NASA TECHNICAL MEMORANDUM

NASA TM X-1785

C.1

NASA TM X-1785

JET EFFECTS ON BOATTAIL PRESSURE DRAG OF ISOLATED EJECTOR NOZZLES AT MACH NUMBERS FROM 0.60 TO 1.47

by Douglas E. Harrington

Lewis Research Center
Cleveland, Ohio

NATIONAL AERONAUTICS AND SPACE ADMINISTRATION • WASHINGTON, D. C. • MAY 1969

JET EFFECTS ON BOATTAIL PRESSURE DRAG OF ISOLATED EJECTOR NOZZLES AT MACH NUMBERS FROM 0.60 TO 1.47

By Douglas E. Harrington

Lewis Research Center
Cleveland, Ohio

NATIONAL AERONAUTICS AND SPACE ADMINISTRATION

For sale by the Clearinghouse for Federal Scientific and Technical Information
Springfield, Virginia 22151 – CFSTI price $3.00

ABSTRACT

The cylindrical ejector nozzles were operated over a range of pressure ratios from approximately 1.0 (jet off) to 11. Results were obtained with both 15° and 10° boattail angles. The 15° configurations utilized different radii of curvature at the boattail juncture with a cylindrical forebody. Subsonically, the jet caused large reductions in boattail pressure drag whether the jet was under or overexpanded. Supersonically, however, reductions in boattail drag were obtained only if the jet was near full expansion or was underexpanded. A jet boundary simulator was effective in duplicating a fully expanded jet with an exit static-pressure ratio of one.

JET EFFECTS ON BOATTAIL PRESSURE DRAG OF ISOLATED EJECTOR NOZZLES AT MACH NUMBERS FROM 0.60 TO 1.47

by Douglas E. Harrington

Lewis Research Center

SUMMARY

An experimental investigation has been conducted to determine the effects of a cold jet on the boattail pressure drag of four isolated cylindrical ejector nozzles. The Mach number range was from 0.60 to 1.47. Nozzle pressure ratio was varied from approximately 1.0 (jet off) to 11. The effects of secondary airflow were also studied. The nozzle configurations included three with a 15° trailing-edge boattail angle and one with a 10° boattail. The boattail juncture with the cylindrical portion of the nacelle for the 15° configurations was faired with different radii of curvature. In addition, jet effects were simulated by a cylinder positioned downstream of the nozzle exit for the 15° configurations.

At subsonic speeds, the jet caused large reductions in drag of the 15° boattails. This drag reduction was relatively insensitive to nozzle pressure ratio for values much less than the design value. However, boattail drag was further reduced as the jet pressure ratio was increased to the design condition and beyond, thereby increasing the jet-exit static-pressure ratio and hence the tendency for jet pluming to occur downstream of the nozzle exit. Supersonically, the boattail pressure drag was unaffected by the jet until it also approached full expansion. As it became underexpanded, the boattail drag was significantly reduced. The trends were basically the same for the 10° boattails except that boattail drag was affected to a lesser degree by the jet.

In general, the effect of increasing secondary flow was to decrease boattail pressure drag by increasing the jet-exit static-pressure ratio. Secondary flow was most effective in reducing boattail pressure drag coefficient at subsonic speeds when the nozzle was operating at or near full expansion or was underexpanded. A cylindrical jet boundary simulator was effective in duplicating a fully expanded jet with an exit to local ambient static pressure ratio of one.

INTRODUCTION

Current airbreathing propulsion systems designed for supersonic flight operate over a wide range of nozzle pressure ratios. To maintain efficient operation at all flight speeds, variations in the nozzle expansion ratio are required. At subsonic speeds, for example, the exit area of a variable flap divergent ejector will be smaller than that required at supersonic speeds. This reduction in exit area necessitates increased boattailing of the afterbody. The resultant drag can be a significant portion of the net thrust of the propulsion system, particularly at subsonic cruise where the engine is at a reduced power setting. In addition, the jet issuing from the exit of the nozzle will have a pronounced effect on boattail drag (refs. 1 to 3).

As part of a program in airbreathing propulsion at the Lewis Research Center, various nozzle concepts, designed primarily for supersonic cruise application, are being studied at off-design conditions. Subsonic and transonic performance is being obtained with cold-flow models in isolated nacelles in the Lewis 8- by 6-Foot Supersonic Wind Tunnel. These results will be compared with the installed performance of the same nozzles obtained during flight tests using an F-106B aircraft. Nacelles that house an afterburning J-85/13 turbojet engine as a gas generator will be installed under the large delta wing of the F-106B with the nozzles extending downstream of the trailing edge. Scale models of the F-106B are also being studied in the wind tunnel (ref. 4) to determine testing procedures that provide correlation with flight data.

An experimental investigation, therefore, was conducted in the Lewis 8- by 6-Foot Supersonic Wind Tunnel to determine the effects of a cold jet on the drag of four isolated ejector nozzles. The Mach number range was from 0.60 to 1.47 and nozzle-pressure ratio was varied from approximately 1.0 (jet off) to 11. In addition, a cylinder was positioned downstream of the nozzle exit for the 15° configurations to determine the effectiveness of a jet boundary simulator in duplicating the effects of a jet on boattail pressure drag.

SYMBOLS

A	cross-sectional area
C_D	pressure drag coefficient, D/q_0A_m
C_p	pressure coefficient, $(p - p_0)/q_0$
D	drag
d	diameter
F	nozzle gross thrust

$\frac{F - D}{F_{ip} + F_{is}}$	nozzle efficiency
$\frac{F - D}{F_{ip}}$	nozzle gross thrust coefficient
M	Mach number
P	total pressure
P_s	secondary total pressure measured beneath primary nozzle actuating ring
P'_s	secondary total pressure measured at station 7
p	static pressure
q	dynamic pressure
r	boattail juncture radius of curvature
T	total temperature
w	weight flow rate
$\frac{w_s}{w_p}\sqrt{\frac{T_s}{T_p}}$	corrected secondary weight flow ratio
v	velocity
x	axial distance downstream of adapter-afterbody interface
y	distance measured along primary rake from primary airflow passage wall
z	radial distance from model surface
α	primary flap angle
δ	boundary-layer thickness
δ^{**}	momentum thickness

Subscripts:

i	ideal
m	model
p	primary air
s	secondary air
$\ell 0$	local ambient
β	boattail surface

0 free-stream

7 nozzle inlet station

8 nozzle throat station

9 nozzle exit station

APPARATUS AND PROCEDURE

Installation

The nozzles were strut mounted in the test section of the Lewis 8- by 6-Foot Supersonic Wind Tunnel as shown in figure 1. The geometry of the model and its thrust-measuring system are shown in figure 2. The main part of the model was a strut-supported cylinder with an ogive nose. The model external shell was grounded and was supported from the tunnel ceiling by a hollow, vertical strut. The adapter portion of the model was attached to the air bottle, which was cantilevered by flow tubes from supply manifolds located outside the test section. Front and rear bearings supported the air bottle. Thus, the axial force acting on the floating part of the model, including both the adapter and nozzle sections, was transmitted to the load cell, located in the nose of the model shell. The nozzle performance presented herein does not include the friction drag measured on the floating portion of the model designated as the adapter section.

The downstream end of the adapter section was arbitrarily selected as being 0.75 model diameter upstream of the nozzle throat (station 8). Friction drag on the adapter section was estimated using the semiempirical, flat-plate, local skin-friction coefficient (given in fig. 6 of ref. 5) as a function of free-stream Mach number and Reynolds number. The coefficient accounts for variations in boundary-layer thickness and flow profile with Reynolds number. Previous measurements of the boundary-layer characteristics at the aft end of this jet exit model in the 8- by 6-Foot Supersonic Wind Tunnel indicated that the profile and thickness were essentially the same as that computed for a flat plate of equal length. The strut wake appeared to affect only a localized region near the top of the model and resulted in a lower local free-stream velocity than measured on the side and bottom of the model. Therefore, the results of reference 5 were used without correction for three-dimensional flow effects or strut interference effects. The calculated friction drag of the adapter section was, therefore, added to the load cell reading to obtain the thrust-minus-drag of the nozzle section.

A static calibration of the thrust-measuring system was obtained by applying a known force to the nozzle and measuring the output of the load cell. To minimize changes in the calibration due to variations in temperature (e.g., aerodynamic heating due to external flow), the load cell was surrounded by a water-cooled jacket and was maintained at a constant temperature.

Primary and secondary air were provided by means of airflow supply lines which entered the model through the support strut. Secondary air in the central air bottle passed through crossover struts inside the model to simulate cooling flow for the primary nozzle and the internal surface of the outer shroud. A uniform primary flow was maintained by using a choke plate and two straightening screens upstream of station 7.

Primary weight flow rate was determined from static and total pressure and temperature measurements at station 7 and a calibration constant for the flow system based on measurements for a standard ASME nozzle. Secondary weight flow rate was determined from a standard ASME flow-metering orifice located in the secondary air-supply line. The ambient pressure was constant for a given free-stream Mach number; thus, a variation in nozzle pressure ratio was obtained by varying the nozzle total pressure P_7.

Nozzle Geometry

The four nozzle configurations that were tested are shown in figure 3. Three of these configurations had 15° boattail trailing-edge angles. Since the emphasis of the test was on the external drag rather than on internal performance, simple cylindrical ejectors were used for the internal flow. The nozzle exit diameter was 5.725 inches (14.542 cm). The boattail juncture with the cylindrical portion of the nacelle for these 15° configurations was smoothed with different radii of curvature. These radii were 0 (sharp edge), 0.5, and 2.5 model diameters. In order to simulate another trailing-edge flap position, a 10° boattail angle with a radius of curvature of 0.5 model diameter was also tested. The 10° nozzle was the cylindrical-ejector type, but it had an exit diameter of 6.636 inches (16.855 cm). In conjunction with the F-106B flight tests at Lewis Research Center, a General Electric J-85/13 primary nozzle was simulated for this test. Since the primary nozzle of the J-85/13 engine has a variable throat, two different throat areas were used with each of the four afterbody configurations in this test. The smaller throat area corresponded to the minimum reheat setting (Primary I) while the larger area simulated maximum reheat (Primary II). The actuating mechanism for varying primary throat area was simulated by a ring containing 12 slots. Secondary air was forced to flow beneath this ring by means of a deflector.

In addition to these configurations, the nozzles with 15° boattails were tested in the presence of a cylindrical section extending from the nozzle exit (station 9) as shown in figure 3(e). The purpose of the cylinder was to approximate the local flow field that would exist if a jet were fully expanded with an exit static-pressure ratio $p_9/p_{\ell 0}$ of 1.0. The jet boundary simulator diameter was equal to the nozzle base diameter.

Instrumentation

Afterbody pressure instrumentation for a typical configuration is shown in figure 4(a). It was assumed that the flow field over the afterbody was symmetric about the strut centerline. Thus, with the exception of one row of instrumentation, all boattail static-pressure orifices were located on one side of the afterbody. Limitations in space necessitated one of the rows being at 300° instead of 60°.

Boattail static-pressure orifices were located at the centroids of equal projected areas and the pressure-drag coefficient was computed using the method described in reference 6. Extra pressure taps were located just downstream of the boattail juncture of the 15° ($r/d_m = 0$) configuration to help define boattail pressure distributions. These pressures were located at 0°, 90°, and 180° and were not used for pressure-drag determination. In addition, three rows of static-pressure orifices were located on the cylindrical portion of each nozzle at 0°, 90°, and 180°. The axial location of each afterbody orifice was determined by the distance x downstream of the adapter-nozzle interface. Table I gives the position of each orifice as well as a nondimensional position coordinate x/d_m. Nozzle exit pressure p_9 was assumed to be the average of five pressures located in the exit plane (station 9). Local ambient pressure p_{l0} was assumed to be the average of the six pressures located at the trailing edge of the boattail and in the same axial plane as orifice 13.

Details of temperature and pressure instrumentation at station 7 are shown in figure 4(b). Pressures in the primary airflow passage were measured by two static-pressure orifices and a total-pressure rake containing 11 tubes. Primary nozzle total pressure was obtained from an integrated average of these pressures. The accompanying table lists pressure orifice spacing as distance y from the inner surface of the passage. Secondary-air total pressure P'_s was measured using four total-pressure tubes. Primary- and secondary-air total temperatures were measured by copper-constantan thermocouples.

Additional secondary-air total-pressure instrumentation is shown in figure 4(c). Secondary-air total pressure P_s was assumed to be the average of four pressures recorded beneath the actuating ring of the simulated J-85/13 primary nozzle. The four tubes were located at 0°, 90°, 180°, and 270° circumferentially. Pumping characteristics were determined using this total pressure. Details of boundary-layer rake instrumentation are presented in figure 4(d). The three rakes were located at 0°, 90°, and 180° circumferentially. The survey plane was located approximately at the adapter-nozzle interface. The total pressures from the rakes were used with local static pressures to compare values of V/V_0 using the Rayleigh-pitot equation.

TABLE I. - NOZZLE AFTERBODY STATIC-PRESSURE ORIFICE LOCATIONS[a]

Orifice	Boattail angle, deg											
	15								10			
	Dimensionless radius ratio, r/dm											
	0			0.5			2.5			0.5		
	Boattail length, x		Ratio of boattail length to model diameter, x/d_m	Boattail length, x		Ratio of boattail length to model diameter, x/d_m	Boattail length, x		Ratio of boattail length to model diameter, x/d_m	Boattail length, x		Ratio of boattail length to model diameter, x/d_m
	in.	cm		in.	cm		in.	cm		in.	cm	
1	5.99	15.21	0.708	5.99	15.21	0.708	2.67	6.78	0.316	5.57	14.15	0.659
2	7.98	20.27	.944	7.86	19.96	.930	4.88	12.39	.577	7.61	19.33	.900
3	9.85	25.02	1.165	9.73	24.71	1.151	5.99	15.21	.708	9.65	24.51	1.141
4	10.22	25.96	1.209	-----	-----	-----	-----	-----	-----	-----	-----	-----
5	10.31	26.19	1.219	10.25	26.03	1.212	8.93	22.68	1.056	10.23	25.98	1.210
6	10.80	27.43	1.277	10.80	27.43	1.277	10.16	25.80	1.202	10.77	27.35	1.274
7	11.32	28.75	1.339	11.32	28.75	1.339	11.03	28.01	1.304	11.32	28.75	1.339
8	11.85	30.10	1.401	11.85	30.10	1.401	11.75	29.84	1.390	11.88	30.17	1.405
9	12.41	31.52	1.468	12.41	31.52	1.468	12.39	31.47	1.465	12.45	31.62	1.472
10	12.99	32.99	1.536	12.99	32.99	1.536	12.99	32.99	1.536	13.04	33.12	1.542
11	13.59	24.52	1.607	13.59	34.52	1.607	13.59	24.52	1.607	13.65	34.67	1.614
12	14.22	36.12	1.682	14.22	36.12	1.682	14.22	36.12	1.682	14.27	36.24	1.688
13	14.90	37.84	1.762	14.90	37.84	1.762	14.90	37.84	1.762	14.92	37.90	1.764

[a]See fig. 4(a).

RESULTS AND DISCUSSION

Jet Effects

Figure 5 presents the boundary-layer characteristics of the basic model used in this study. At all Mach numbers, the boundary layer at 0° was noticeably affected by the wake of the support strut. The ratio of momentum thickness to model diameter δ^{**}/d_m is also listed for the boundary-layer rake located at 180°. Momentum thickness was based on the local conditions at the outermost tube of the rake and was found to be constant between $M_0 = 0.70$ and $M_0 = 1.19$.

A typical boundary-layer profile is shown in figure 6 for the rake at 180° and $M_0 = 0.90$. This profile is compared with a 1/7 profile, which is denoted by the solid line.

The effect of nozzle jet flow on boattail pressure-drag coefficient is shown in figure 7. Results for the 15° boattail configurations are presented in figures 7(a) to 7(f) and the 10° boattail configurations are presented in figures 7(g) and 7(h). The range of nozzle pressure ratios was chosen to encompass the typical operating points of turbojet engines designed for supersonic flight. All pressure ratios were obtained with a nominal 3-percent corrected secondary flow, and corrected secondary flow was varied from 0 to 15 percent at typical conditions to study its effect.

Subsonically, even at pressure ratios much less than the design value, large reductions in boattail drag were obtained for the 15° boattails. This drag reduction was relatively insensitive to nozzle pressure ratio for values much less than the design value. However, boattail drag was further reduced as the jet pressure ratio was increased to the design condition and beyond. Supersonically, the boattail pressure drag was unaffected by the jet until it approached full expansion. As it became underexpanded, the boattail drag was significantly reduced. The presence of a jet was also favorable for the 10° boattails at subsonic speeds since, in general, boattail pressure-drag coefficient was decreased by turning the jet on. Supersonically, however, for the 10° boattails with both primaries I and II, the presence of a jet was not as effective in reducing boattail pressure-drag coefficient because the exit area A_9 was larger and the jet required a larger pressure ratio to be fully expanded.

The effect of secondary flow on boattail pressure-drag coefficient is also presented in figure 7. Secondary weight flow was varied from 0 to 15 percent of primary weight flow. The listed values of corrected secondary weight flow ratio are nominal values.

In general, the effect of increasing secondary flow was to decrease boattail pressure-drag coefficient. However, for the 15° boattail ($r/d_m = 0$) with primary I ($A_9/A_8 = 1.70$) at $M_0 = 0.6$, 1.20, 1.27, and 1.47, increasing secondary flow initially increased and then decreased boattail pressure-drag coefficient. This could have also been the case

for the other 15° boattails with primary I at $M_0 = 1.20$, 1.27, and 1.47 but there were insufficient data at the pertinent pressure ratios to substantiate this. For the 10° boattails, increasing secondary flow to 3 percent of primary weight flow increased boattail pressure-drag coefficient. Further increases in secondary weight flow decreased the boattail pressure-drag coefficient. The exception to the above trends for the 10° boattails occurred with primary I at $M_0 = 0.6$ and 0.7 where the effects of increasing secondary flow were inconclusive. Secondary flow was most effective in reducing boattail pressure-drag coefficient at subsonic speeds when the nozzle was operating at or near full expansion or was underexpanded. This reduction in drag was due to an increase in $p_9/p_{\ell 0}$ caused by increasing secondary flow.

The effect of nozzle pressure ratio on afterbody pressure distributions is presented in figure 8 for all configurations tested. With the jet on, a nominal value of corrected secondary weight flow ratio of 0.03 was selected. At subsonic speeds, the principal effect of the jet was to raise the static-pressure level over the entire boattail surface. At the transonic and supersonic Mach numbers, the major jet effects were confined to the aft portion of the boattail. At these speeds an underexpanded jet forced the trailing compression shock forward on the boattail, reducing pressure drag. This effect was most noticeable for the nozzles with small area ratios (primary II) since these configurations were underexpanded at these higher speeds and pressure ratios. The major effect of increasing the radius ratio r/d_m was to reduce the initial overexpansion on the boattail and, thus, reduce boattail pressure drag.

The effect of nozzle exit static-pressure ratio on boattail pressure drag coefficient is shown in figure 9. Corrected secondary weight flow ratio was varied from 0 to 0.15. With no jet flow, the exit static-pressure ratio was near one. As the jet was turned on and its pressure ratio increased toward the design point, the exit static-pressure ratio initially decreased. However, in some cases (in particular, for the 10° boattail with primary I), the jet did not attach itself to the shroud until higher pressure ratios were attained. In these instances, $p_9/p_{\ell 0}$ remained at a value of one until attachment was achieved and then decreased as pressure ratio was increased. In this highly overexpanded flow regime, a system of oblique shocks would be present in the cylindrical portion of the nozzle. As pressure ratio was increased, this system of shock waves would move downstream until it reached the nozzle exit. At this point, any further increases in pressure ratio causes the exit pressure ratio to increase; the shock system would then be located downstream of the nozzle exit. As the jet pressure ratio approached the fully expanded condition, the exit pressure ratio would approach one; as the jet becomes underexpanded at higher pressure ratios, the exit pressure ratio becomes greater than one. At overexpanded conditions, increasing secondary flow had no effect on $p_9/p_{\ell 0}$. However, at underexpanded and fully expanded conditions, increasing secondary flow increased $p_9/p_{\ell 0}$.

For the 15° boattails with primary II ($A_9/A_8 = 1.22$), boattail pressure drag coefficient was predominantly a function of $p_9/p_{\ell 0}$. These configurations were underexpanded ($p_9/p_{\ell 0} > 1$) over most of the range of test variables. For the 15° boattails with primary I ($A_9/A_8 = 1.70$) and the 10° boattails, however, $p_9/p_{\ell 0}$ was not a very good parameter in correlating boattail pressure drag. Since these configurations were overexpanded over most of the range of test variables, a highly complex flow regime existed in the cylindrical portion of the nozzle. Thus, due to this complicated flow, no simple relation existed between $p_9/p_{\ell 0}$ and boattail pressure drag.

In order to facilitate a comparison of the various configurations tested, a nozzle pressure ratio schedule was assumed for a typical turbojet engine designed for supersonic flight. This schedule is presented in figure 10. The acceleration schedule will be used both for configurations with primary I and for configurations with primary II. A subsonic cruise point was chosen at a pressure ratio of 3.2 and $M_0 = 0.90$.

Using the assumed pressure ratio schedule, the effect of nozzle jet flow on boattail pressure-drag coefficient is shown in figure 11. The effect of a jet was generally favorable in that boattail pressure-drag coefficient was decreased in most cases. The only exception was the 10° boattail with primary I at Mach numbers from 1.00 to 1.47 where the jet effect was minor. For the very underexpanded conditions associated with the 15° boattail ($r/d_m = 2.5$) with primary II, the boattail pressure-drag coefficient was decreased to the extent that a thrust was obtained on the boattail between $M_0 = 0.6$ and 0.96. In addition, for all configurations using primary II, which was underexpanded at most conditions, boattail pressure-drag coefficient was lower than that for the configurations using primary I, which was operating at less than the design pressure ratio at many test conditions. For all configurations, a dip occurred in the drag coefficient curves between $M_0 = 1.00$ and 1.20. This phenomenon resulted from the higher pressures caused by a terminal shock wave on the boattail. In free flight the flow field near the front of an ogive cylinder creates a terminal shock that moves aft rapidly with increasing flight velocity and disappears downstream at speeds slightly above Mach 1. However, in a tunnel installation, large models retard the aft movement of the terminal shock. Thus, the resultant boattail pressure drag can be influenced by tunnel installation effects particularly at speeds where the terminal shock is near the boattail. These phenomena are discussed more thoroughly in reference 7.

The effect of r/d_m on boattail pressure-drag coefficient for the assumed pressure ratio schedule is presented in figure 12. Corrected secondary weight flow ratio was maintained at a nominal value of 0.03. Increasing boattail juncture radius of curvature decreased boattail pressure-drag coefficient over the entire range of test Mach numbers. In particular, for the 15° boattails with primary I ($A_9/A_8 = 1.70$) at subsonic cruise, a reduction in boattail pressure-drag coefficient of 21 percent was achieved by increasing

r/d_m from 0 to 0.5. An additional reduction of 45 percent was obtained by increasing r/d_m to 2.5.

Jet Boundary Simulator Effects

A comparison of jet-boundary simulator data with jet-on and jet-off data is presented in figure 13 for the 15° boattail configurations. The jet-boundary simulator was a cylinder positioned downstream of the nozzle exit, and its diameter was equal to that of the nozzle exit. Jet-on data were obtained by interpolating values of boattail pressure-drag coefficient in figure 9 for $p_9/p_{\ell 0} = 1$ and $(w_s/w_p)\sqrt{T_s/T_p} = 0.03$. When $p_9/p_{\ell 0} = 1$ and P_7/p_0 is at or near the design point, the nozzle is fully expanded, and the jet will exit in an axial direction. The jet-boundary simulator was very effective in duplicating a jet with an exit static-pressure ratio of one when compared with jet-on ($p_9/p_{\ell 0} = 1$) data for the 15° configurations with primary II. These configurations were operating at nozzle pressure ratios at or near design.

However, the jet-boundary simulator was not very effective when compared with jet on ($p_9/p_{\ell 0} = 1$) data for the 15° configurations with primary I. This was particularly true at subsonic and transonic Mach numbers. The ineffectiveness of the simulator in this case was due to the nozzle not operating at or near the design nozzle-pressure ratio. The nozzle was highly overexpanded and sometimes separated. Thus, the jet was smaller than the jet-boundary simulator and a true comparison could not be made. For these configurations, the only good agreement with jet-on was between $M_0 = 1.20$ and 1.47 where the nozzle was operating at or near design. Thus, a jet-boundary simulator was effective in duplicating a fully expanded jet with an exit static-pressure ratio of one.

Thrust and Pumping Characteristics

The thrust and pumping characteristics of each of the configurations tested are presented in figures 14 to 19. For these figures, quiescent data are also presented. The effect of nozzle pressure ratio on nozzle efficiency and pumping characteristics is shown in figure 14. Pumping characteristics were determined using the secondary total pressure measured beneath the primary nozzle actuating ring. Corrected secondary weight flow ratio was held constant at a nominal value of 0.03. Also shown in the plots are cases in which the secondary air total pressure was less than free-stream static pressure, or $P_s < p_0$. In these cases, the ideal gross thrust of the secondary air F_{is} was set equal to zero. Subsonically, nozzle efficiency improved when nozzle pressure ratio was increased until the design value was reached. At pressure ratios higher than design, the

efficiency had a tendency to remain constant. Supersonically, efficiency generally improved with increasing nozzle pressure ratio.

The effect of secondary flow on nozzle efficiency and pumping characteristics is shown in figure 15. Corrected secondary weight flow ratio was varied from 0 to 0.15. At nozzle pressure ratios much less than design, nozzle efficiency was improved by increasing secondary flow. The peak in efficiency was reached at the high values of secondary flow. At pressure ratios just below design, small amounts of secondary flow were very effective in improving nozzle efficiency. Further increases in secondary flow had little effect on efficiency. Above the design pressure ratio, efficiency was generally insensitive to changes in secondary flow.

Figure 16 presents the effect of nozzle pressure ratio on the ratio of boattail pressure drag to the ideal gross thrust of the primary and secondary. For all configurations tested, increasing nozzle-pressure ratio decreased the ratio of boattail pressure drag to the ideal thrust of the primary and secondary. This was due to a twofold effect. As the pressure ratio was increased, the ideal gross thrust also increased, thus reducing the ratio $D_\beta/(F_{ip} + F_{is})$. In addition, for most of the configurations, increasing pressure ratio reduced the boattail pressure drag, particularly at pressure ratios at or above design.

The effect of boattail juncture radius of curvature on nozzle efficiency using the assumed pressure ratio schedule is shown in figure 17. Corrected secondary weight flow ratio was held constant at a nominal value of 0.03. When using the acceleration schedule (open symbols in fig. 17), r/d_m effects on nozzle efficiency were, in general, minor. This was because, at these particular pressure ratios, boattail pressure drag was such a small percentage of gross nozzle thrust that even large changes in r/d_m had little effect on nozzle efficiency. The effects of r/d_m became important only for the 15^o boattail with $r/d_m = 2.5$ above $M_0 = 0.95$ where nozzle efficiency was improved from 1 to 2 percent. At subsonic cruise, nozzle efficiency was improved by 1.5 percent when r/d_m was increased from 0 to 0.5. An additional improvement of 3.2 percent was obtained when r/d_m was increased to 2.5.

Nozzle gross thrust coefficient, as influenced by nozzle pressure ratio and secondary flow, is presented in figures 18 and 19, respectively.

Total pressure loss through the secondary flow passage as influenced by secondary flow variations is presented in figure 20. This loss was independent of free-stream Mach number and nozzle pressure ratio.

SUMMARY OF RESULTS

An experimental investigation has been conducted to determine the effects of a cold jet on the boattail pressure drag of four isolated ejector nozzles. The Mach number

range was from 0.60 to 1.47. Nozzle pressure ratio was varied from approximately 1.0 (jet off) to 11. The effects of secondary airflow were also studied. The nozzle configurations included three with a 15° trailing-edge boattail angle and one with a 10° trailing-edge boattail angle. The boattail juncture with the cylindrical portion of the nacelle for the 15° configuration was faired with different radii of curvature. In addition, jet effects were simulated with a cylinder positioned downstream of the nozzle exit for the 15° configurations. The following results were obtained:

1. Subsonically, even at pressure ratios much less than the design value, large reductions in boattail drag were obtained for the 15° boattails. This drag reduction was relatively insensitive to nozzle pressure ratio for values much less than the design value. However, boattail drag was further reduced as the jet pressure ratio was increased to the design condition and beyond. Supersonically, the boattail pressure drag was unaffected by the jet until it approached full expansion. As it became underexpanded, the boattail drag was significantly reduced. The trends were basically the same for the 10° boattails with larger exit areas except that the boattail drag was affected to a lesser degree by the jet.

2. For a given nozzle area ratio, boattail pressure drag coefficient is predominantly a function of exit static-pressure ratio when the nozzle is fully expanded or is highly underexpanded and pluming effects are important. However, in regions where the nozzle is overexpanded, no simple relation exists between exit pressure ratio and boattail pressure drag because of jet overexpansion and separation effects.

3. In general, the effect of increasing secondary flow was to decrease boattail pressure drag. Secondary flow was most effective in reducing boattail pressure drag coefficient at subsonic speeds where the nozzle was operating at or near full expansion or was underexpanded. This reduction in drag was due to an increase in jet-exit static-pressure ratio caused by increasing secondary flow.

4. A jet boundary simulator was found to be effective in duplicating a fully expanded jet with an exit to local ambient static-pressure ratio of one.

5. When operating at a typical turbojet pressure ratio schedule, increasing boattail juncture radius of curvature decreased boattail pressure-drag coefficient over the entire range of test Mach numbers. For example, at subsonic cruise a reduction in boattail pressure drag coefficient of 21 percent was achieved by increasing the radius to model diameter ratio from 0 to 0.5 for the 15° boattails with primary I (nozzle exit to throat area ratio, 1.70). An additional reduction of 45 percent was obtained by increasing the radius to model diameter ratio to 2.5.

Lewis Research Center,
National Aeronautics and Space Administration,
Cleveland, Ohio, December 31, 1968,
126-15-02-10-22.

REFERENCES

1. Cortright, Edgar M. Jr.; and Kochendorfer, Fred D.: Jet Effects on Flow Over Afterbodies in Supersonic Stream. NACA RME53H25, November 1953.

2. Cubbage, James M. Jr.: Jet Effects on the Drag of Conical Afterbodies for Mach Numbers of 0.6 to 1.28. NACA RML57B21, April 1957.

3. Englert, Gerald W.; Vargo, Donald J.; and Cubbison, Robert W.: Effect of Jet-Nozzle-Expansion Ratio on Drag of Parabolic Afterbodies. NACA RME54B12, April 1954.

4. Blaha, Bernard J.; and Mikkelson, Daniel C.: Wind Tunnel Investigation of Airframe Installation Effects on Underwing Engine Nacelles at Mach Numbers From 0.56 to 1.46. NASA TM X-1683, 1968.

5. Smith, K. G.: Methods and Charts for Estimating Skin Friction Drag in Wind Tunnel Tests With Zero Heat Transfer. Rep. ARC-CP-824, Aeronautical Research Council, Great Britain, 1965.

6. Shrewsbury, George D.: Effect of Boattail Juncture Shape on Pressure Drag Coefficients of Isolated Afterbodies. NASA TM X-1517, 1968.

7. Mitchell, Glenn A.: Effect of Model Forebody Shape on Perforated Tunned Wall Interference. NASA TM X-1656, 1968.

Figure 1. - Model installed in 8- by 6-Foot Supersonic Wind Tunnel.

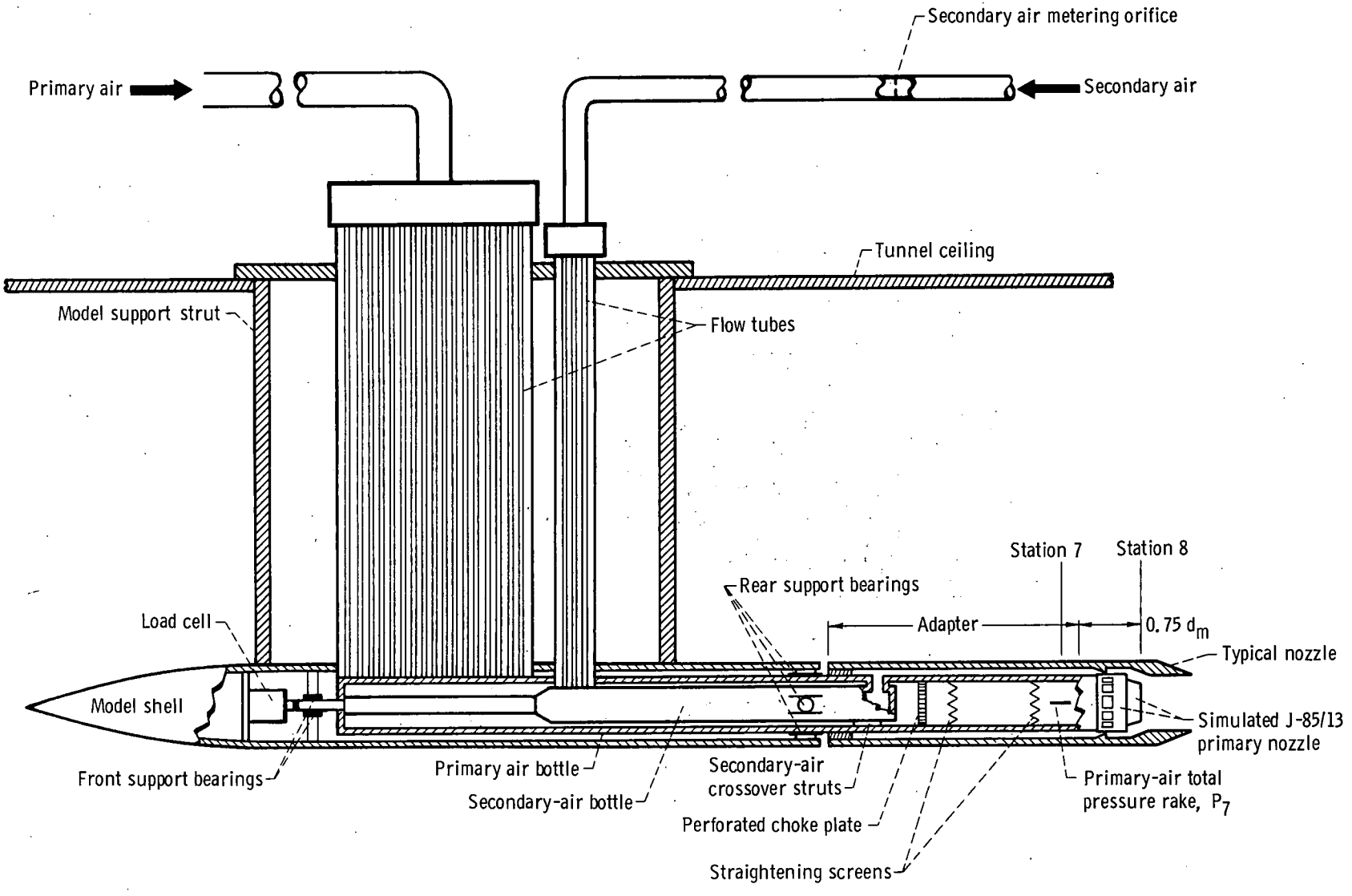

Figure 2. - Model internal geometry and thrust measuring system.

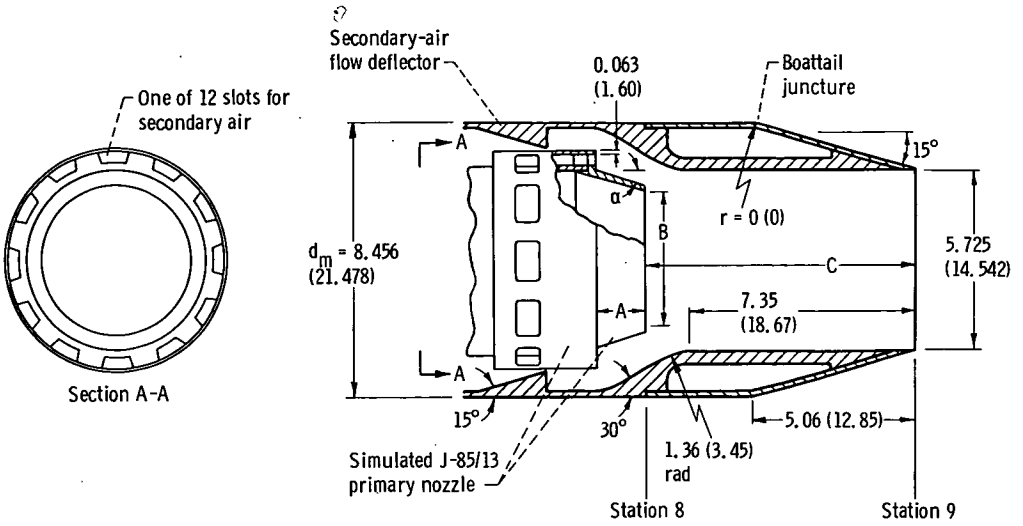

Primary	Primary flap angle, α, deg	A		B		C^a		C^b	
		in.	cm	in.	cm	in.	cm	in.	cm
I	13° 15'	1.500	3.810	4.388	11.146	8.50	21.590	8.60	21.840
II	5° 18'	1.080	2.743	5.192	13.188	8.92	22.657	9.02	22.907

[a]15° boattails only.

[b]10° boattail only.

(a) Boattail angle, 15°; radius ratio, 0.

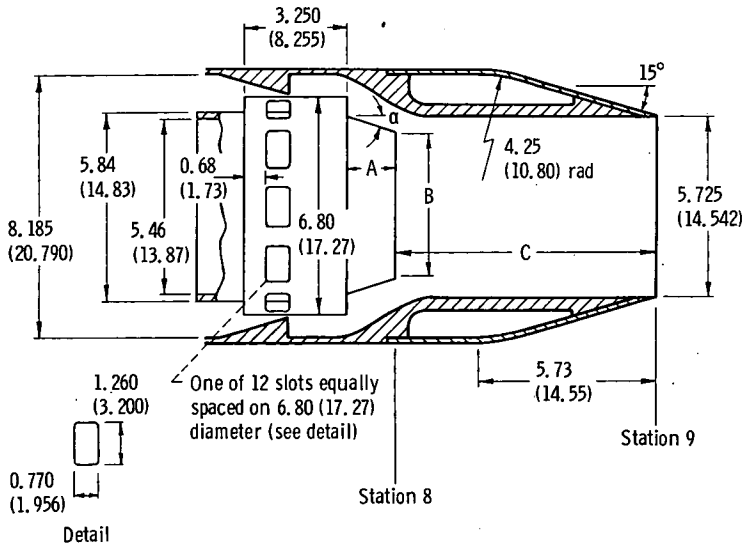

(b) Boattail angle, 15°; radius ratio, 0.5.

Figure 3. - VFE nozzle geometry details (All dimensions are in inches (cm)).

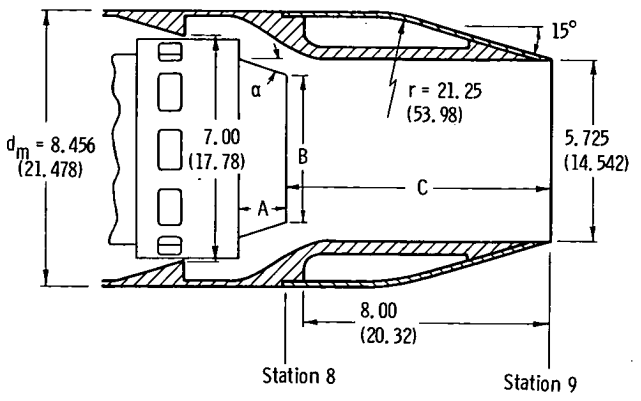

(c) Boattail angle, 15°; radius ratio, 2.5 (See part (a)).

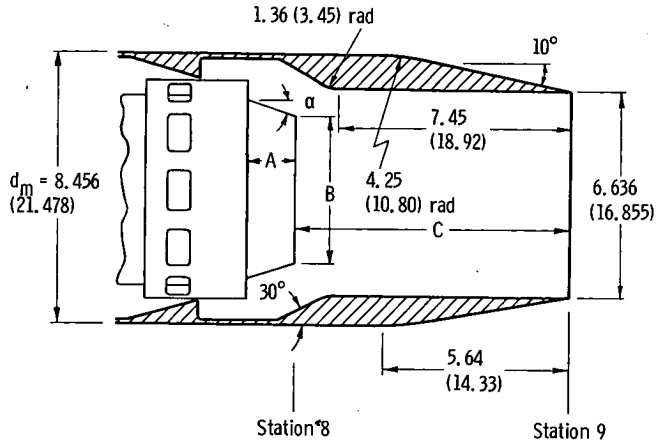

(d) Boattail angle, 10°; radius ratio, 0.5 (See part (a)).

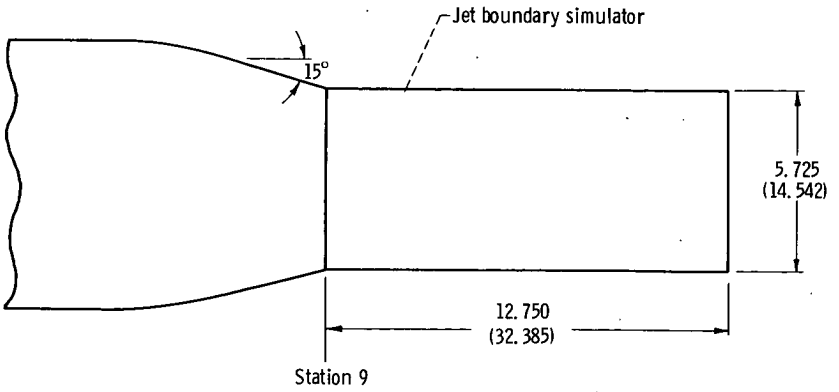

(e) Nozzle with jet boundary simulator (15° boattail configurations only).

Figure 3. - Concluded.

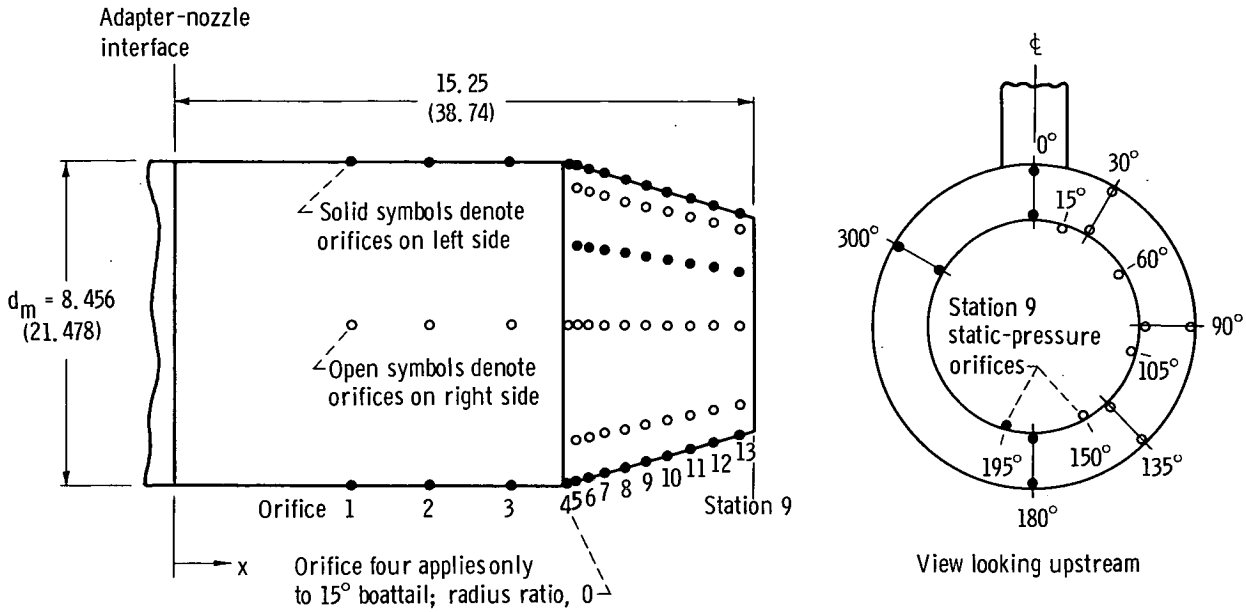

(a) Nozzle afterbody static-pressure instrumentation (see table I for orifice coordinates).

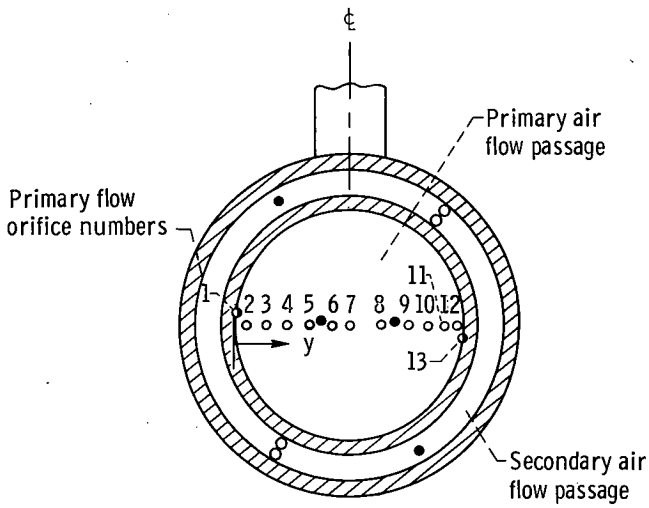

Primary flow orifice number	Distance along primary rake, y	
	in.	cm
1	0	0
2	.29	.74
3	.61	1.55
4	.98	2.49
5	1.43	3.63
6	2.10	5.34
7	3.00	7.61
8	4.28	10.88
9	4.81	12.21
10	5.22	13.28
11	5.56	14.12
12	5.86	14.90
13	6.01	15.27

o Total-pressure orifice
o Static-pressure orifice
• Thermocouple

(b) Details of instrumentation at station 7.

Figure 4. - Model instrumentation details.

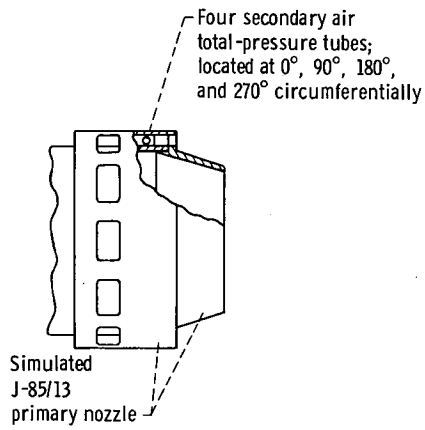

(c) Secondary air total-pressure P_s instrumentation.

Tube	Radial distance ratio, z/d_m
1	0.006
2	.018
3	.035
4	.059
5	.088
6	.124
7	.165
8	.212
9	.265
10	.324

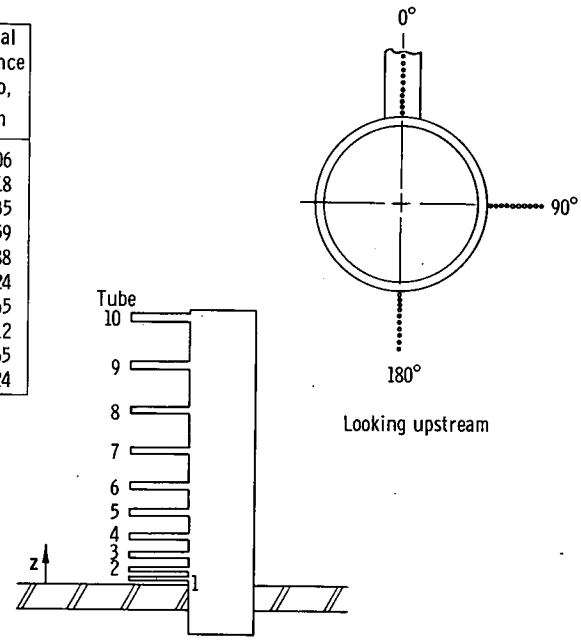

(d) Boundary-layer rake instrumentation.

Figure 4. - Concluded.

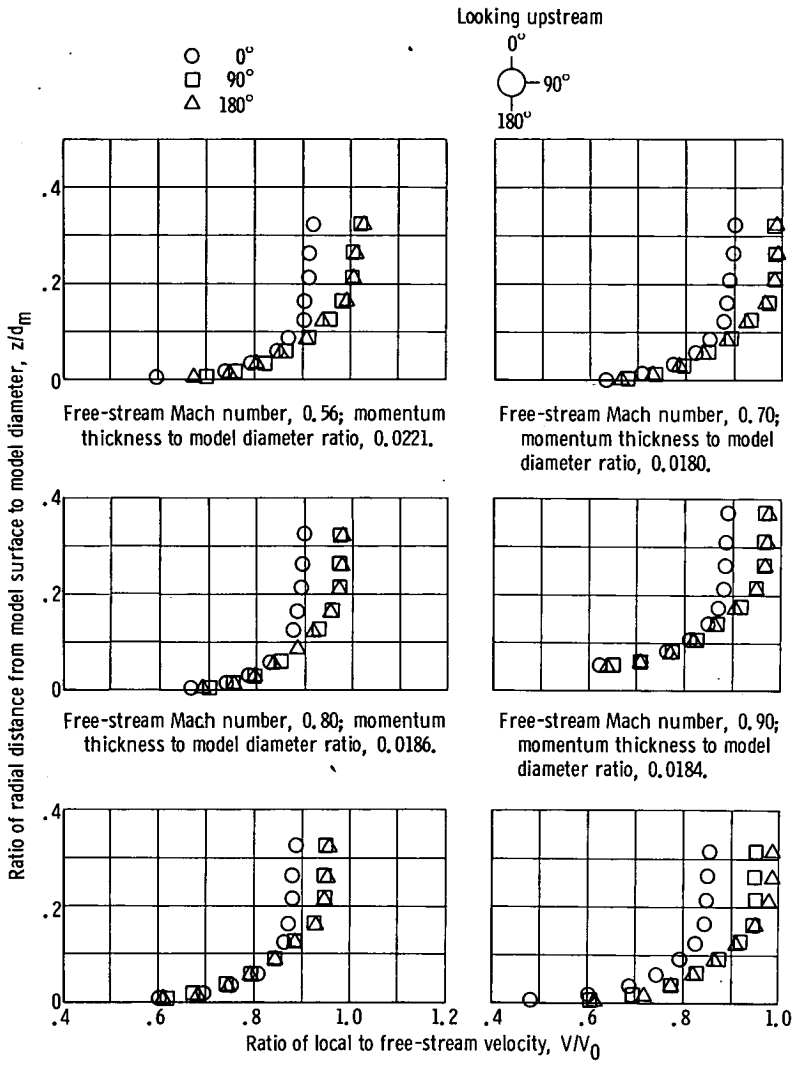

Free-stream Mach number, 0.56; momentum thickness to model diameter ratio, 0.0221.

Free-stream Mach number, 0.70; momentum thickness to model diameter ratio, 0.0180.

Free-stream Mach number, 0.80; momentum thickness to model diameter ratio, 0.0186.

Free-stream Mach number, 0.90; momentum thickness to model diameter ratio, 0.0184.

Free-stream Mach number, 1.00; momentum thickness to model diameter ratio, 0.0184.

Free-stream Mach number, 1.19; momentum thickness to model diameter ratio, 0.0184.

Figure 5. - Afterbody boundary-layer characteristics. (Ratio of momentum thickness to model diameter calculated at 180° only.)

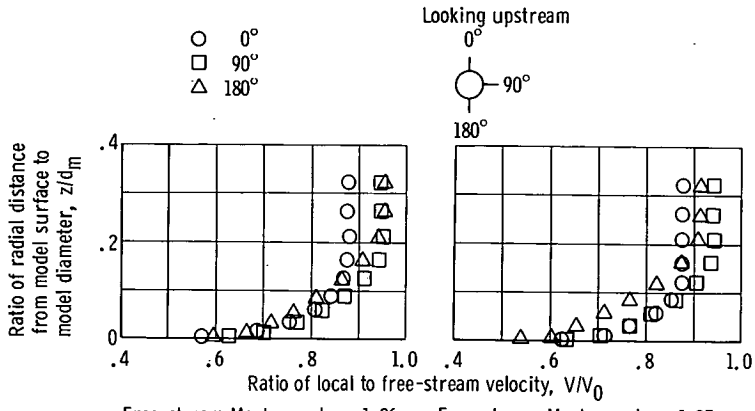

Free-stream Mach number, 1.26; momentum thickness to model diameter ratio, 0.0214.

Free-stream Mach number, 1.37; momentum thickness to model diameter ratio, 0.0217.

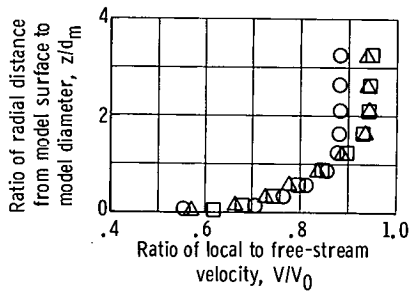

Free-stream Mach number, 1.46; momentum thickness to model diameter ratio, 0.0152.

Figure 5. - Concluded.

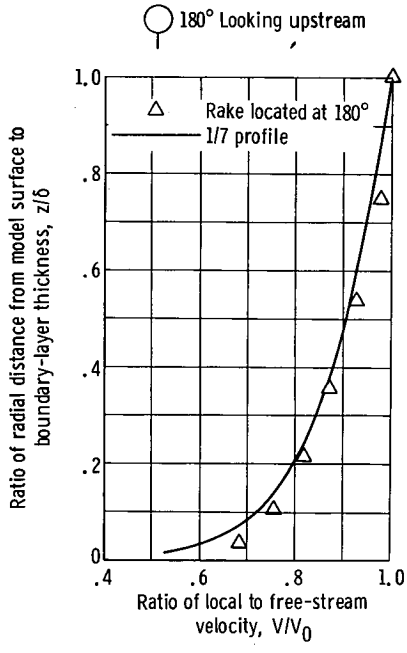

Figure 6. - Typical boundary-layer profile. Free-stream Mach number, 0.90.

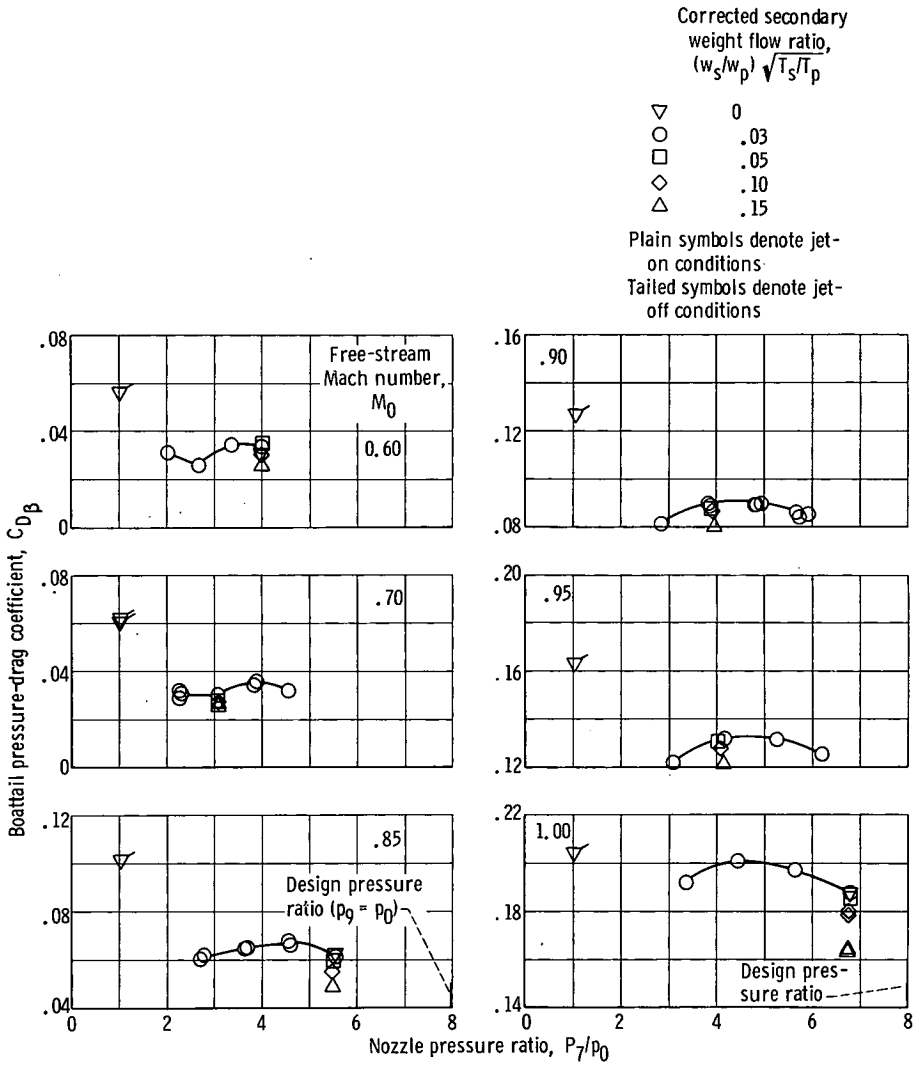

(a) Boattail angle, 15° radius ratio, 0; primary I; nozzle exit to throat area ratio, 1.70.

Figure 7. - Jet effect on boattail pressure drag coefficient.

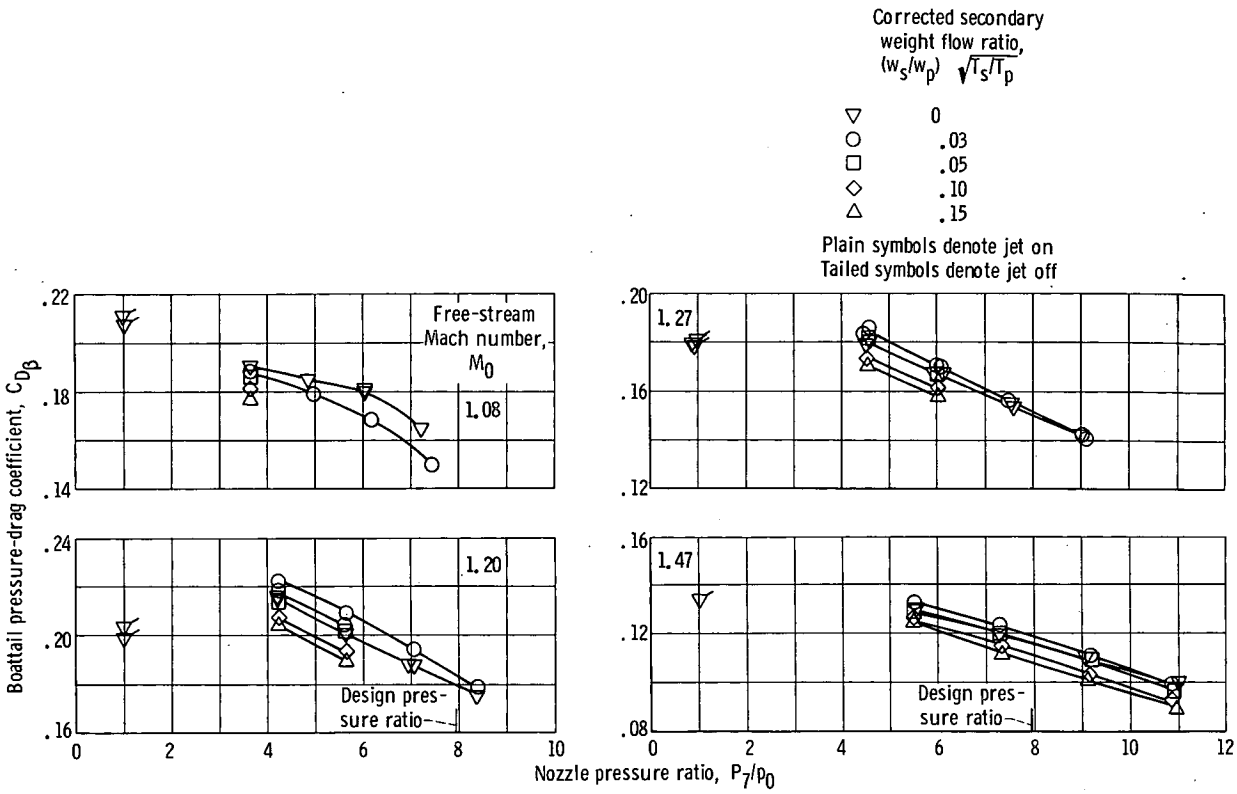

(a) Concluded.

Figure 7. - Continued.

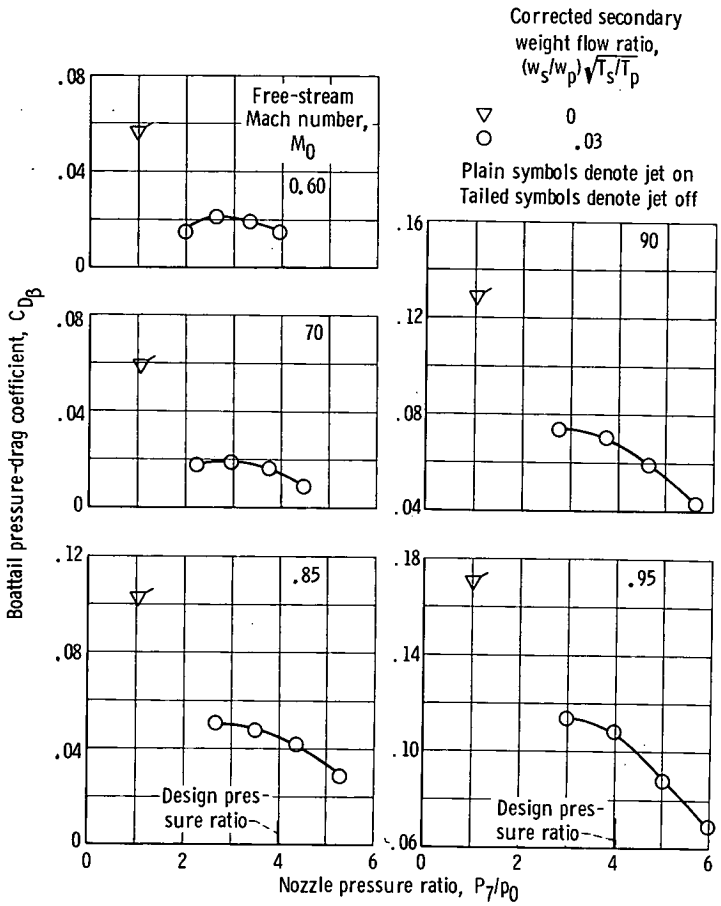

(b) Boattail angle, 15°; radius ratio, 0; primary II; nozzle exit to throat area ratio, 1.22.

Figure 7. - Continued.

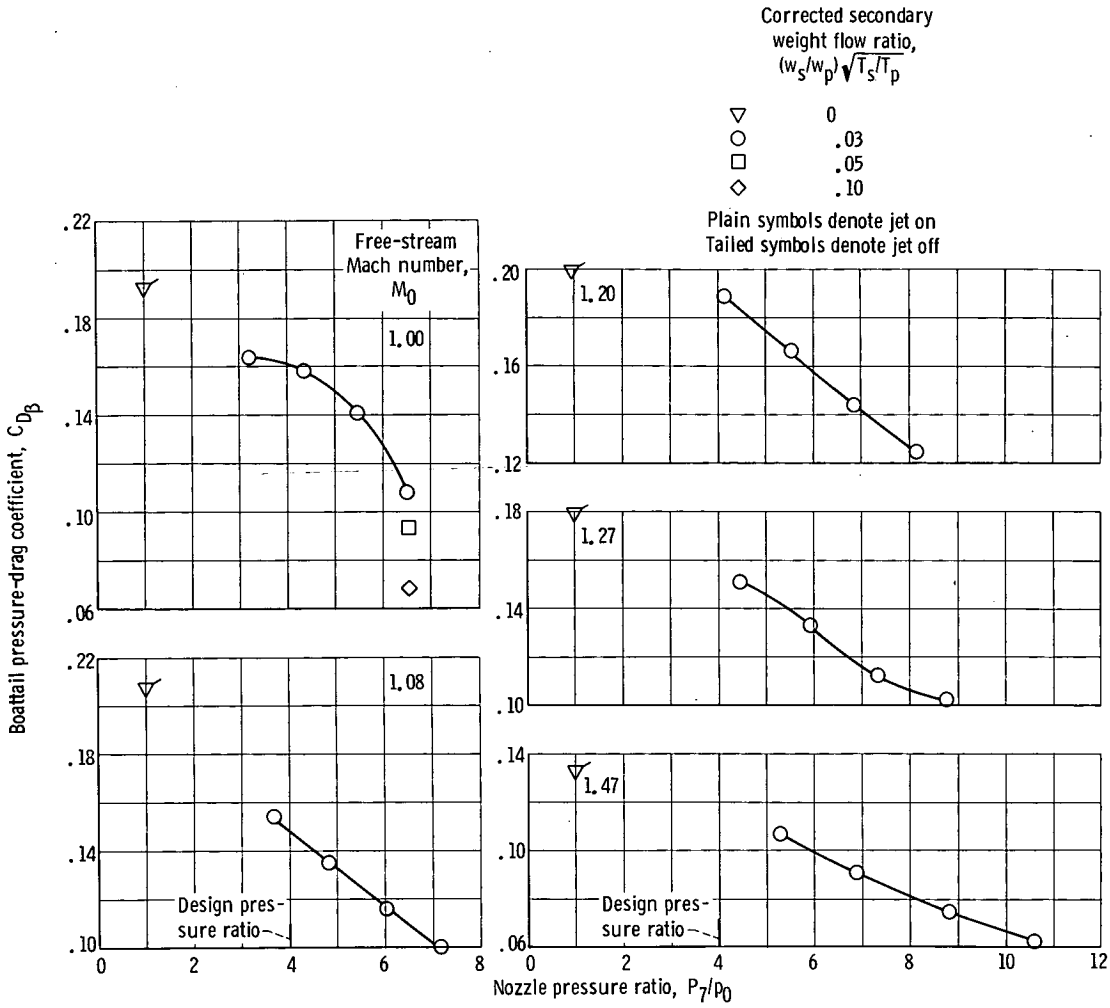

(b) Concluded.

Figure 7. - Continued.

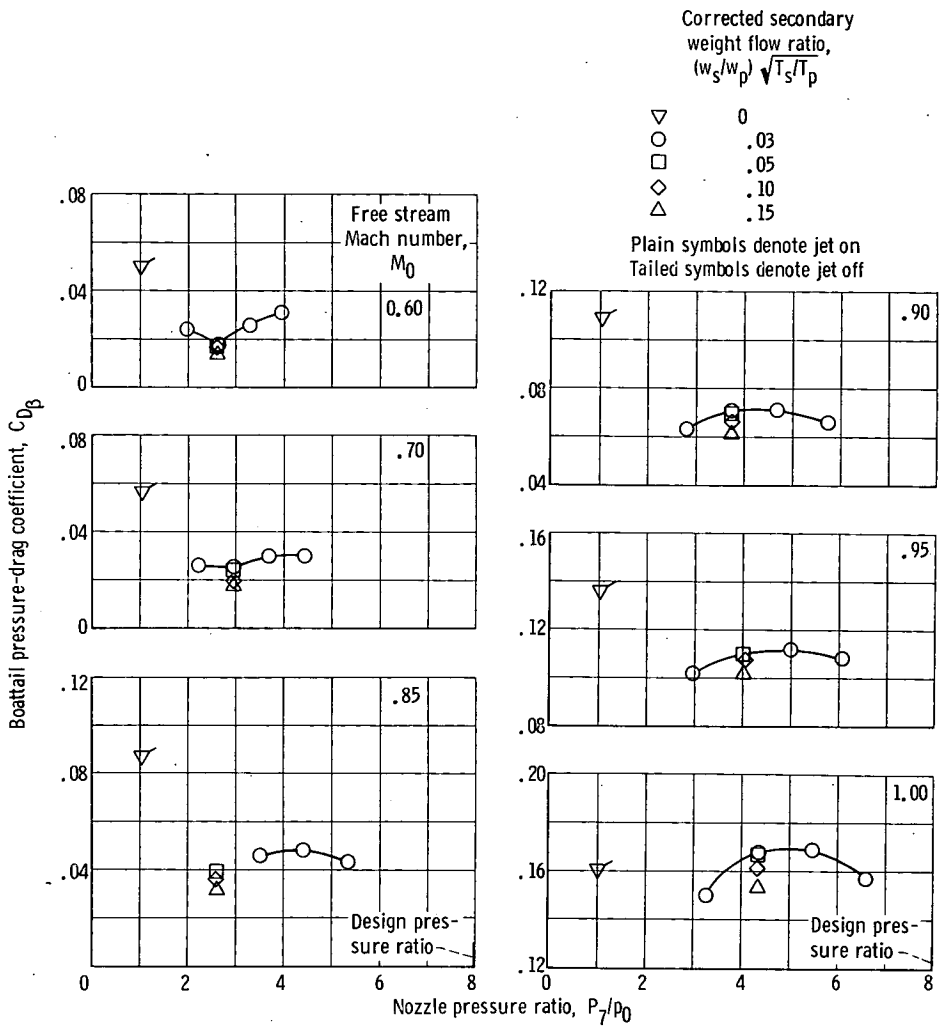

(c) Boattail angle, 15°; radius ratio, 0.5; primary I; nozzle exit to throat area ratio, 1.70.

Figure 7. - Continued.

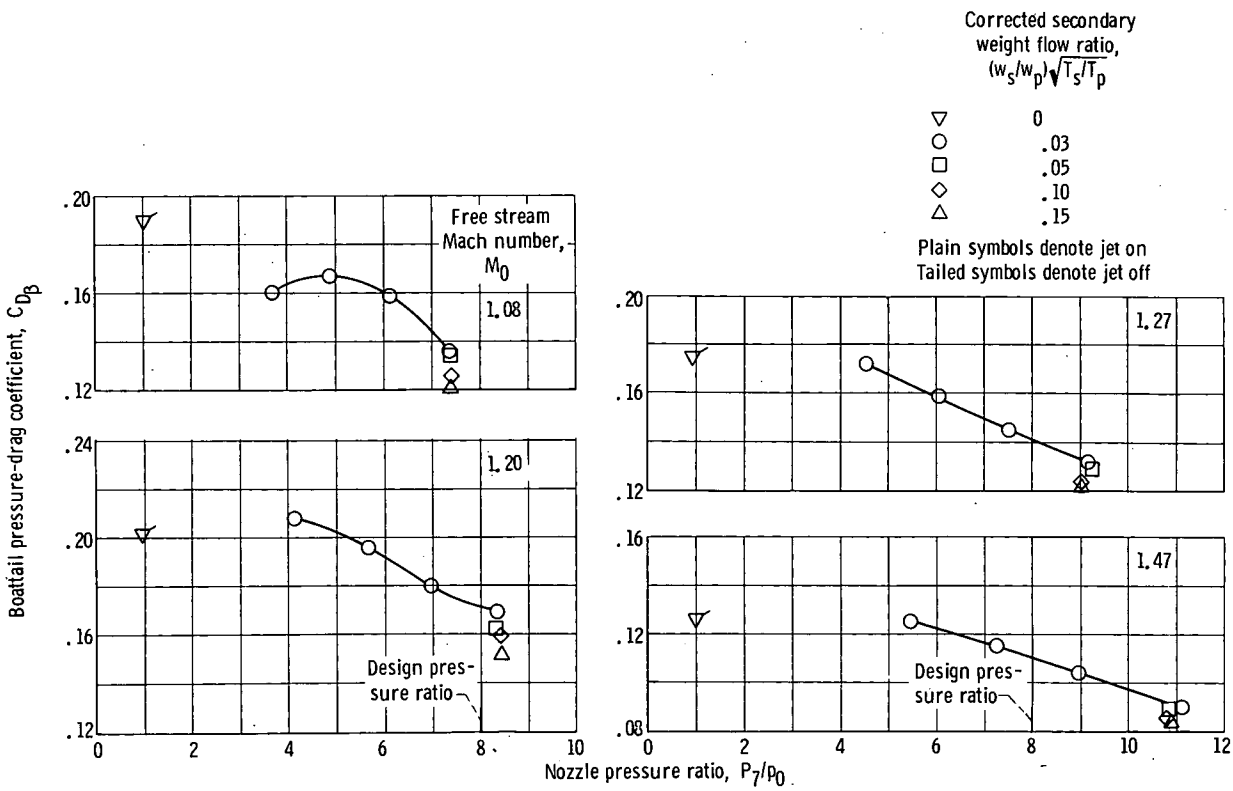

(c) Concluded.

Figure 7. - Continued.

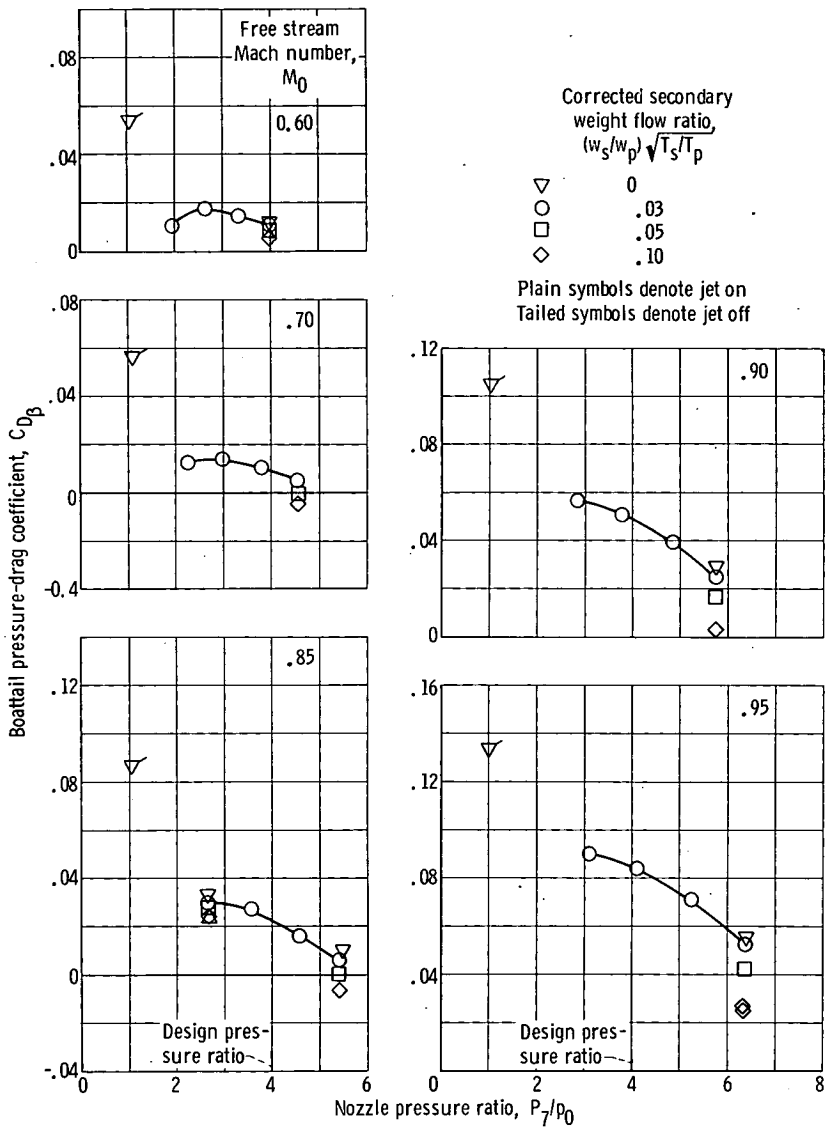

(d) Boattail angle, 15°; radius ratio, 0.5; primary II; nozzle exit to throat area ratio, 1.22.

Figure 7. - Continued.

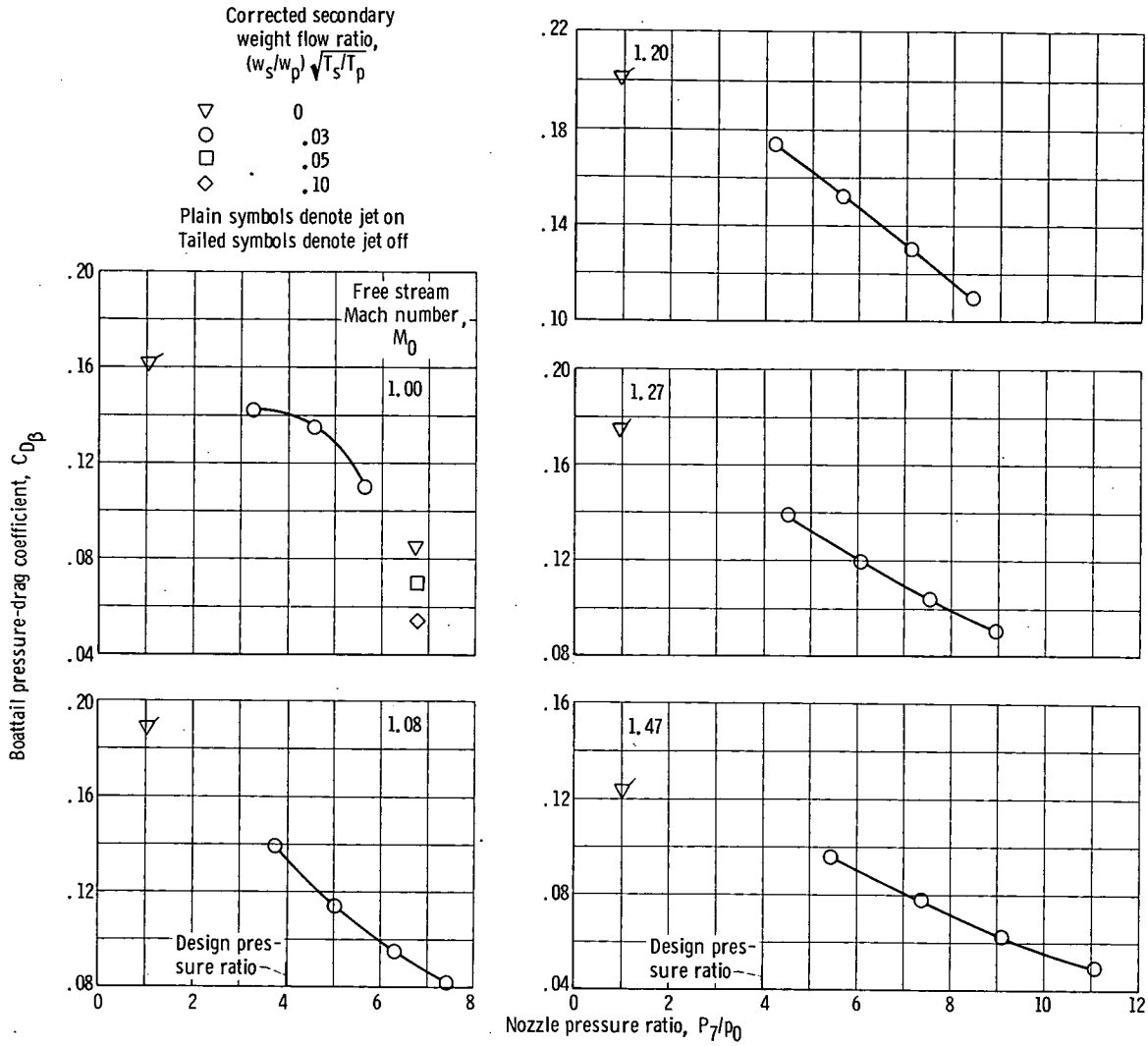

(d) Concluded.

Figure 7. - Continued.

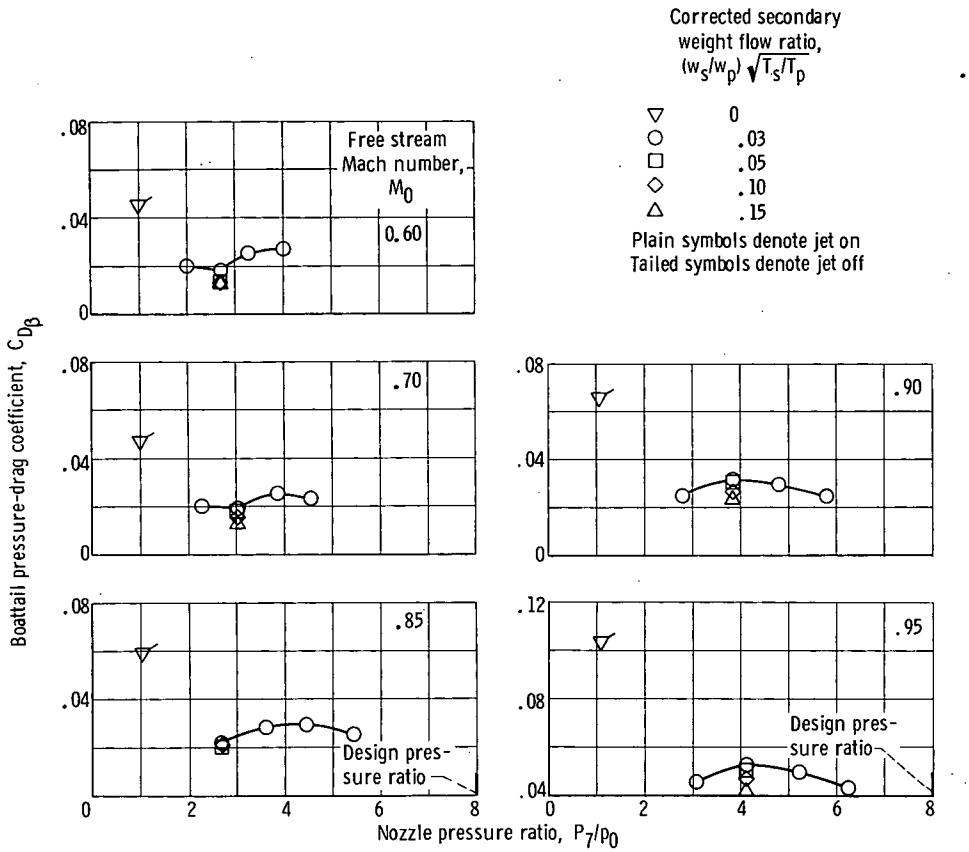

(e) Boattail angle, 15°; radius ratio, 2.5; primary I; nozzle exit to throat area ratio, 1.70.

Figure 7. - Continued.

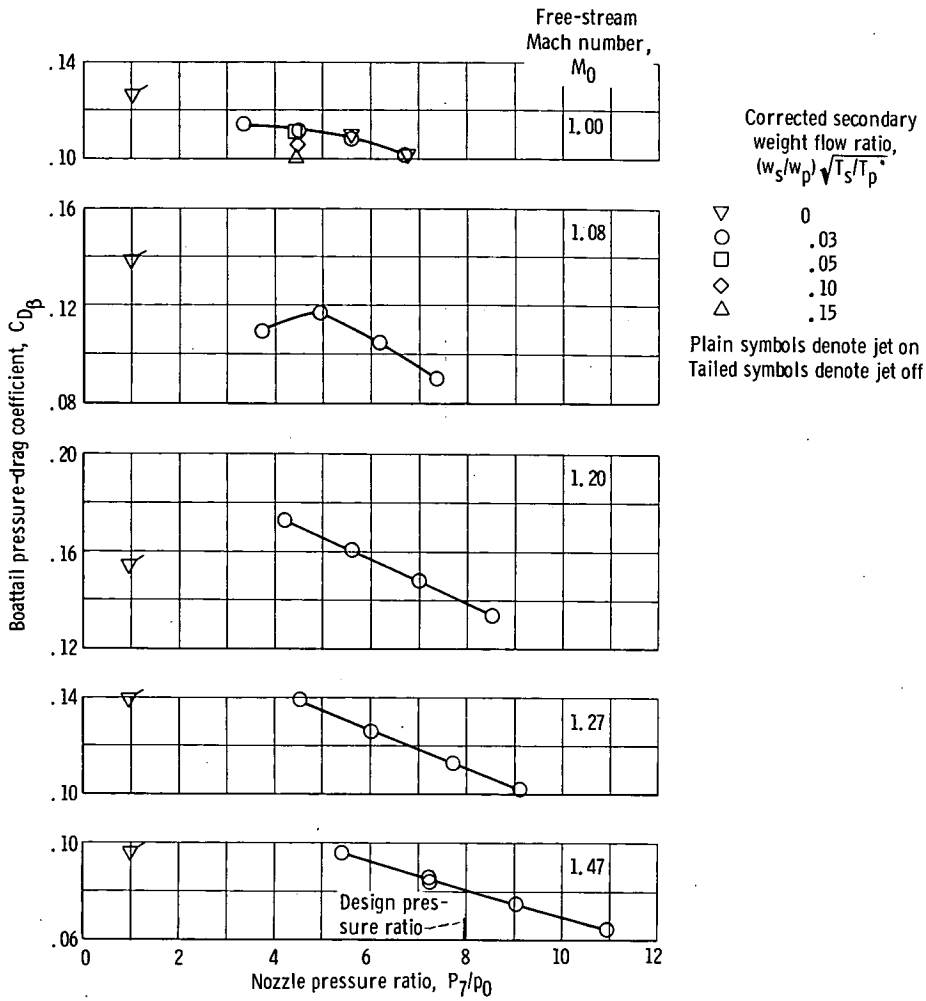

(e) Concluded.

Figure 7. - Continued.

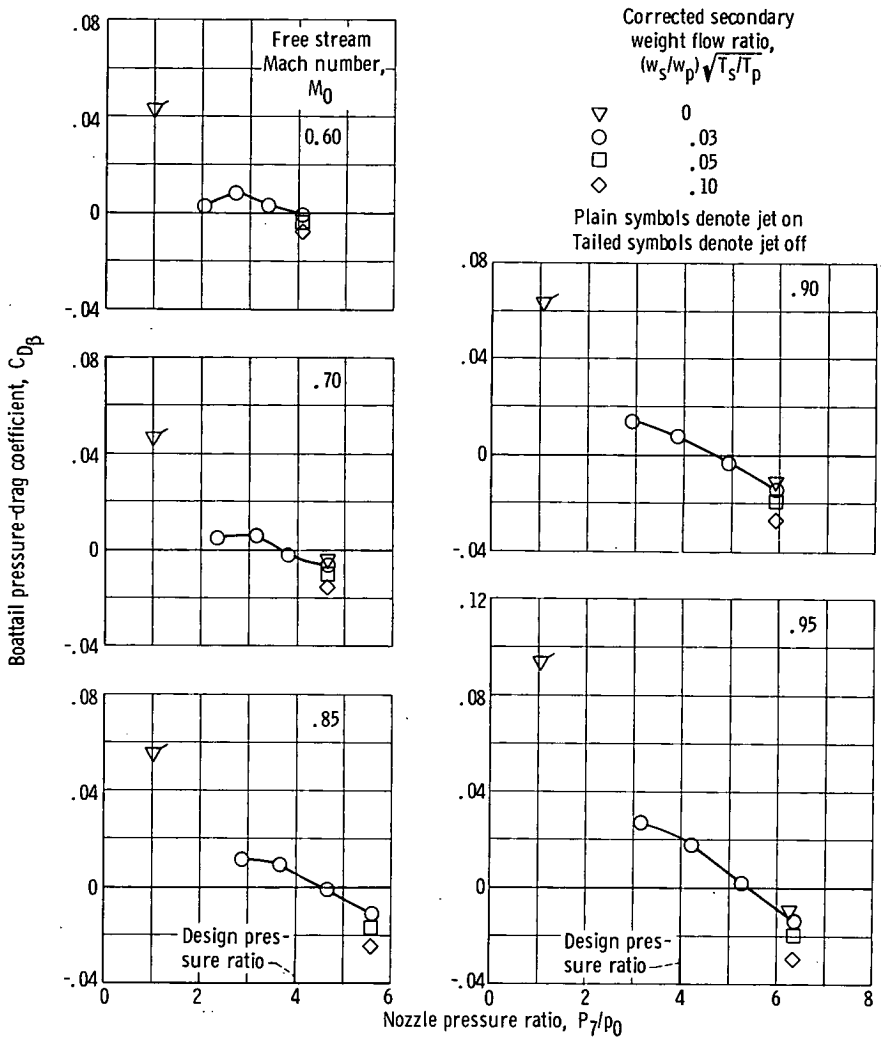

(f) Boattail angle, 15°; radius ratio, 2.5; primary II; nozzle exit to throat area ratio, 1.22.

Figure 7. - Continued.

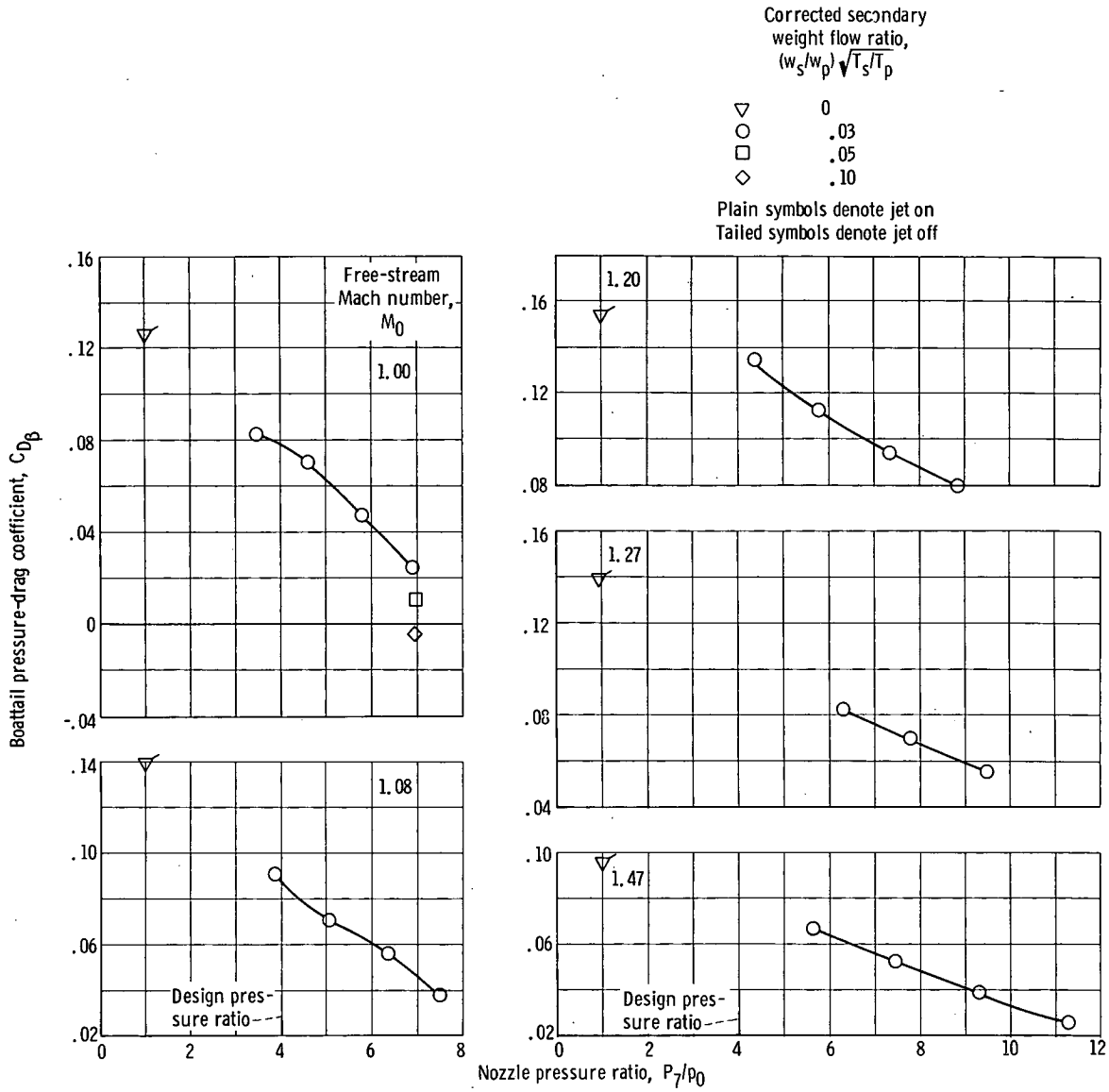

(f) Concluded.

Figure 7. - Continued.

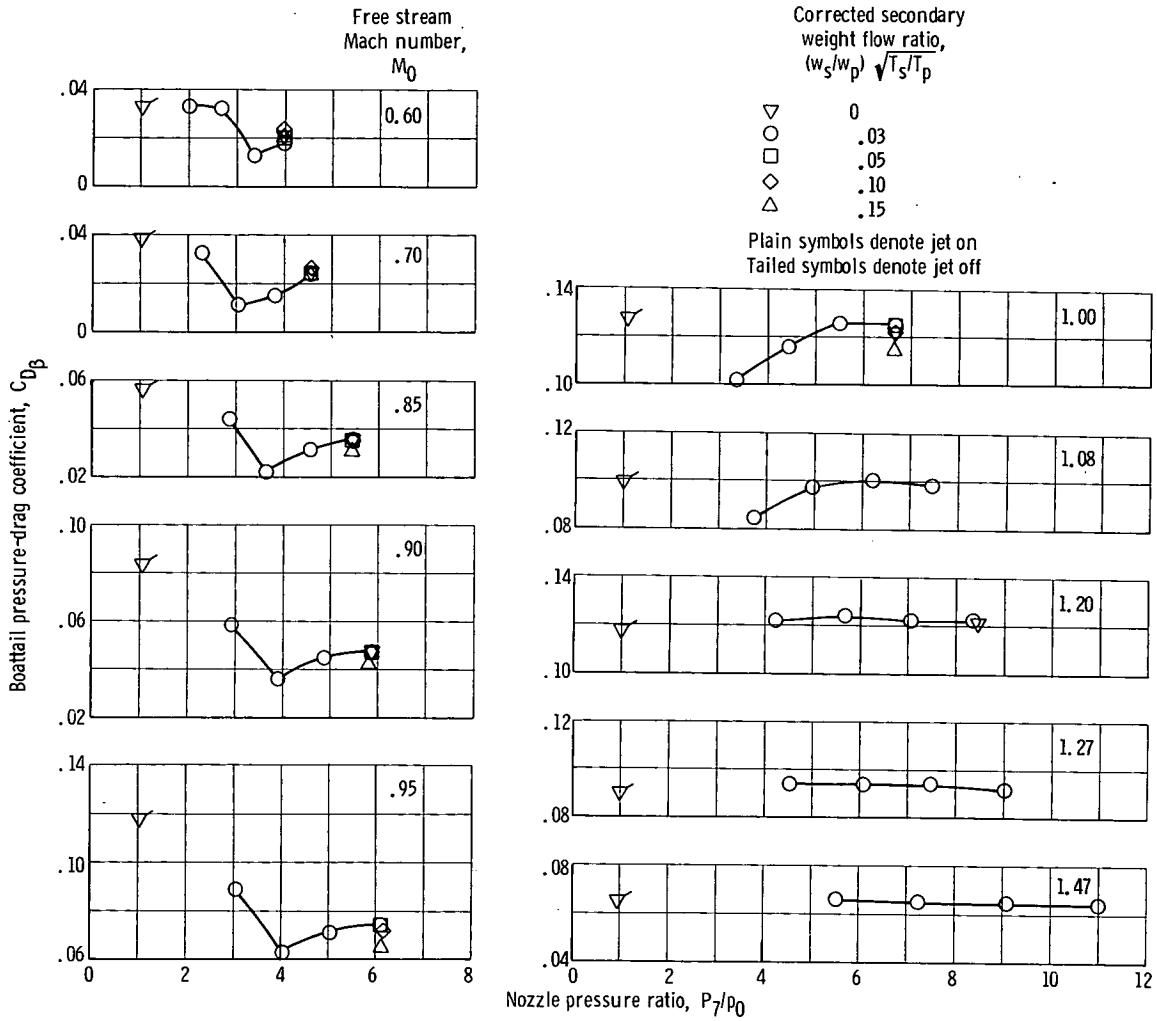

(g) Boattail angle, 10°; radius ratio, 0.5; primary I; nozzle exit to throat area ratio, 2.29; design nozzle pressure ratio, 13.5.

Figure 7. - Continued.

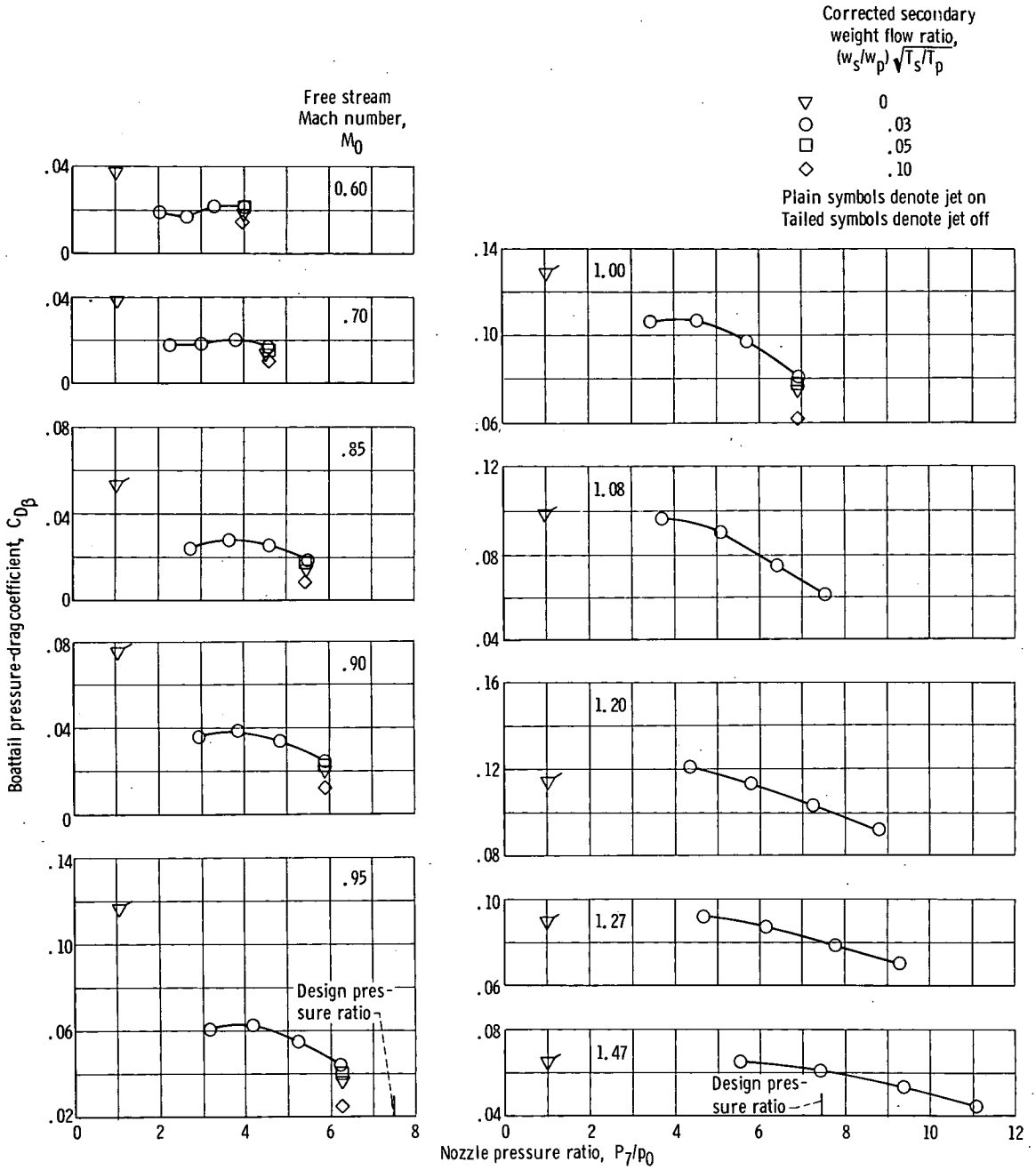

(h) Boattail angle, 10°; radius ratio, 0.5; primary II; nozzle exit to throat area ratio, 1.64.

Figure 7. - Concluded.

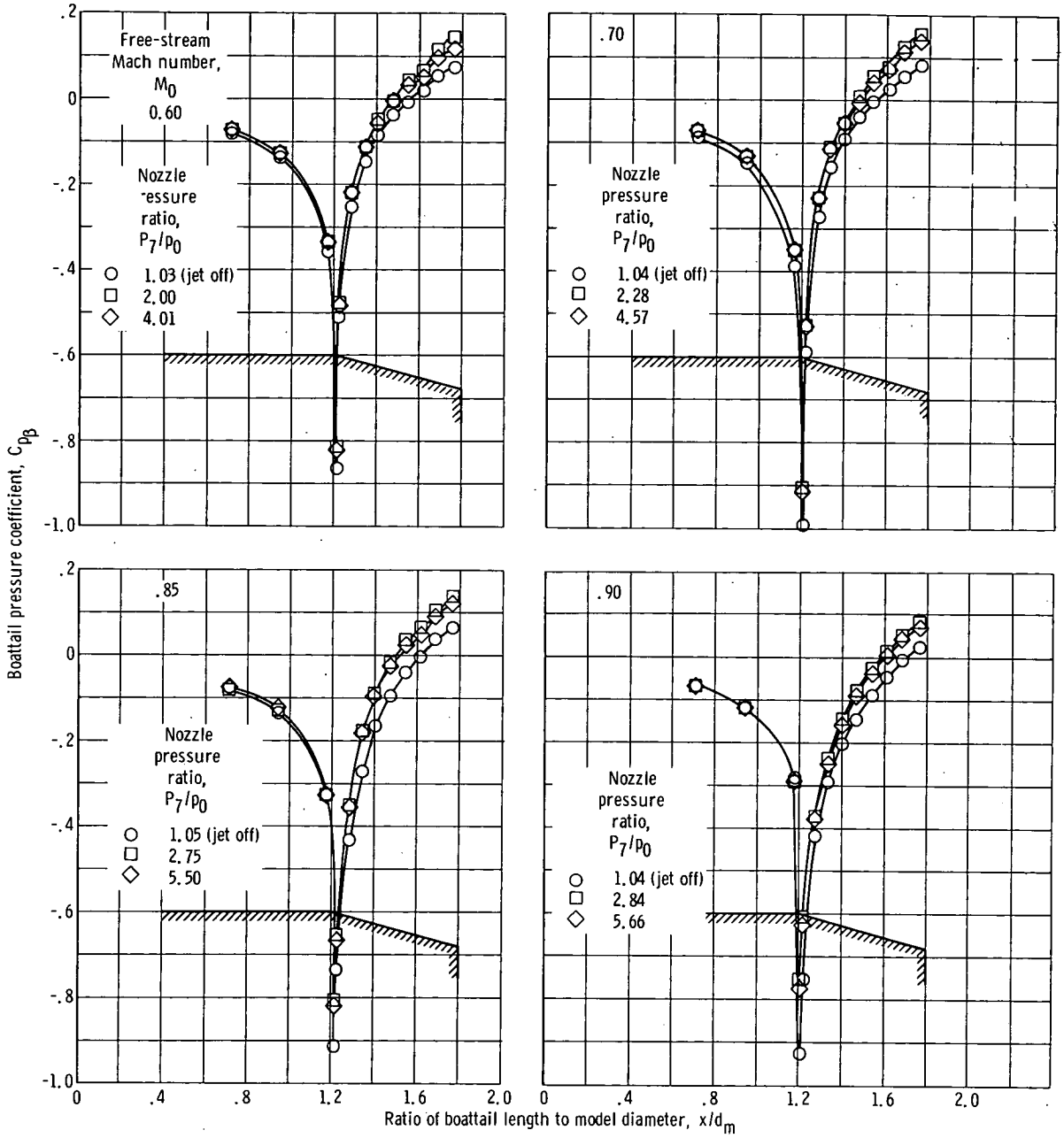

(a) Boattail angle 15°; radius ratio, 0; primary I; nozzle exit to throat area ratio, 1.70.

Figure 8. - Effect of nozzle pressure ratio on boattail pressure distributions. Corrected secondary weight flow ratio, 0.03.

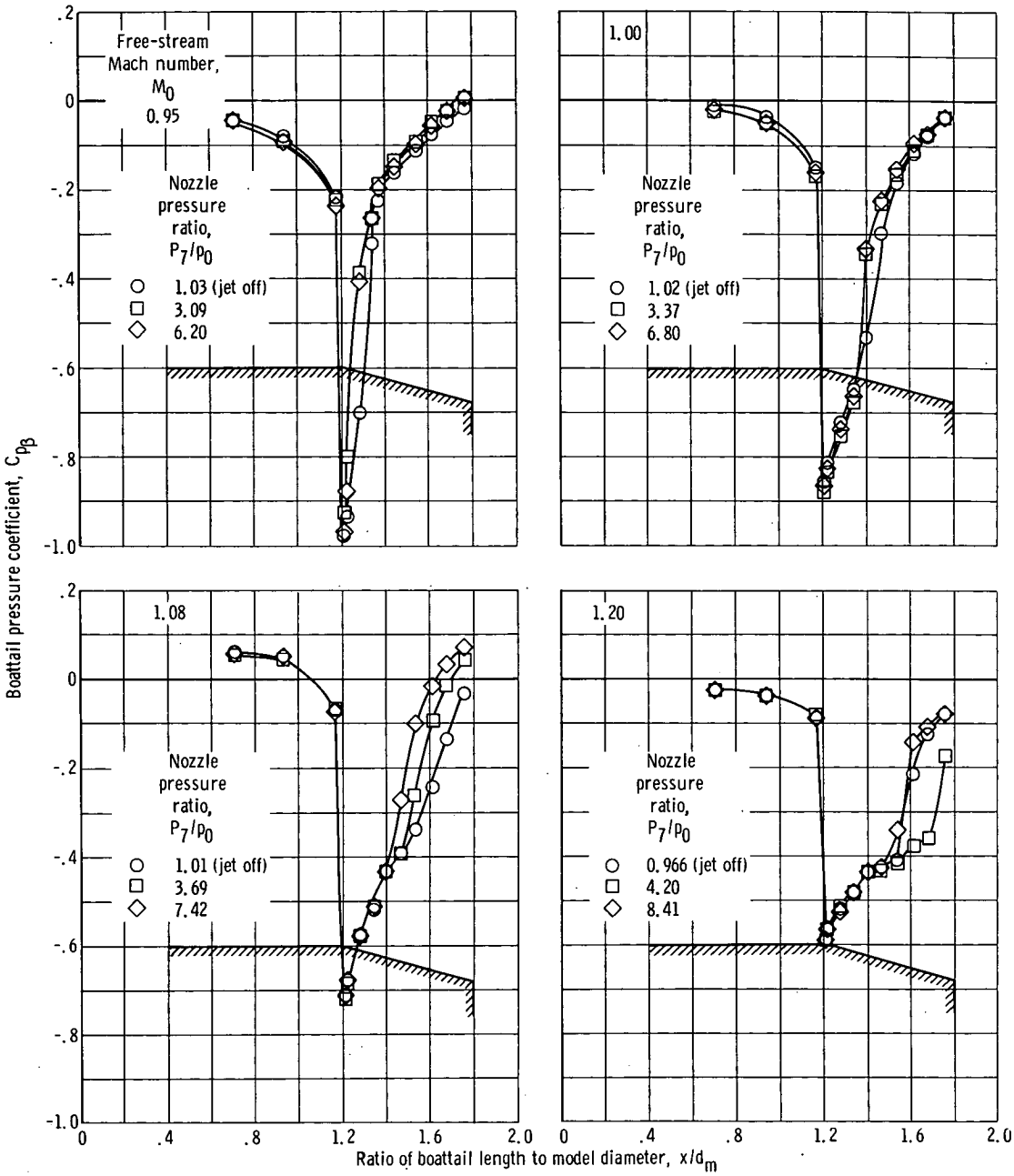

(a) Continued.

Figure 8. - Continued.

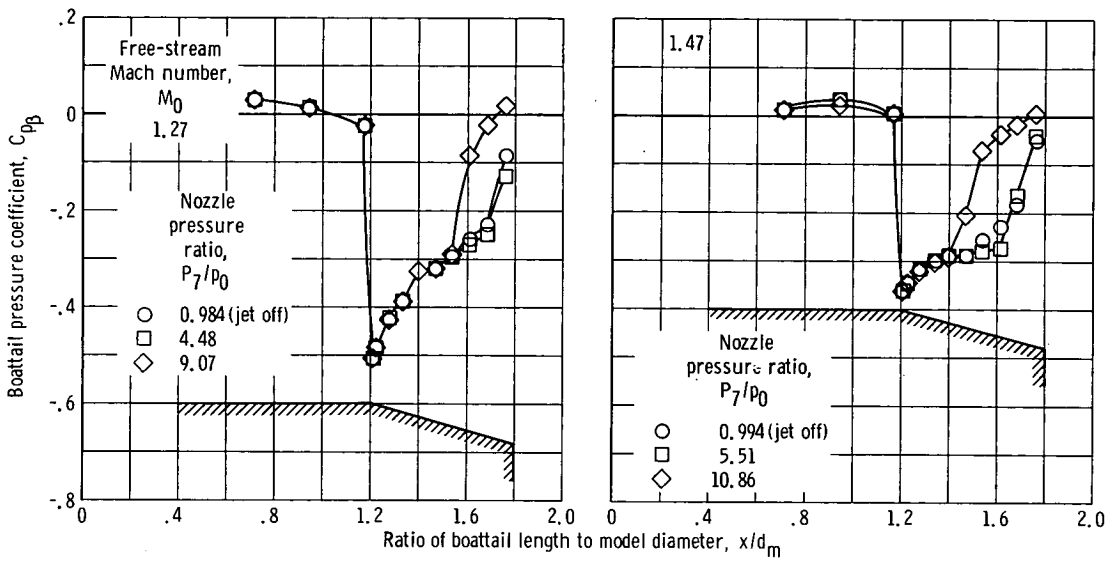

(a) Concluded.

Figure 8. - Continued.

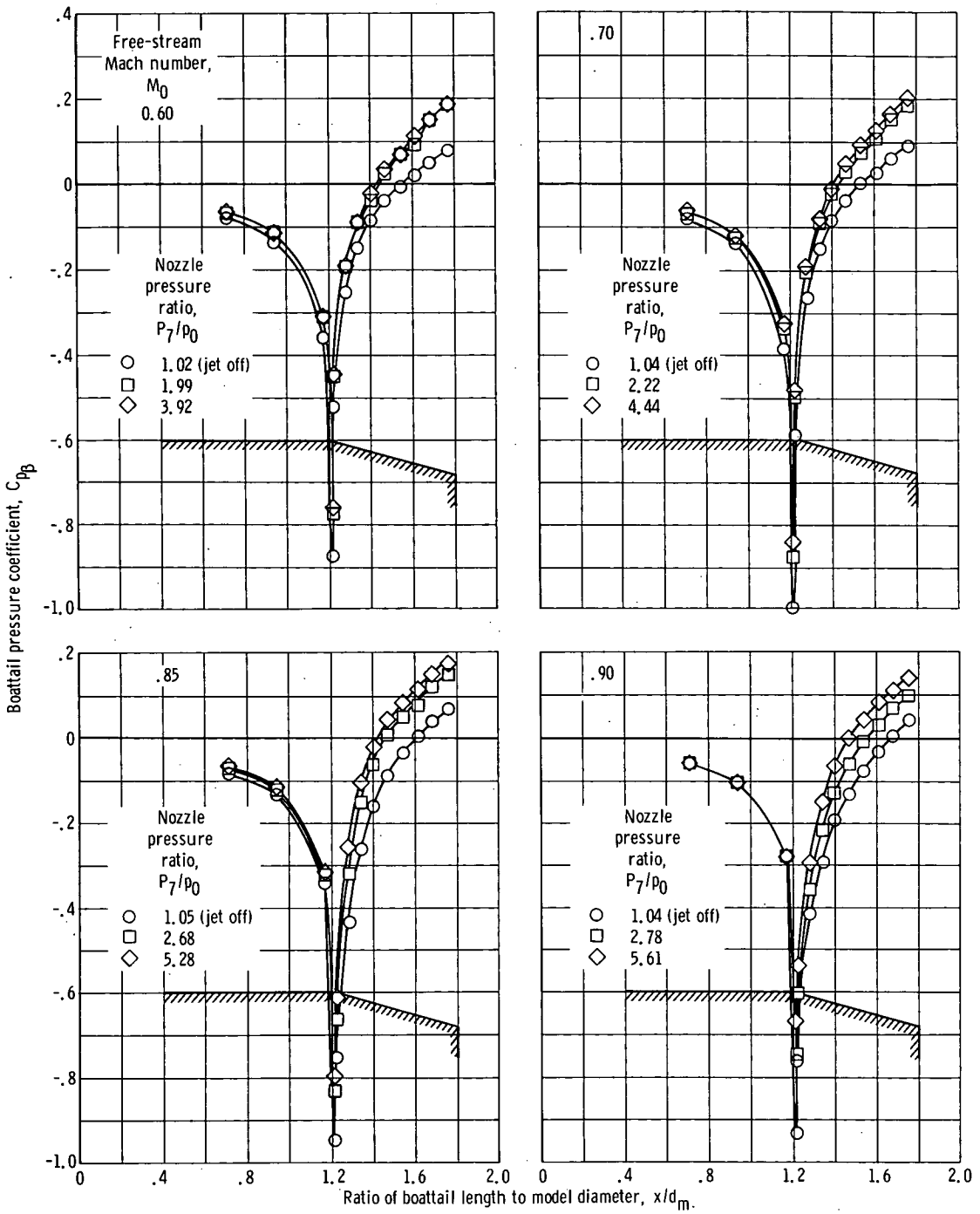

(b) Boattail angle, 15°; radius ratio, 0; primary II; nozzle exit to throat area ratio, 1.22.

Figure 8. - Continued.

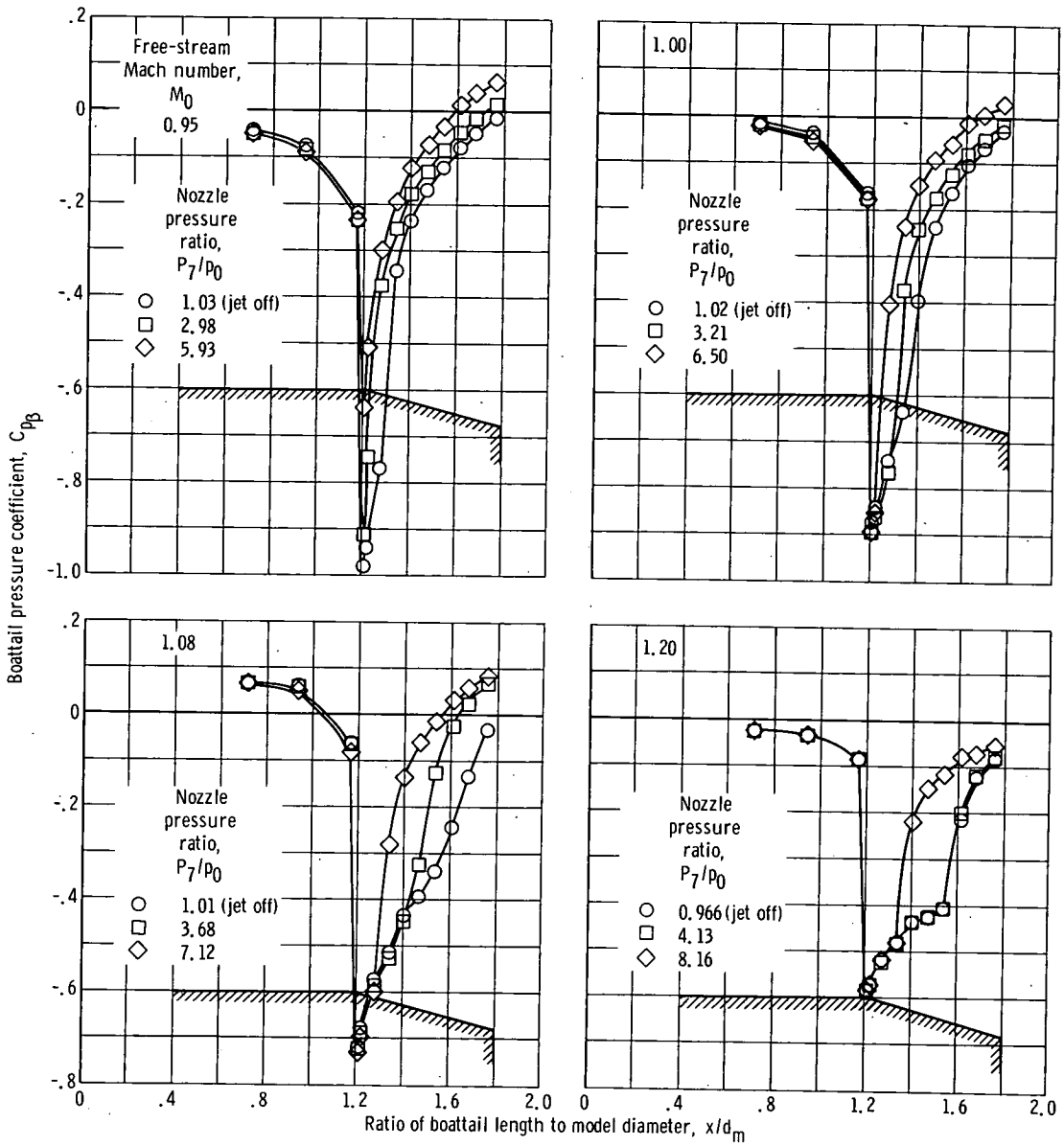

(b) Continued.

Figure 8. - Continued.

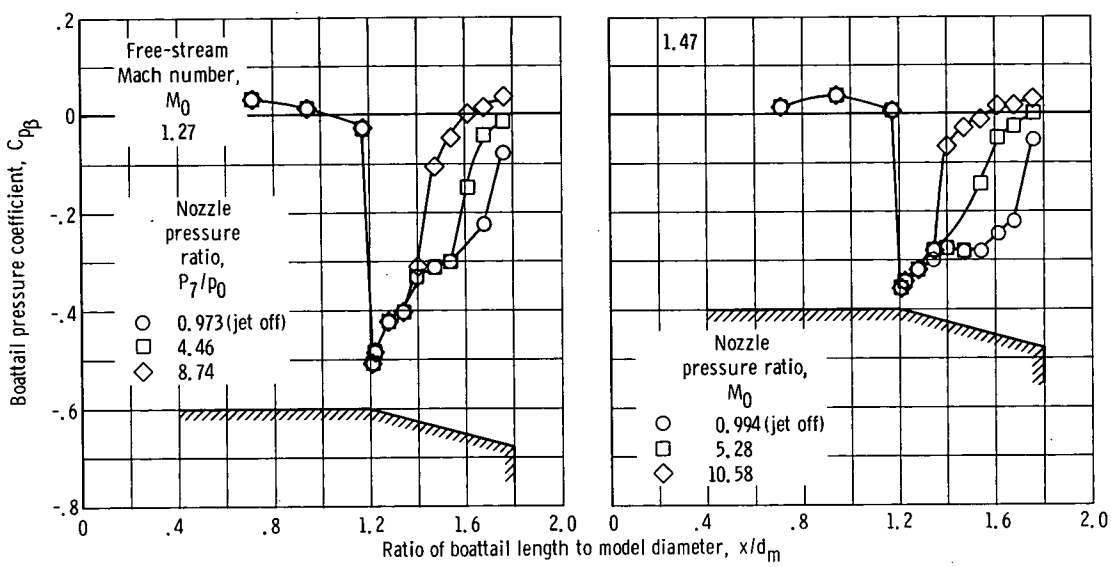

(b) Concluded.

Figure 8. - Continued.

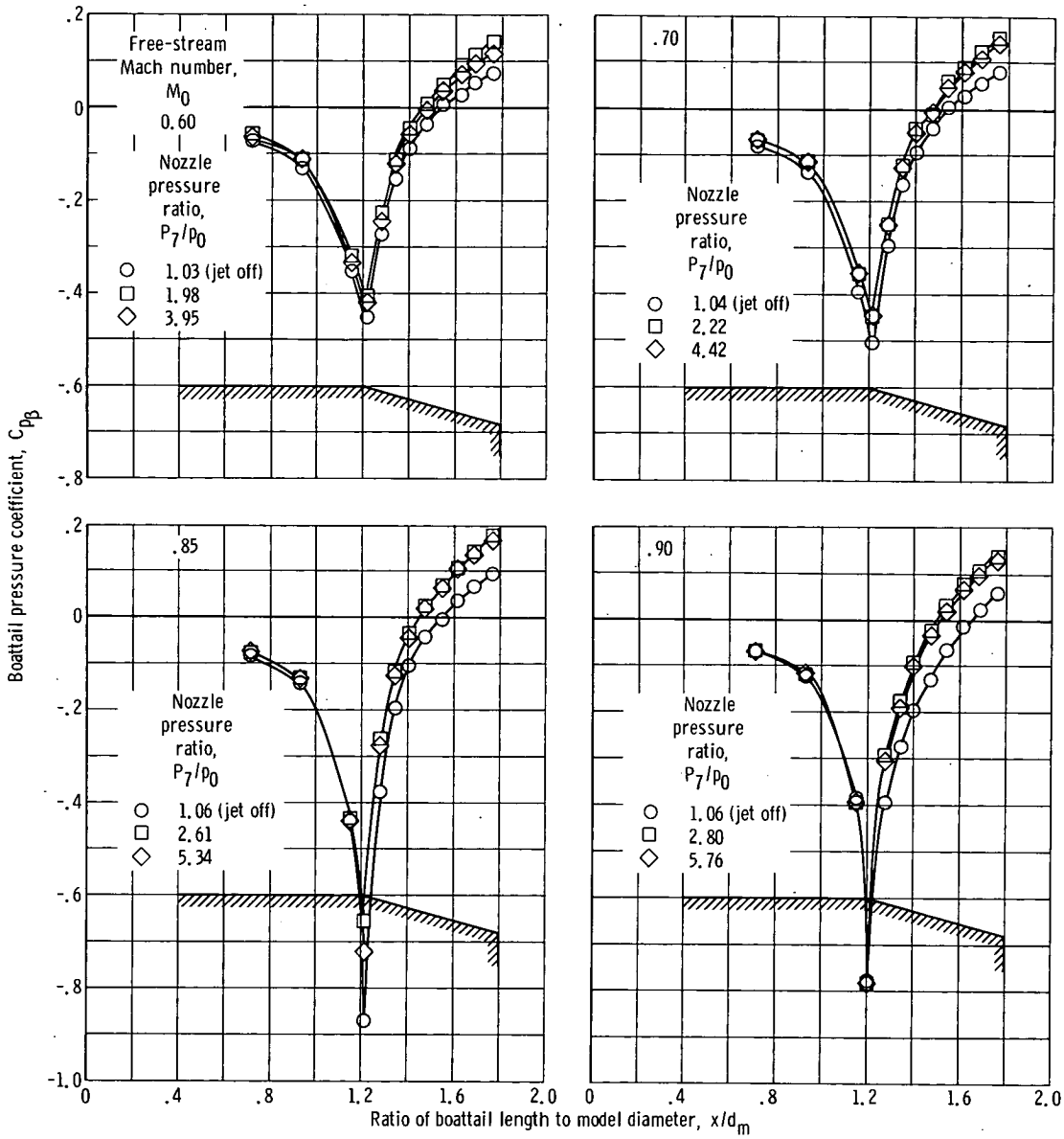

(c) Boattail angle, 15°; radius ratio, 0.5; primary I; nozzle exit to throat area ratio, 1.70.

Figure 8. - Continued.

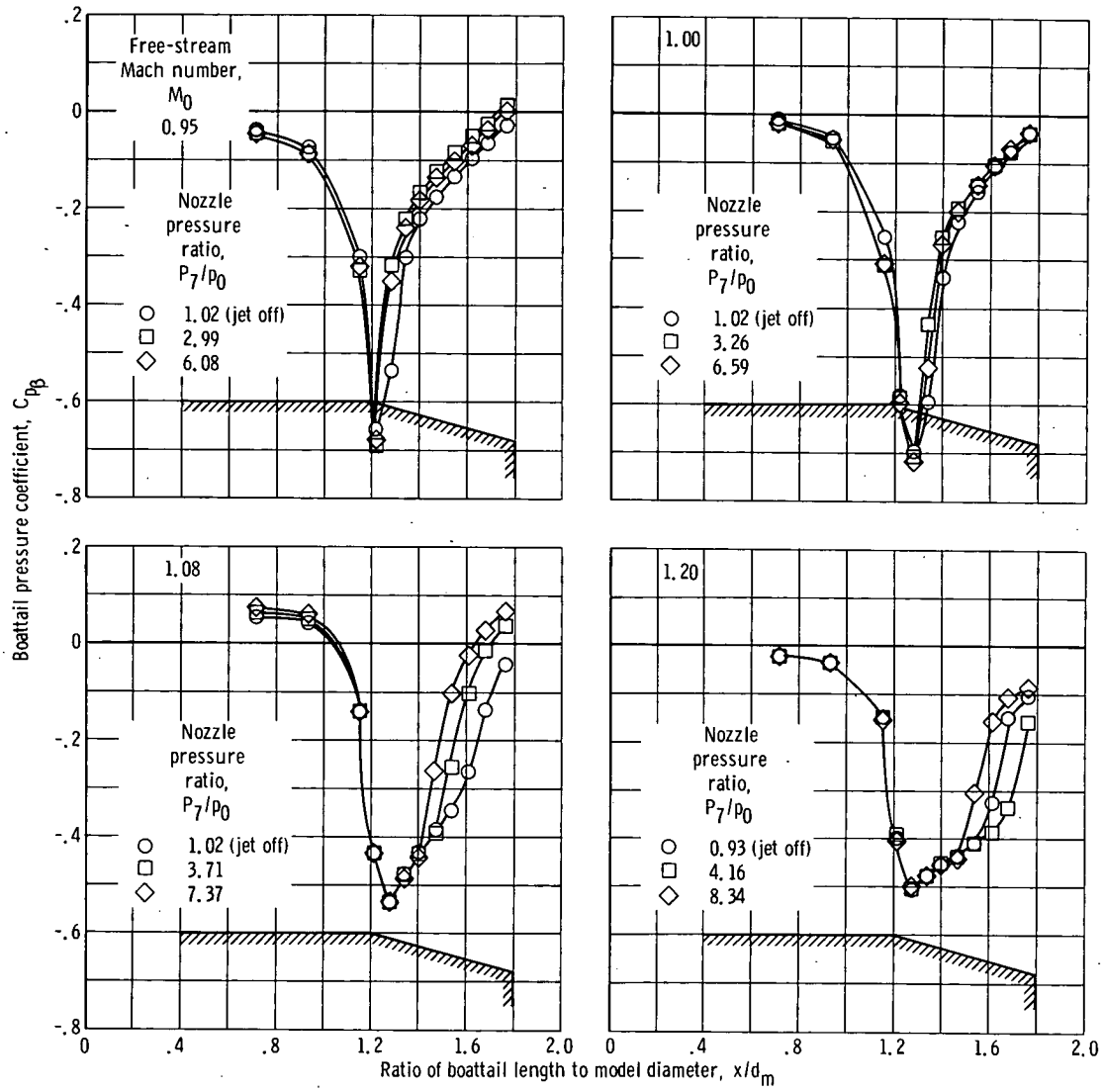

(c) Continued.

Figure 8. - Continued.

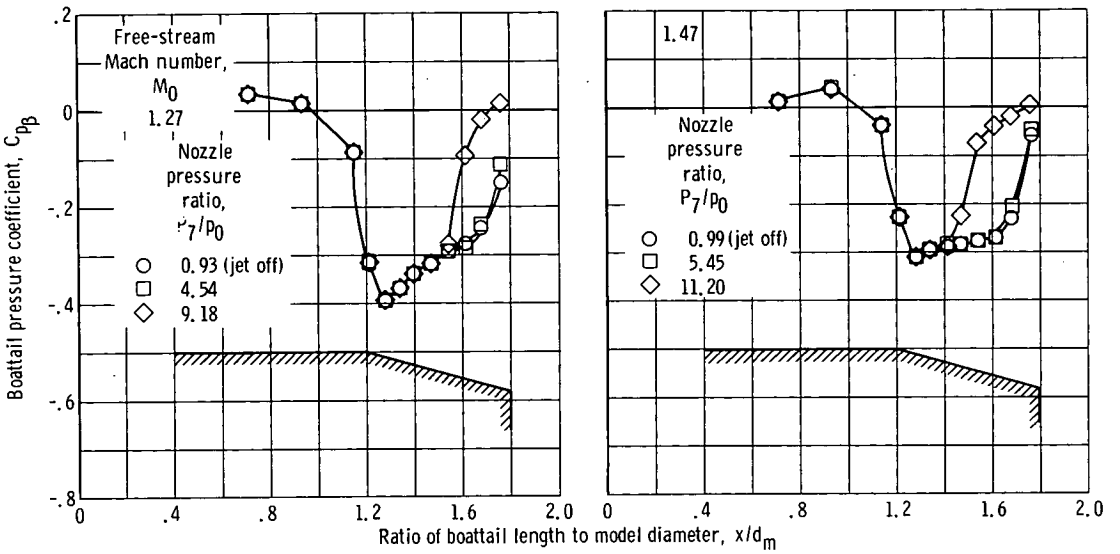

(c) Concluded.

Figure 8. - Continued.

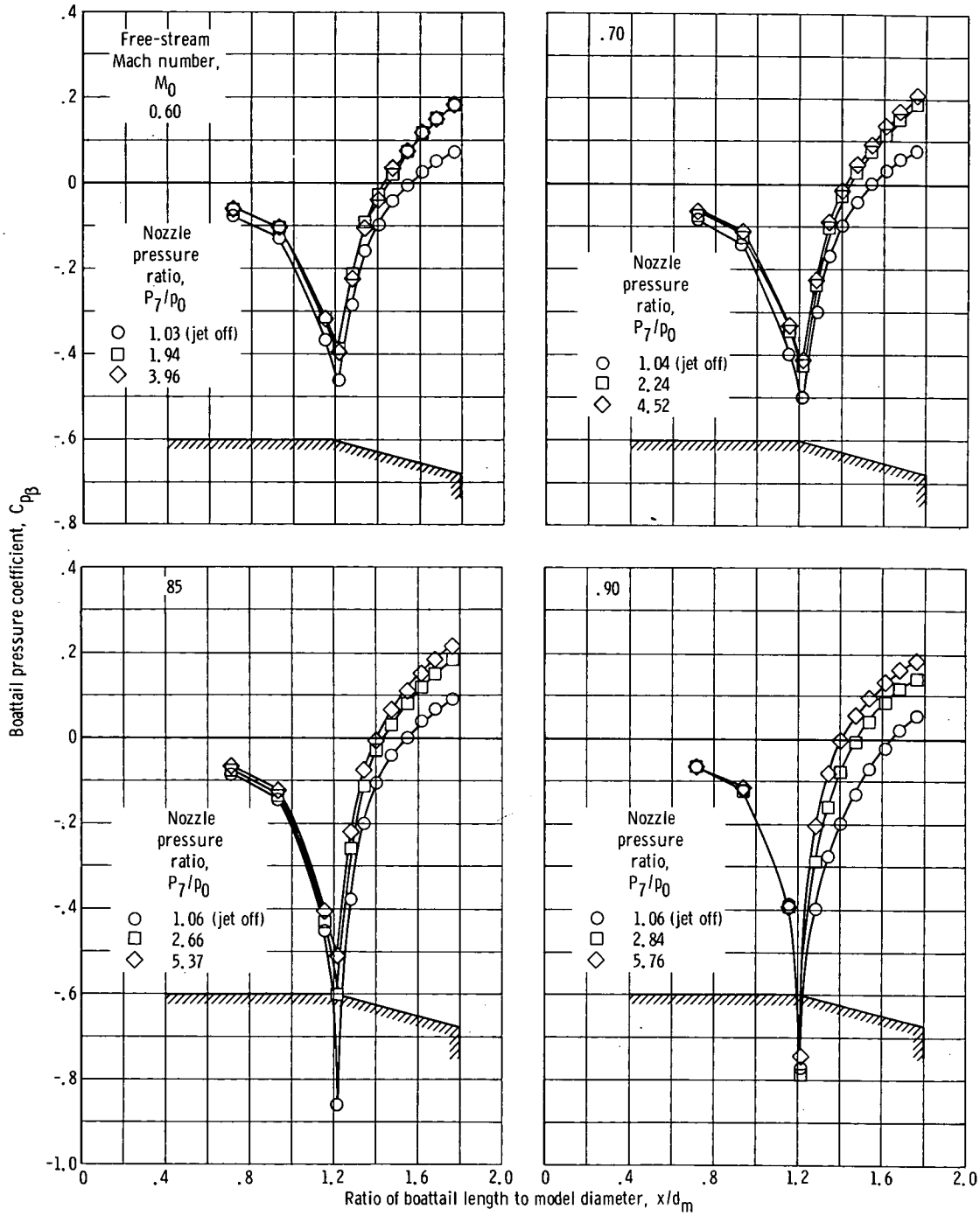

(d) Boattail angle, 15°; radius ratio, 0.5; primary II; nozzle exit to throat area ratio, 1.22.

Figure 8. - Continued.

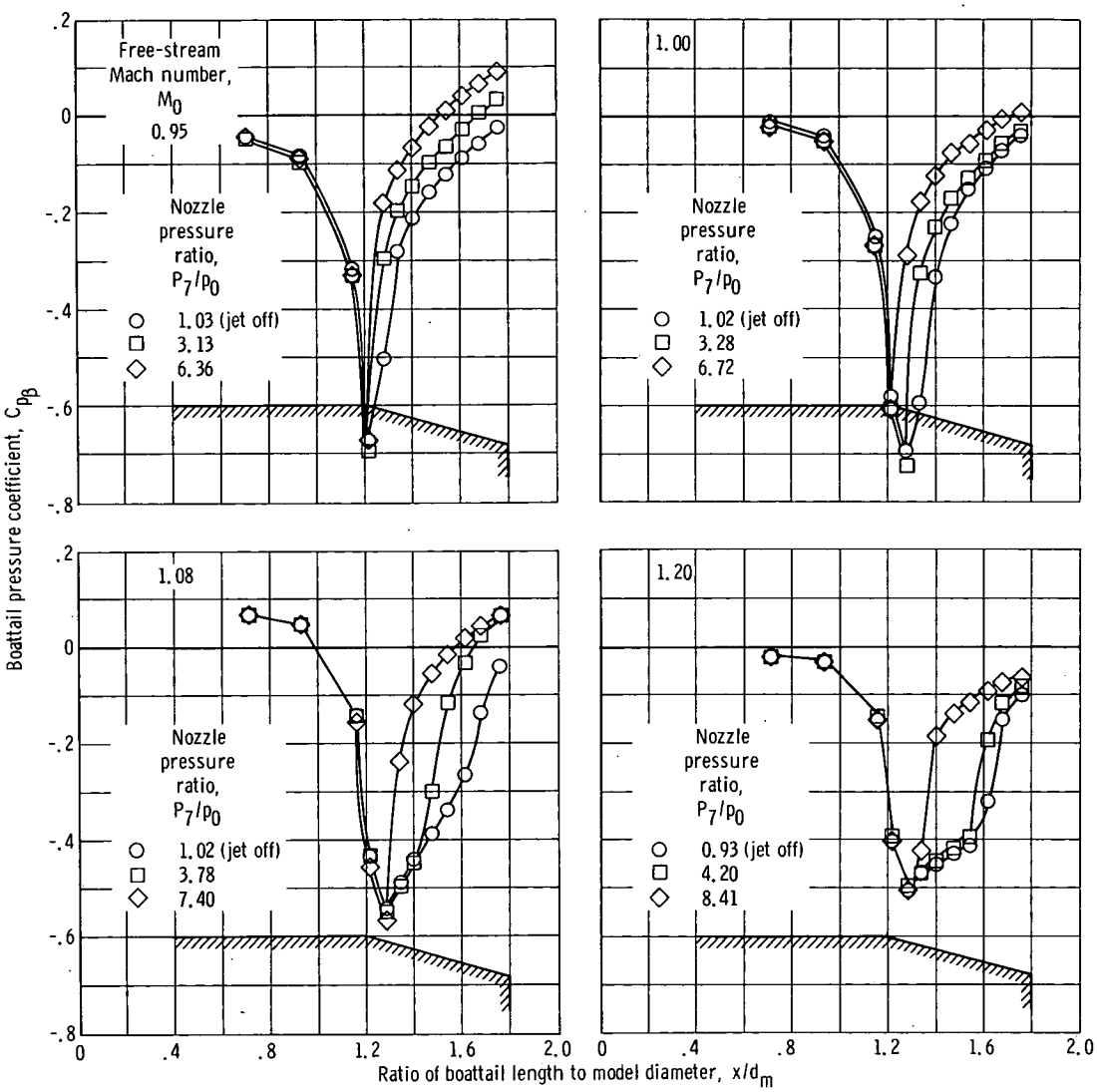

(d) Continued.

Figure 8. - Continued.

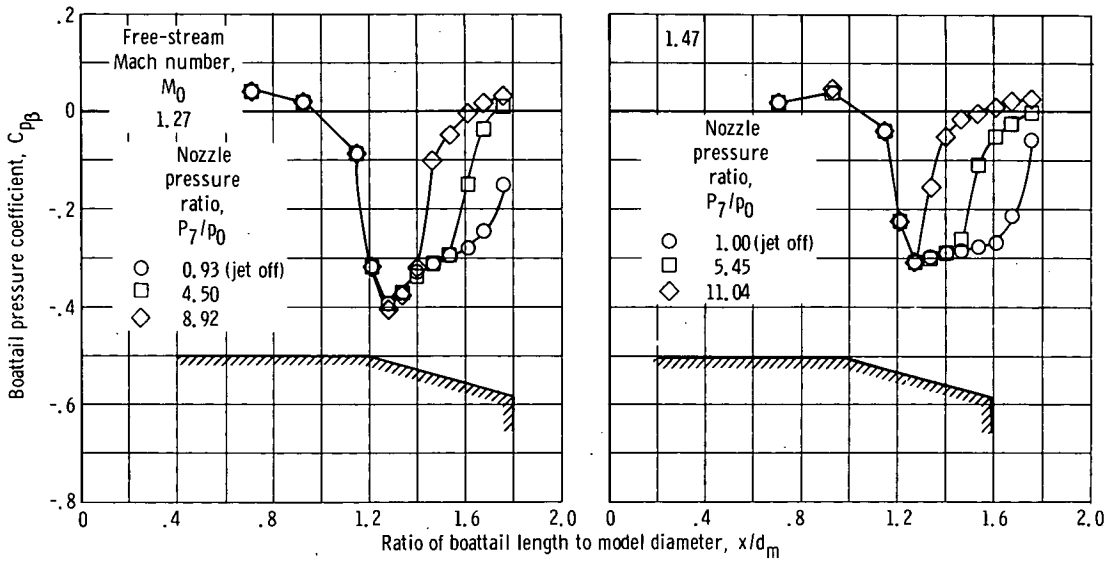

(d) Concluded.

Figure 8. - Continued.

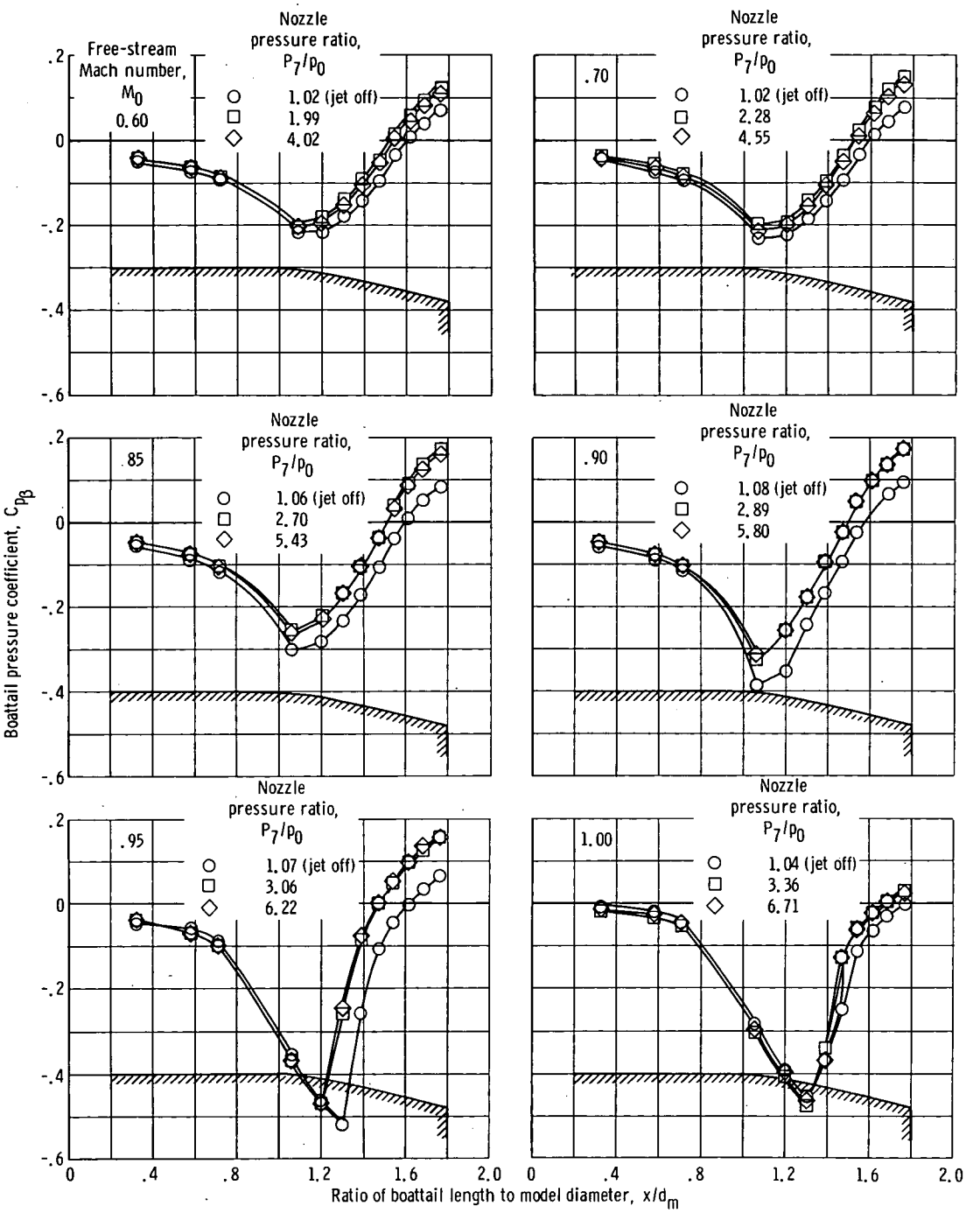

(e) Boattail angle, 15°; radius ratio, 2.5; primary I; nozzle exit to throat area ratio, 1.70.

Figure 8. - Continued.

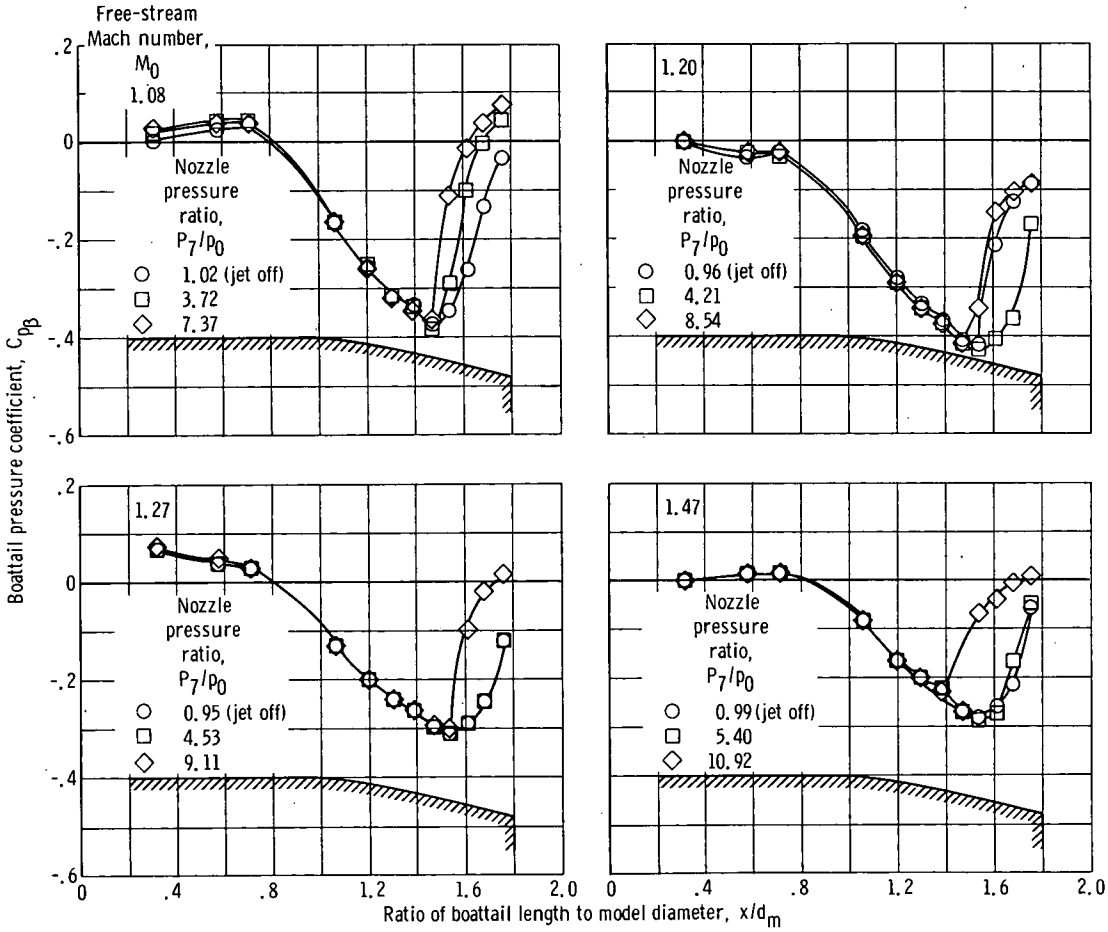

(e) Concluded.

Figure 8. - Continued.

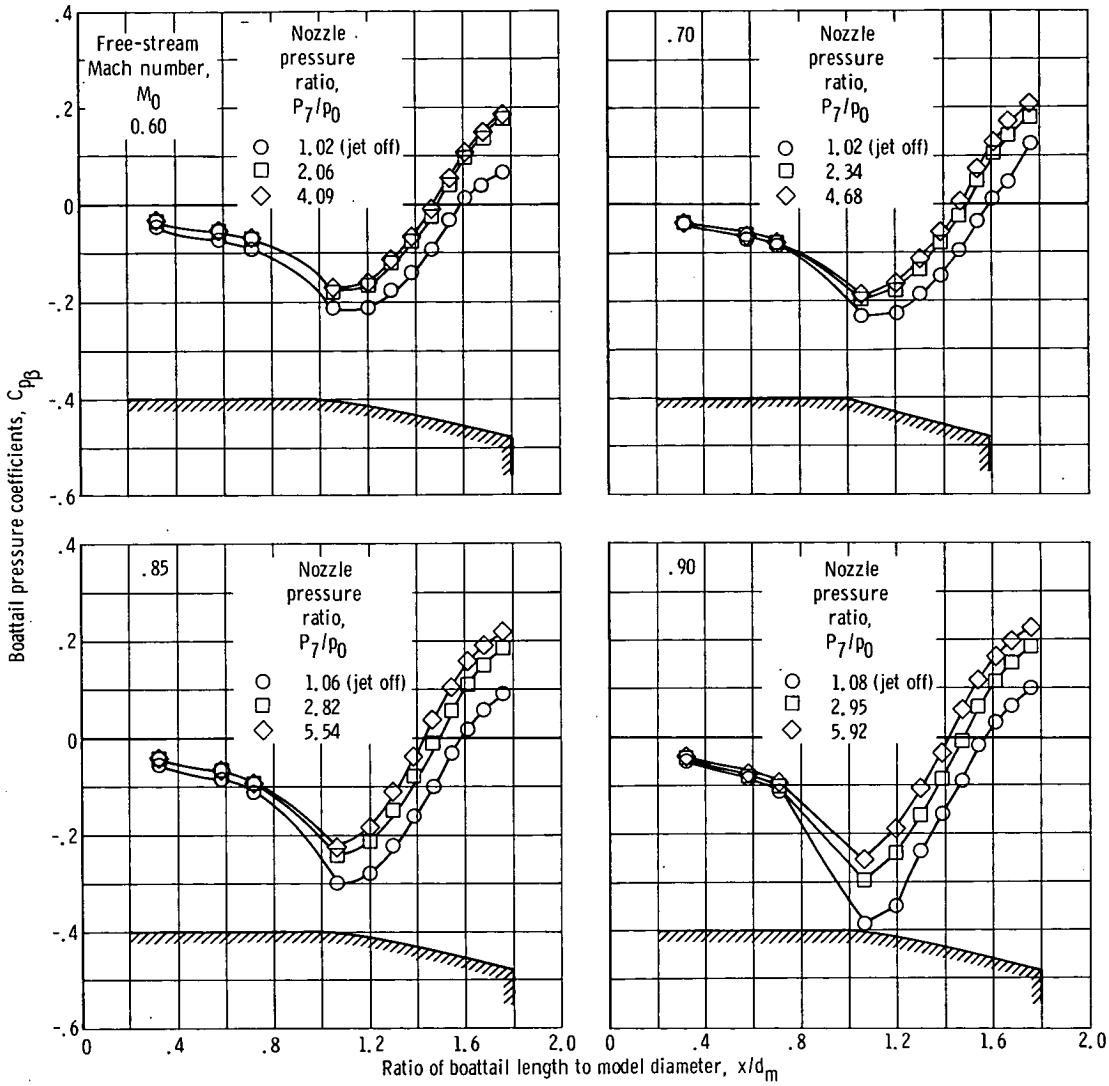

(f) Boattail angle, 15°; radius ratio, 2.5; primary II; nozzle exit to throat area ratio, 1.22.

Figure 8. - Continued.

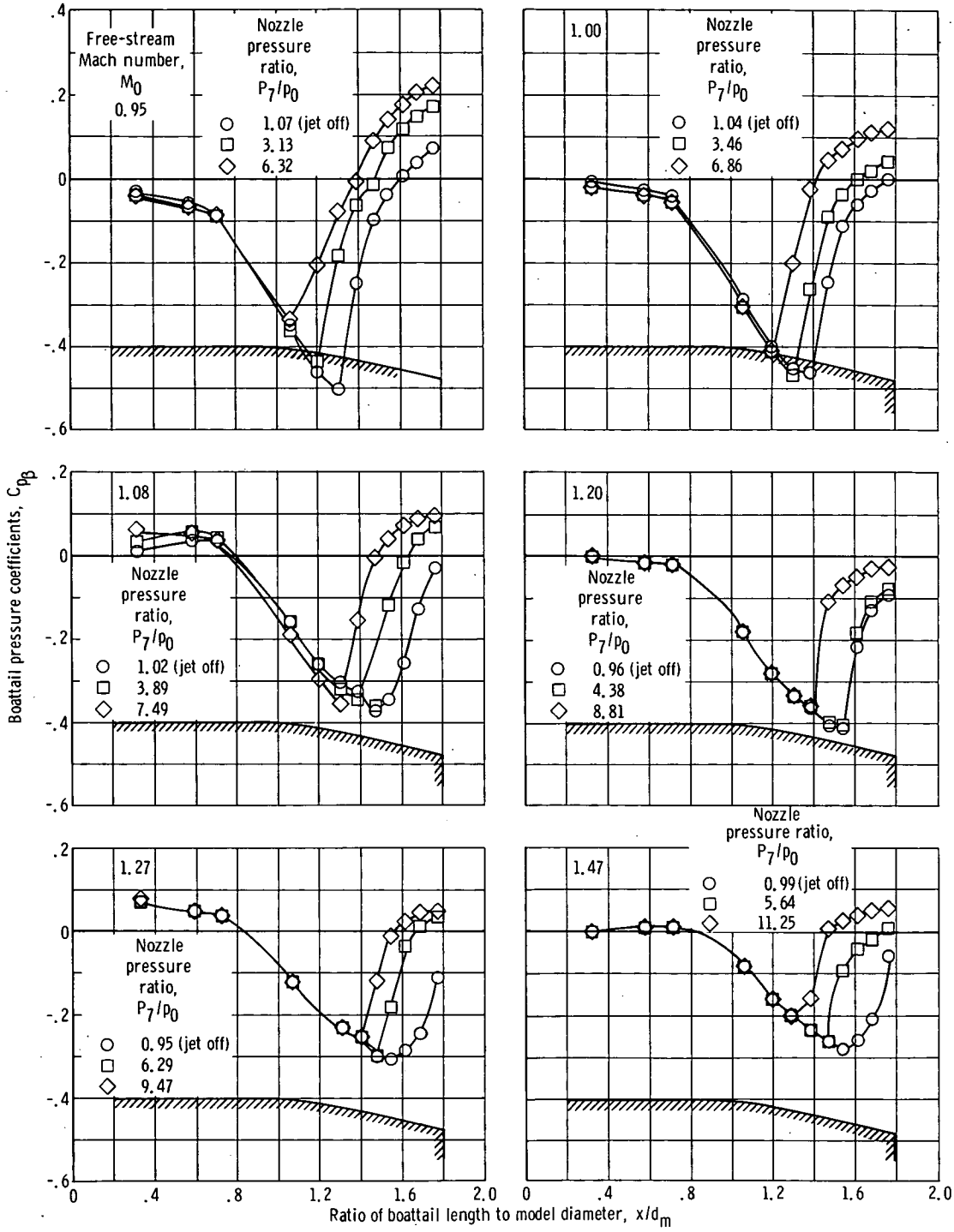

(f) Concluded.

Figure 8. - Continued.

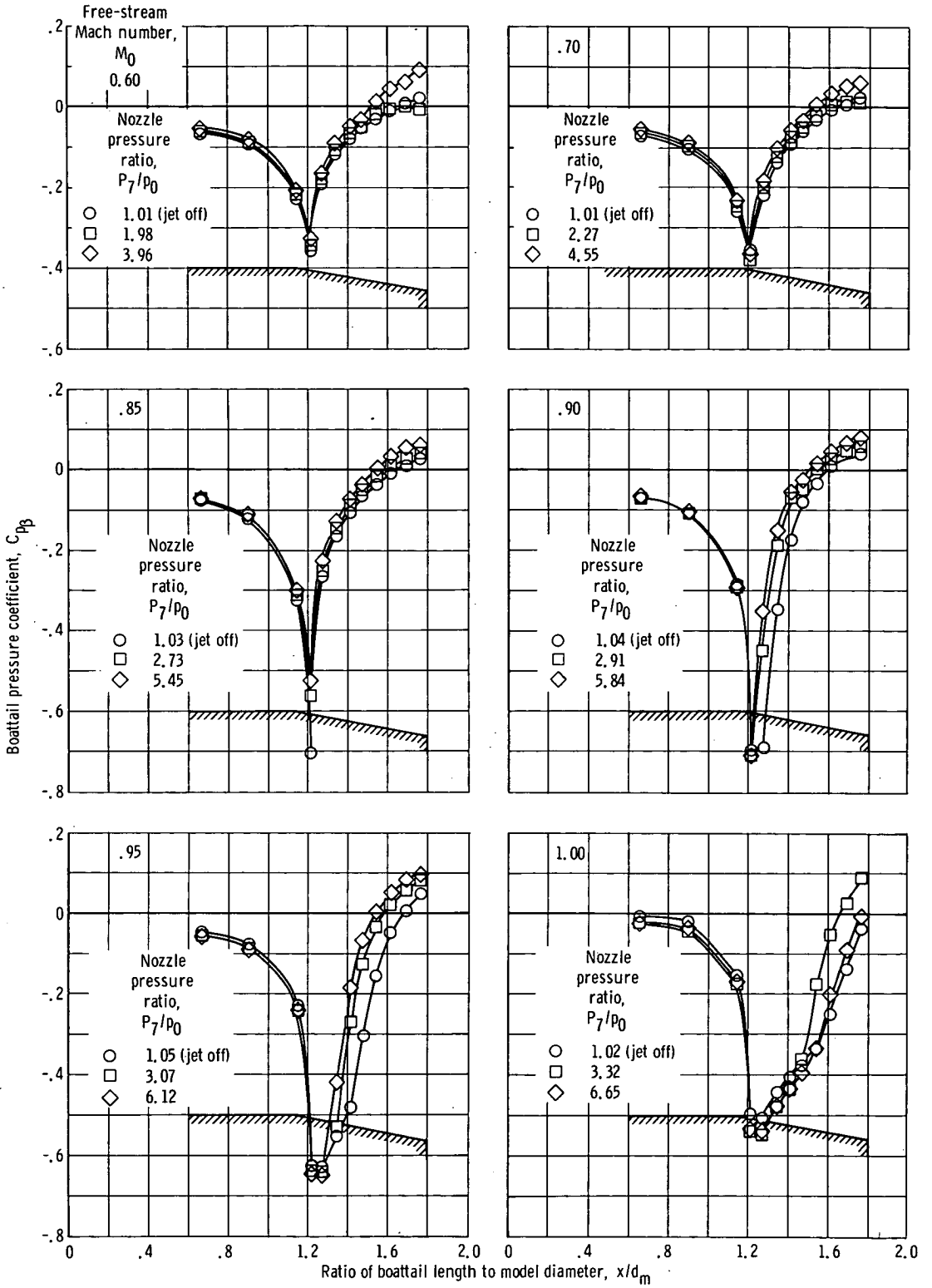

(g) Boattail angle, 10°; radius ratio, 0.5; primary I; nozzle exit to throat area ratio, 2.29.

Figure 8. - Continued.

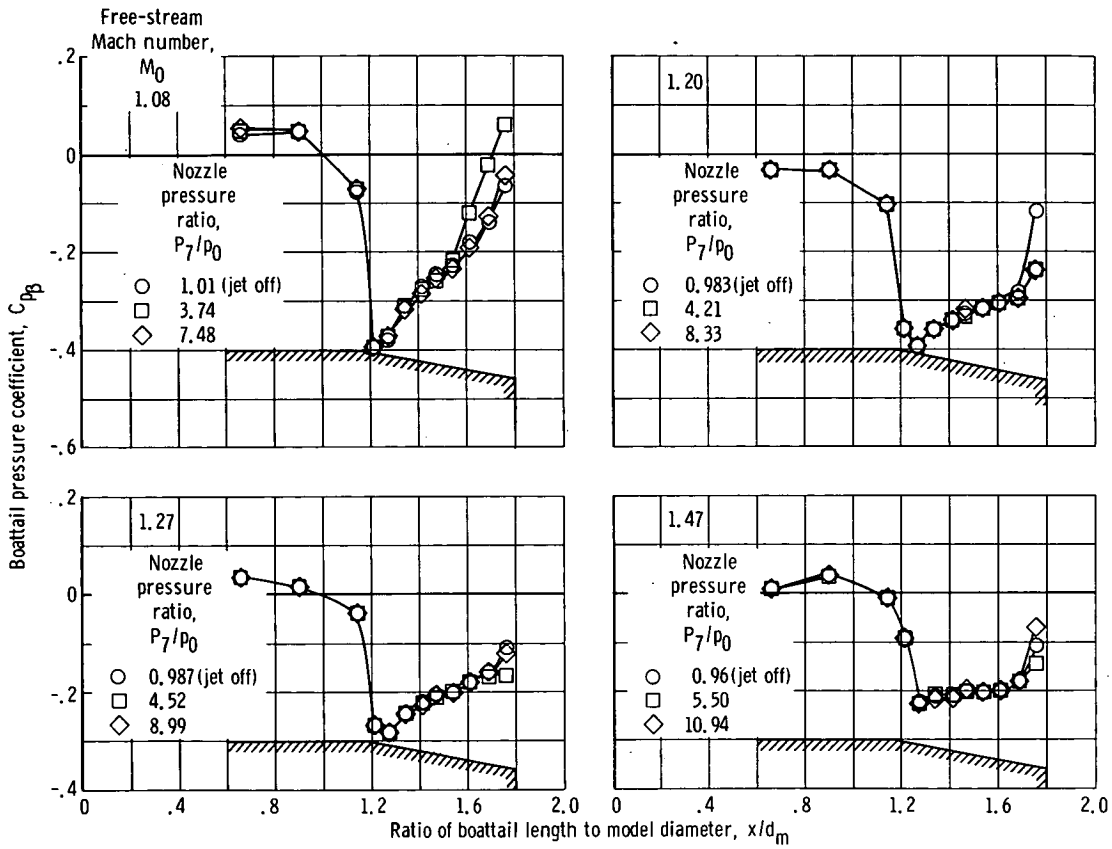

(g) Concluded.

Figure 8. - Continued.

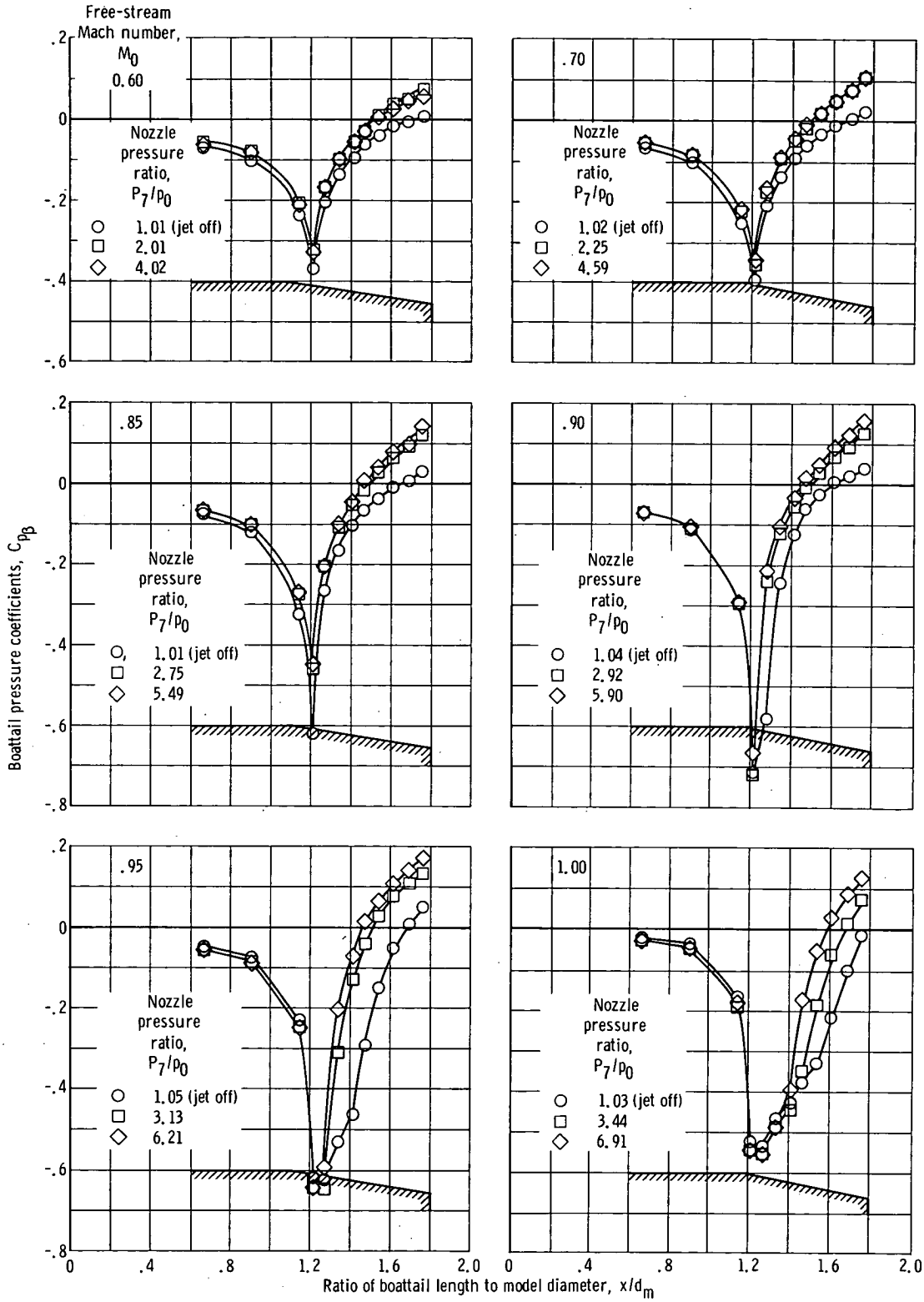

(h) Boattail angle, 10°; radius ratio, 0.5; primary II; nozzle exit to throat area ratio, 1.64.

Figure 8. - Continued.

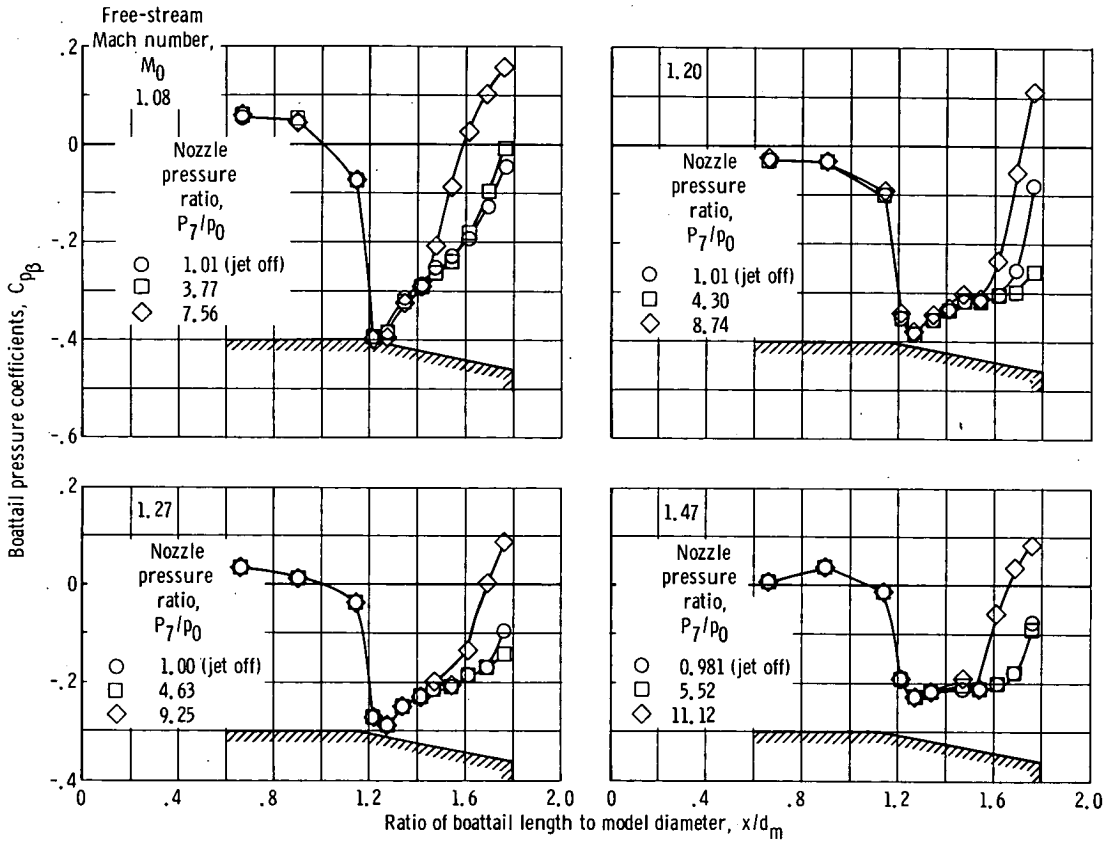

(h) Concluded.

Figure 8. - Concluded.

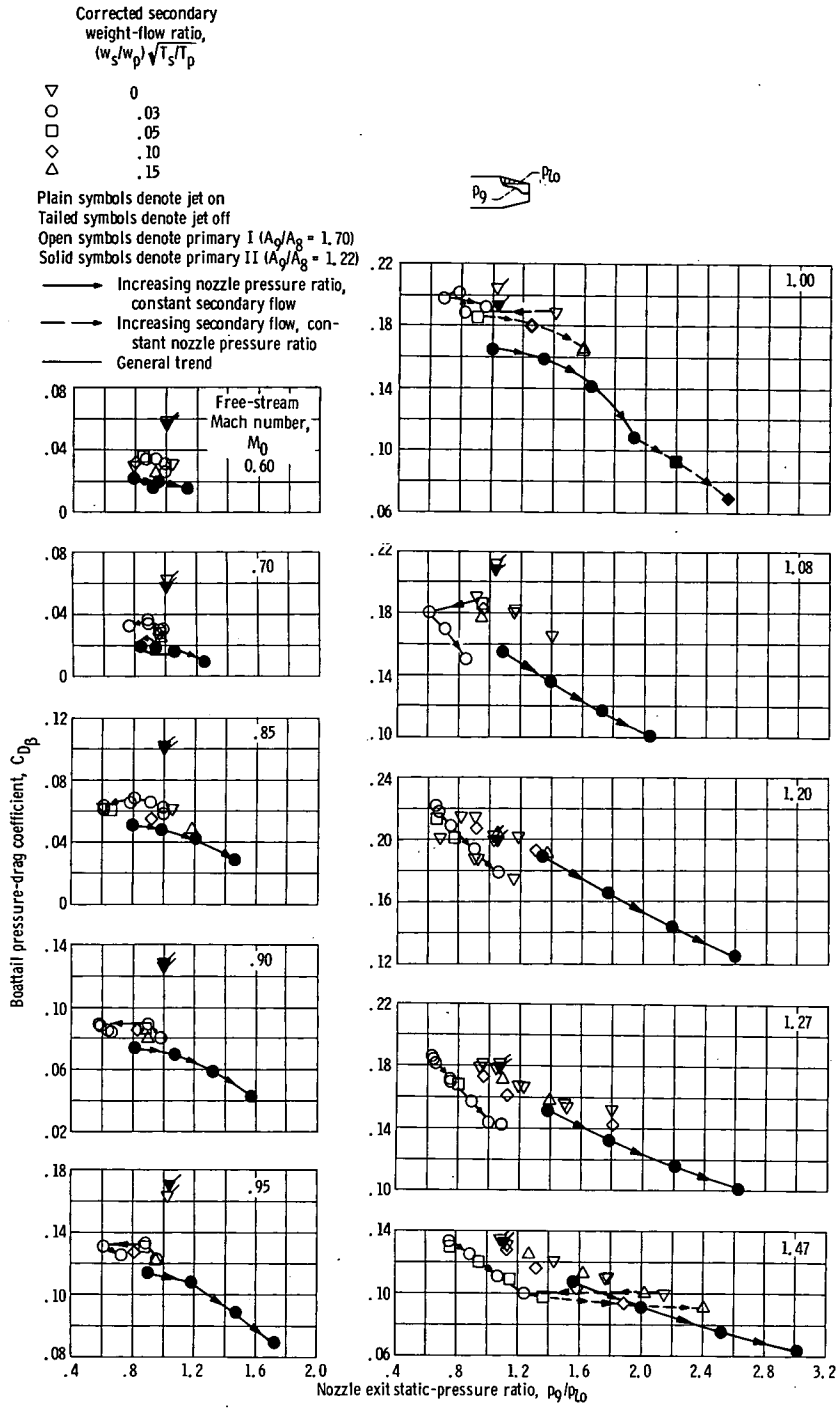

(a) Boattail angle, 15°; radius ratio, 0.

Figure 9. - Effect of nozzle-exit static-pressure ratio on boattail pressure-drag coefficient.

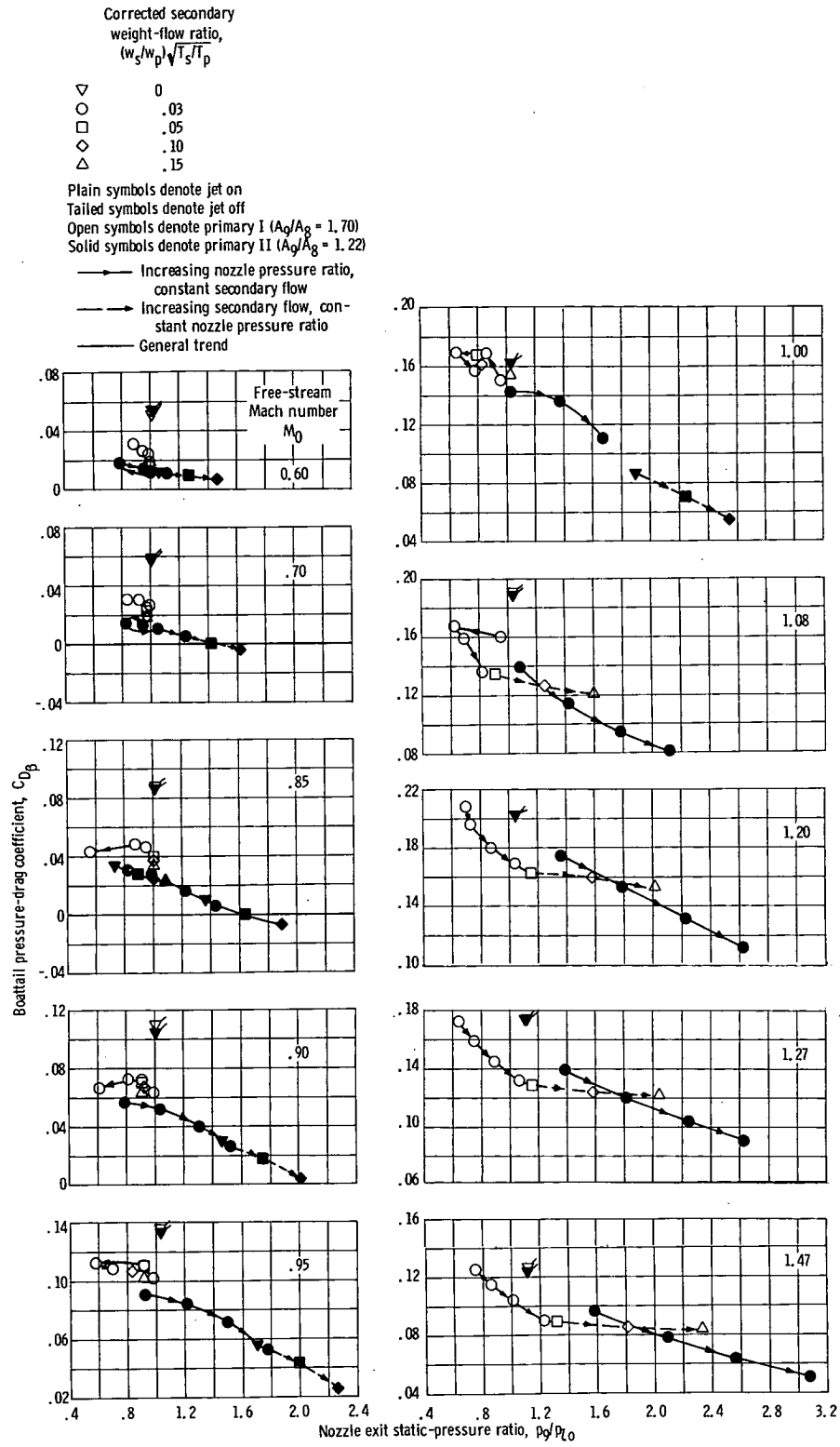

(b) Boattail angle, 15°, radius ratio, 0.5°.

Figure 9. - Continued.

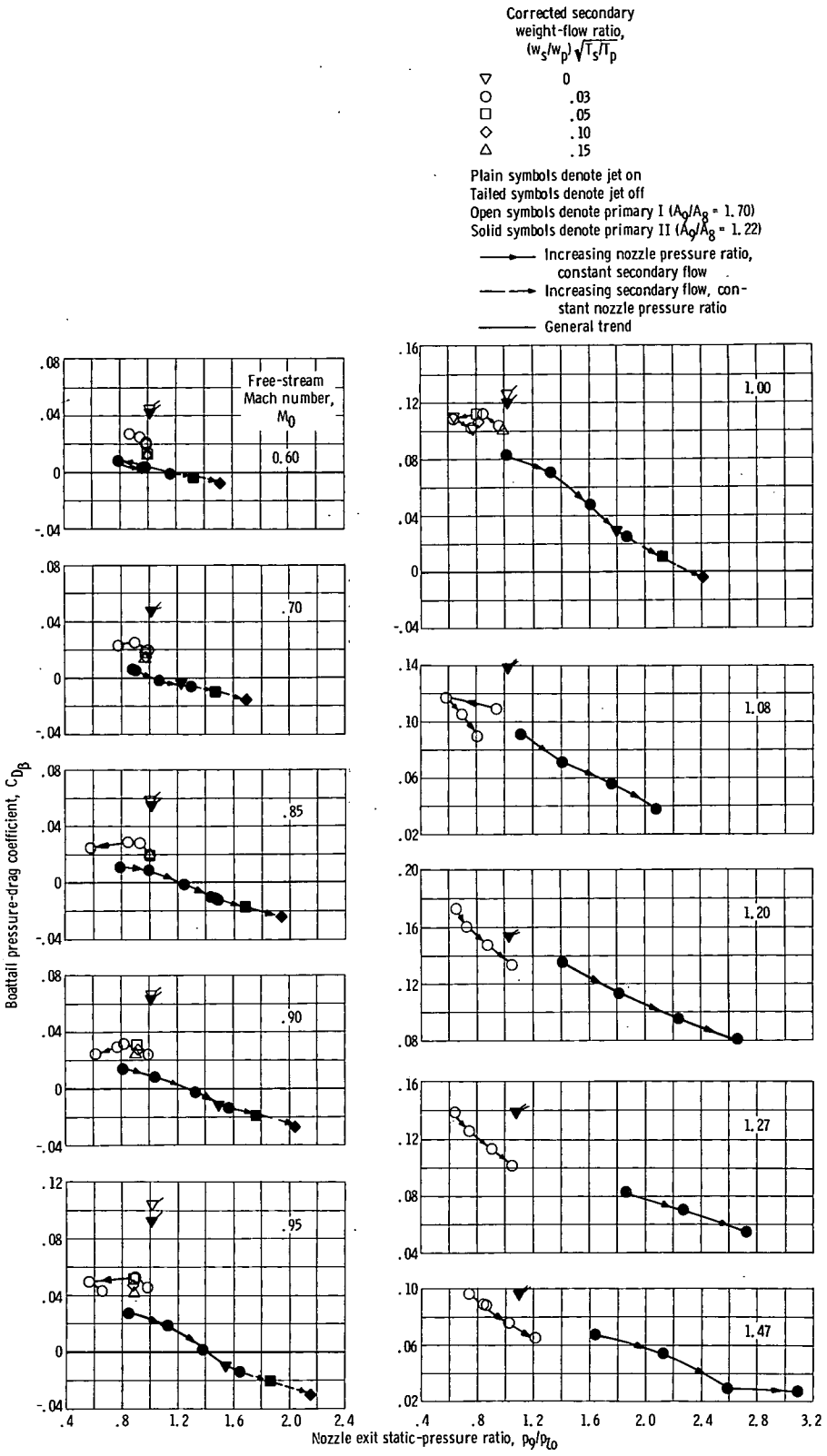

(c) Boattail angle, 15°; radius ratio, 2.5.

Figure 9. - Continued.

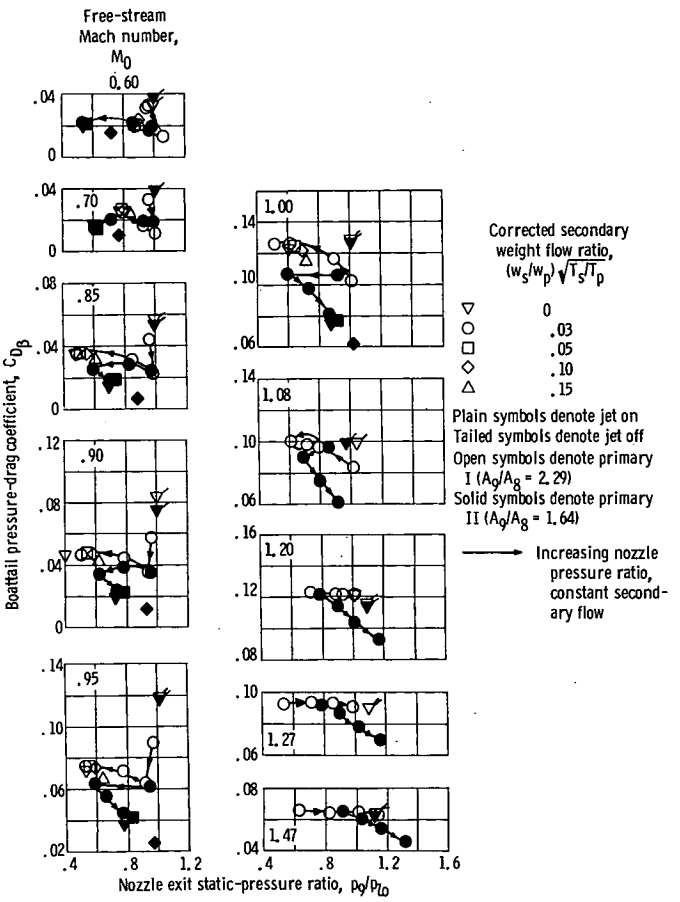

(d) Boattail angle, 10°; radius ratio, 0.5.

Figure 9. - Concluded.

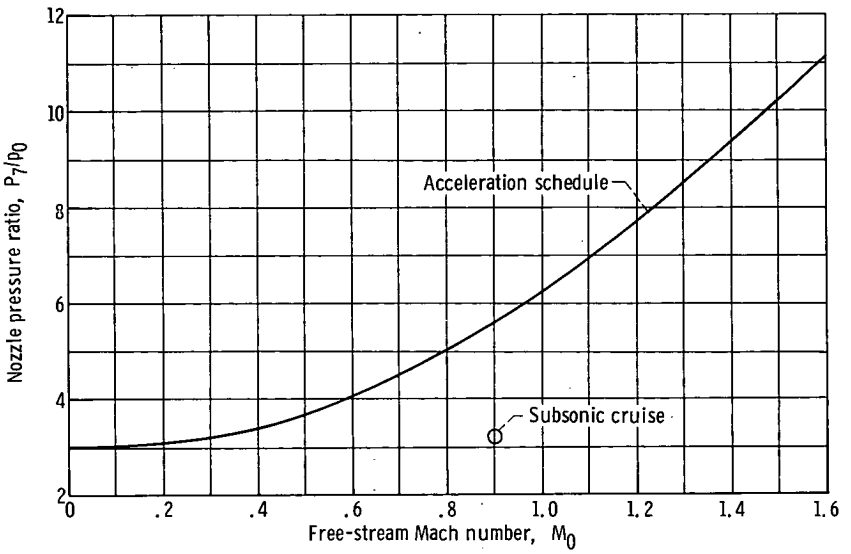

Figure 10. - Assumed turbojet pressure ratio schedule.

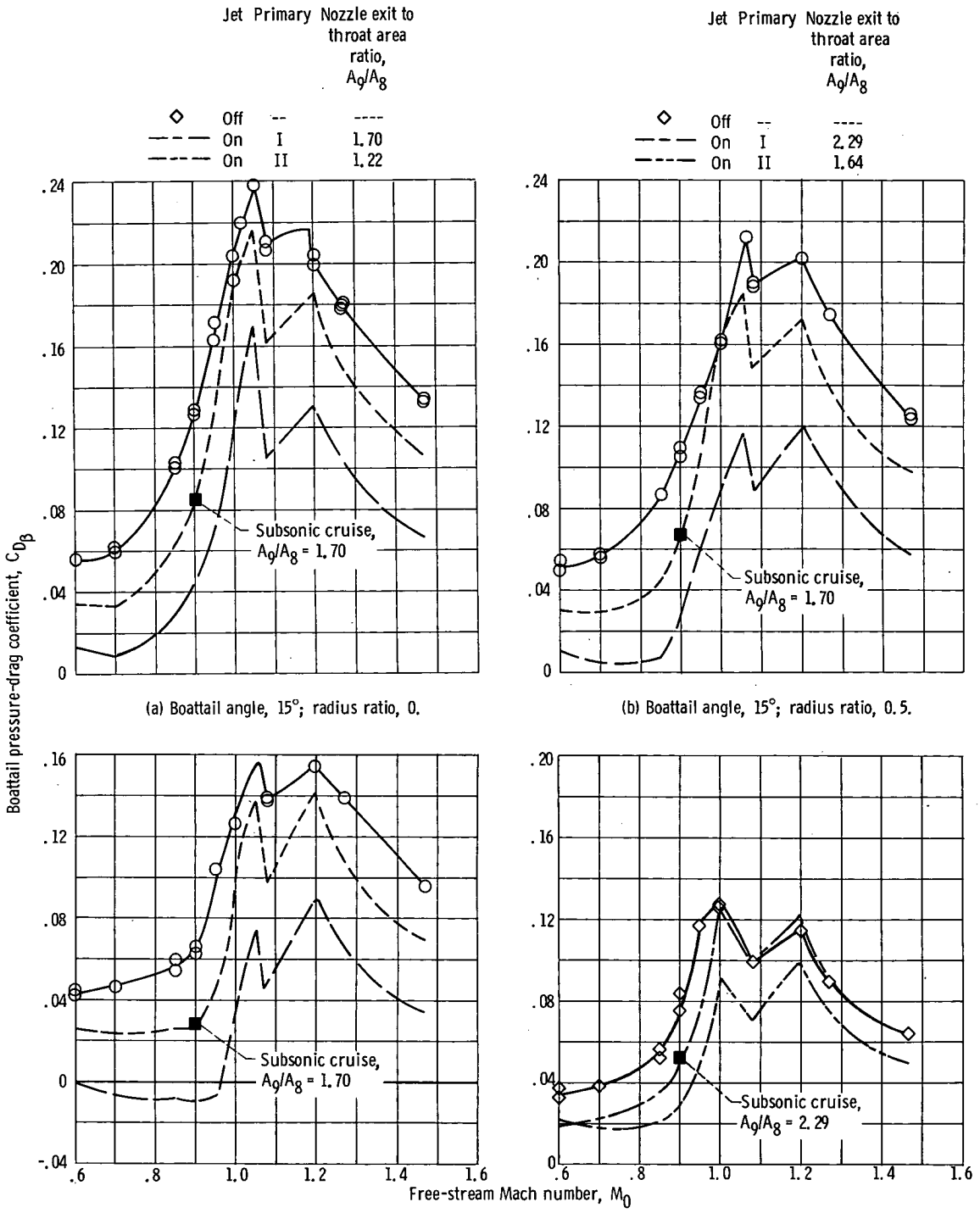

Figure 11. - Effect of nozzle jet flow on boattail pressure-drag coefficient for assumed turbojet pressure ratio schedule. Corrected secondary weight flow ratio, 0.03 (for jet on only).

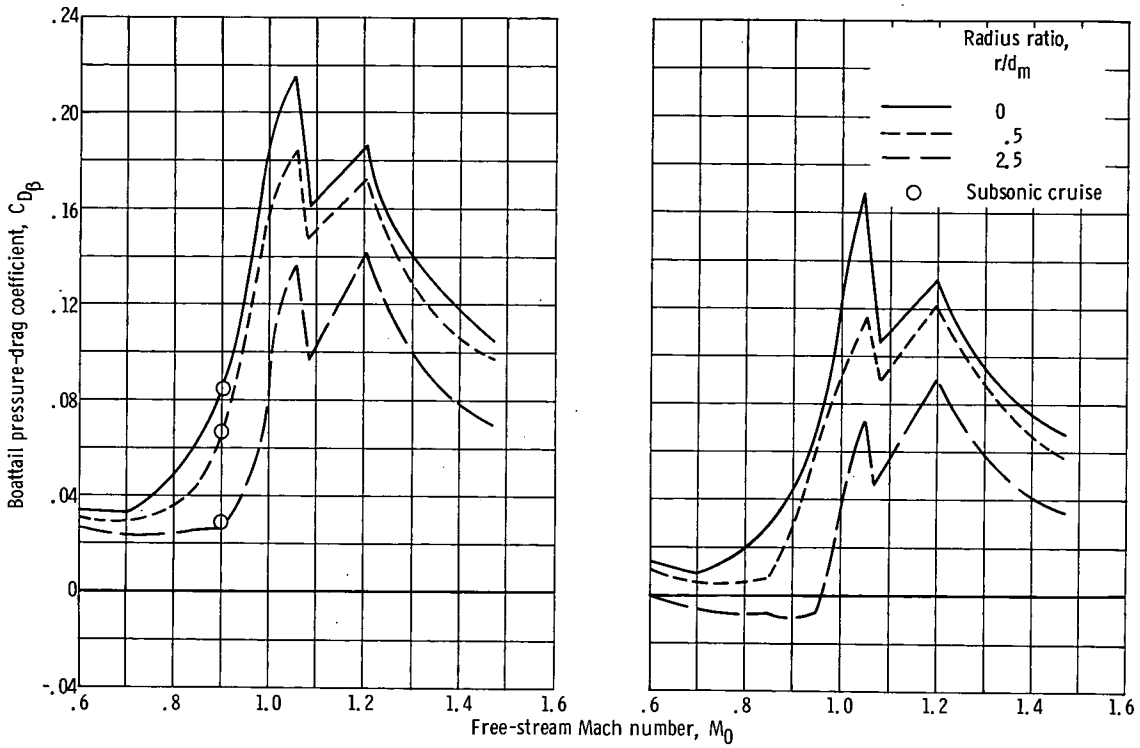

(a) Primary I; nozzle exit to throat area ratio, 1.70.

(b) Primary II; nozzle exit to throat area ratio, 1.22.

Figure 12. - Comparison of boattail pressure-drag coefficients for different radius ratios using assumed turbojet pressure ratio schedule. Boattail angle, 15° corrected secondary weight flow ratio, 0.03.

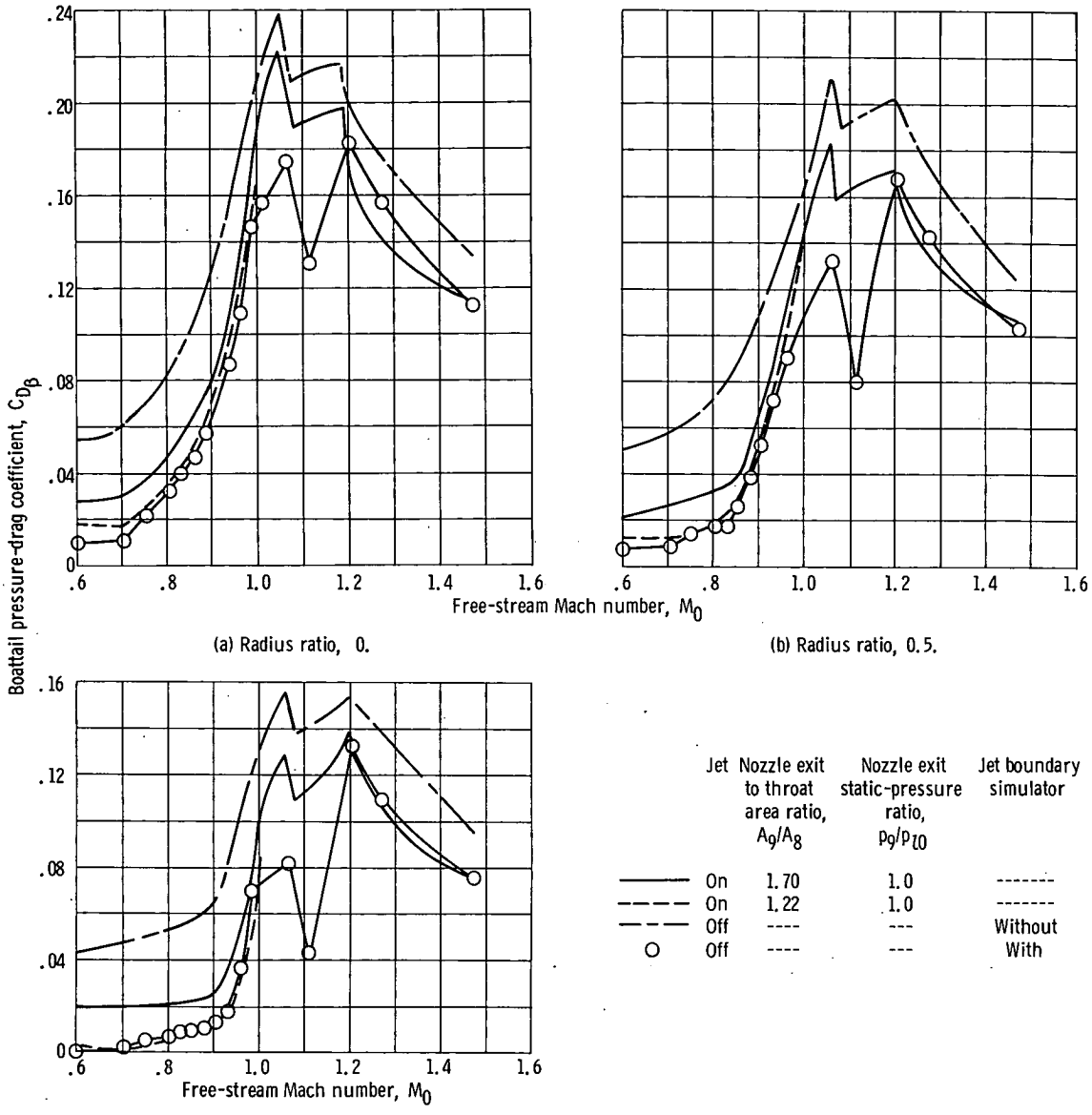

Figure 13. - Comparison of jet boundary simulator data with jet on and jet off data. Boattail angle, 15°; corrected secondary weight flow ratio, 0.03 (jet on only).

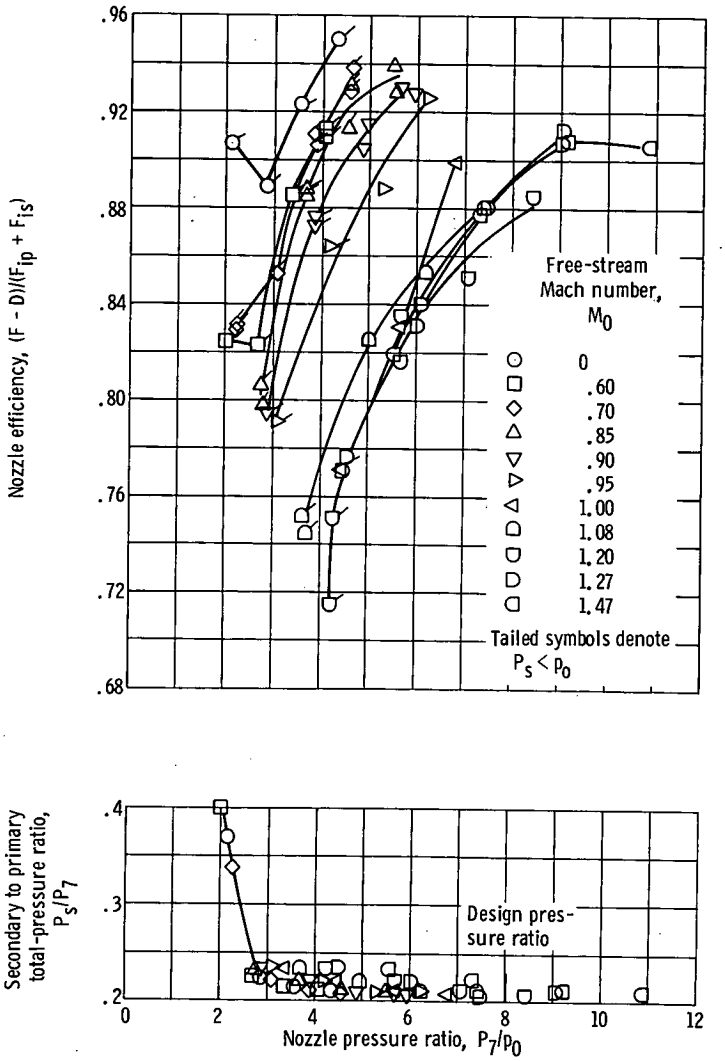

(a) Boattail angle, 15°; radius ratio, 0; primary I; nozzle exit to throat area ratio, 1.70.

Figure 14. - Effect of nozzle pressure ratio on nozzle performance characteristics. Corrected secondary weight flow ratio, 0.03.

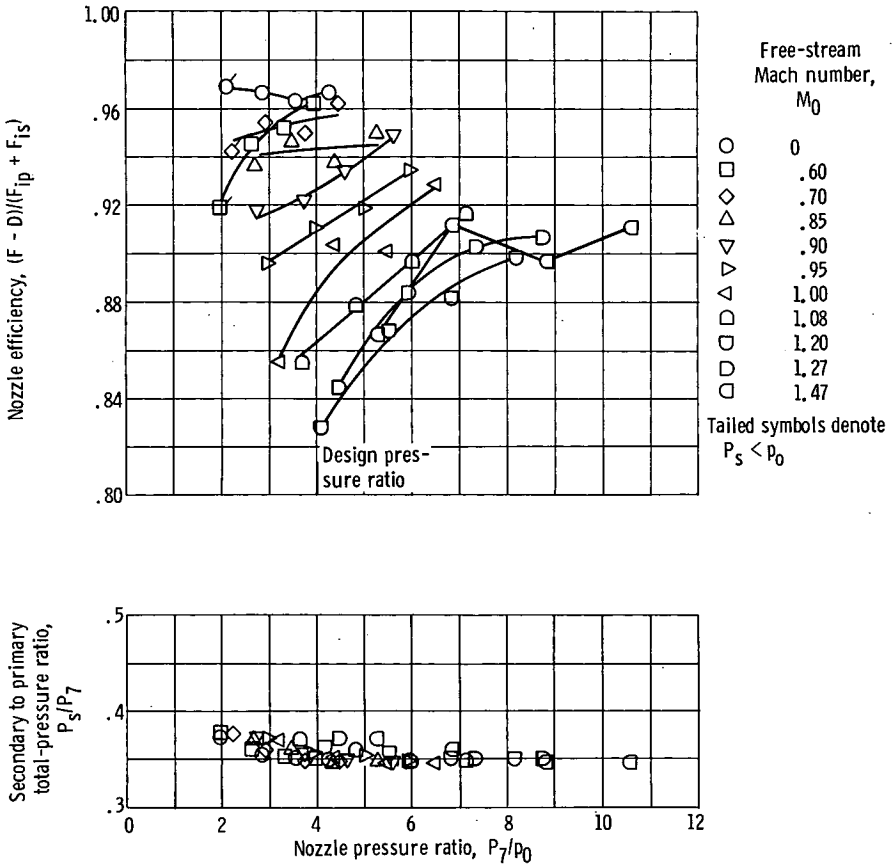

(b) Boattail angle, 15°; radius ratio, 0; primary II; nozzle exit to throat area ratio, 1.22.

Figure 14. - Continued.

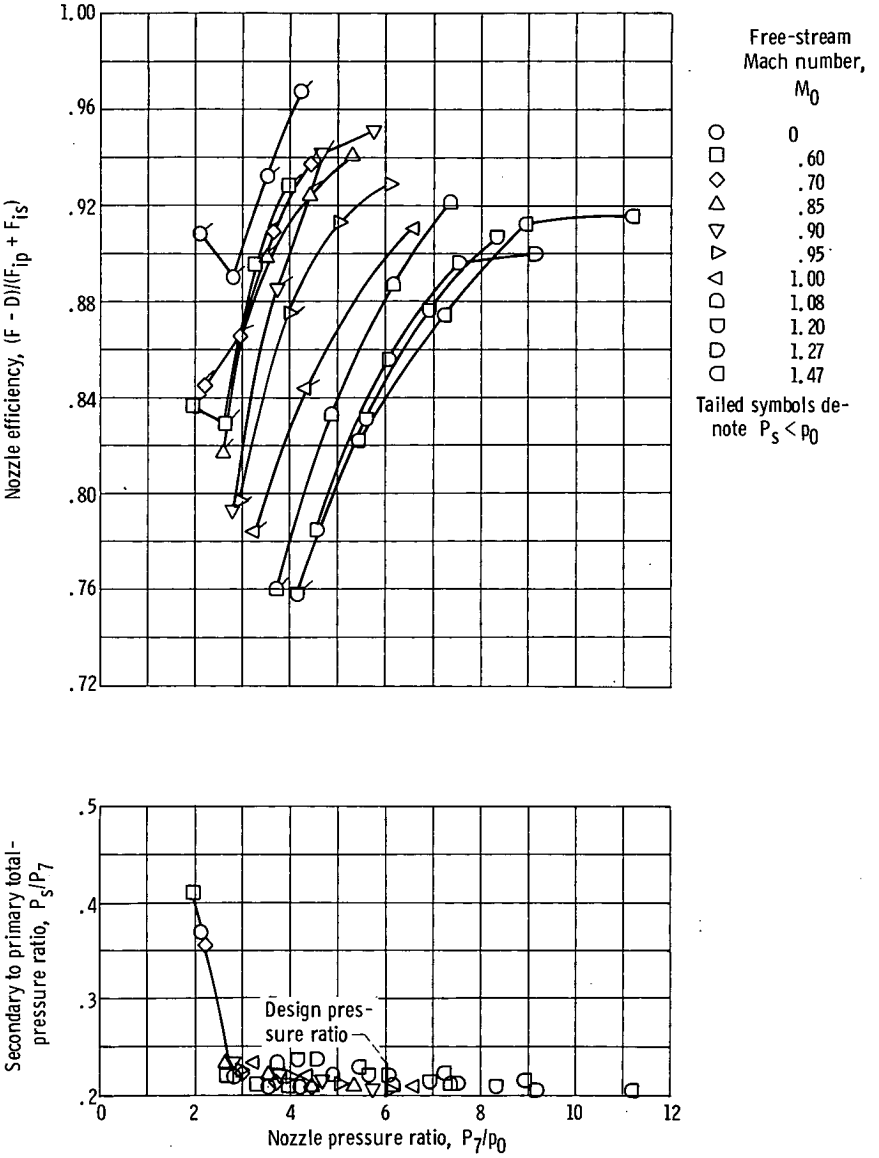

(c) Boattail angle, 15°; radius ratio, 0.5; primary I; nozzle exit to throat area ratio, 1.70.

Figure 14. - Continued.

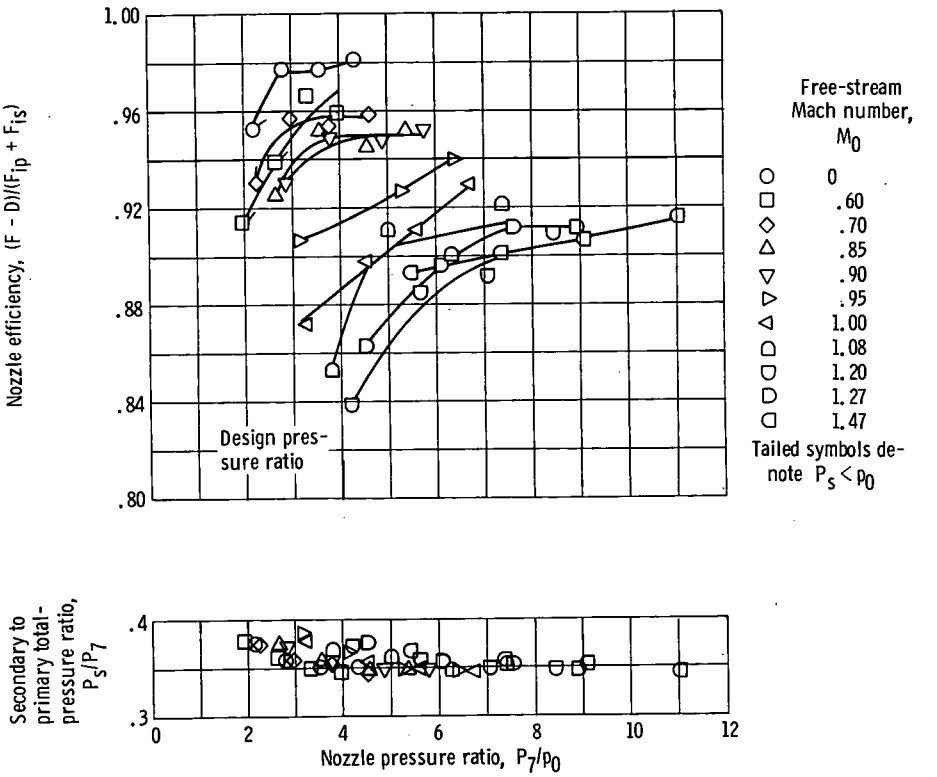

(d) Boattail angle, 15°; radius ratio, 0.5; primary II; nozzle exit to throat area ratio, 1.22.

Figure 14. - Continued.

E-4816

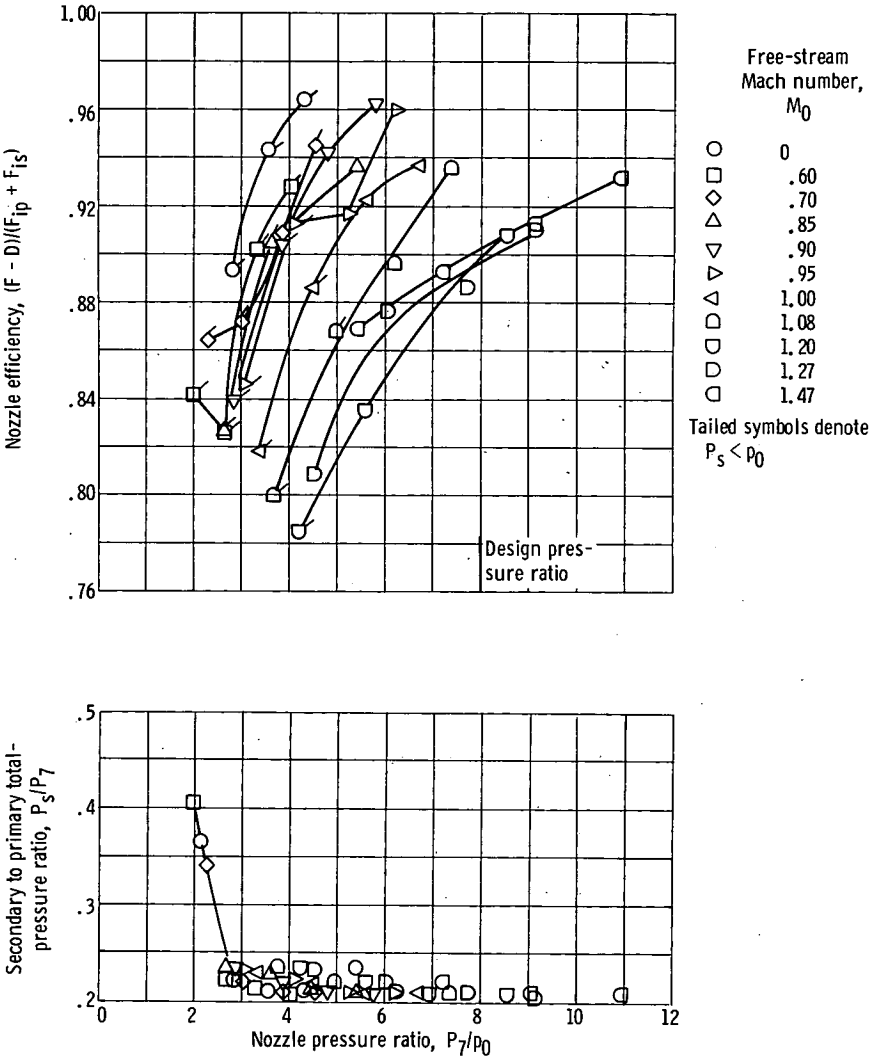

(e) Boattail angle, 15°; radius ratio, 2.5; primary I; nozzle exit to throat area ratio, 1.70.

Figure 14. - Continued.

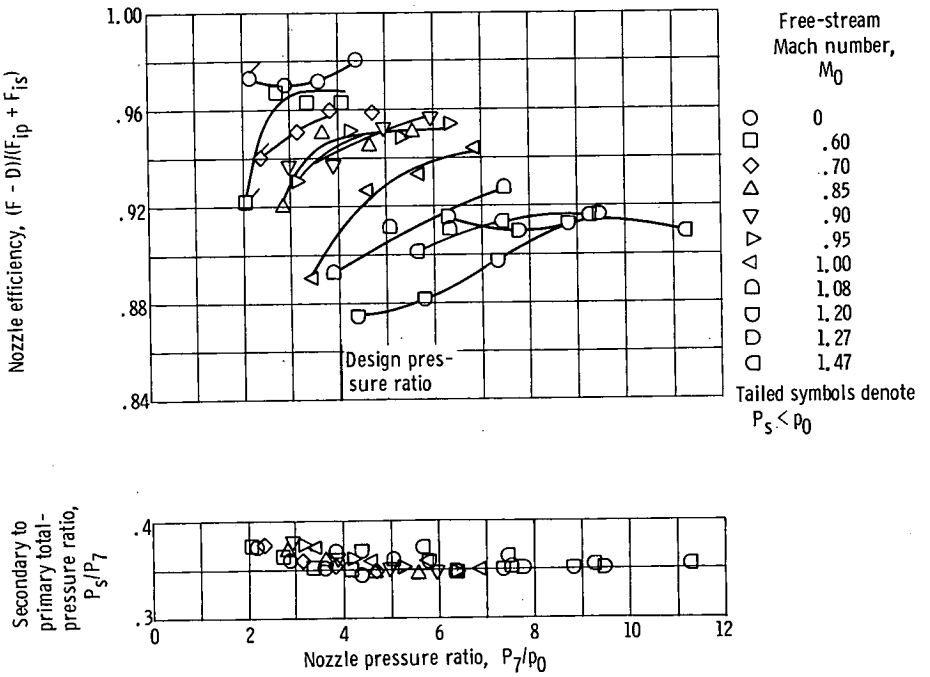

(f) Boattail angle, 15°; radius ratio, 2.5; primary II; nozzle exit to throat area ratio, 1.22.

Figure 14. - Continued.

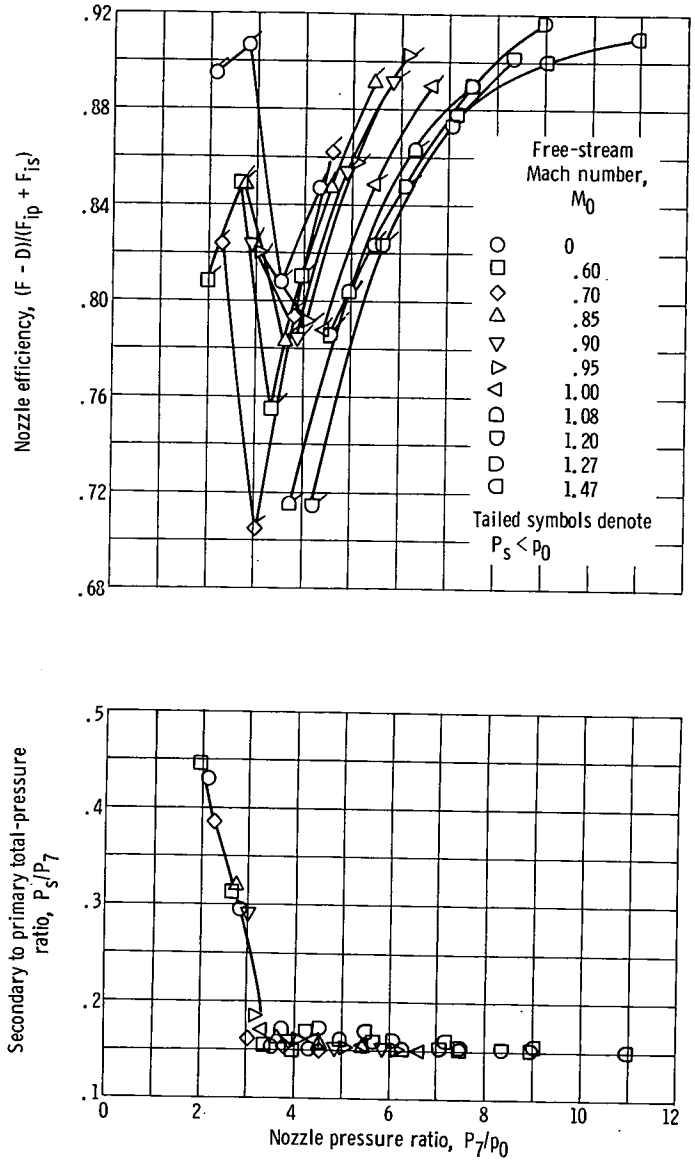

(g) Boattail angle, 10°; radius ratio, 0.5; primary I; nozzle exit to throat area ratio, 2.29; design pressure ratio, 13.5.

Figure 14. - Continued.

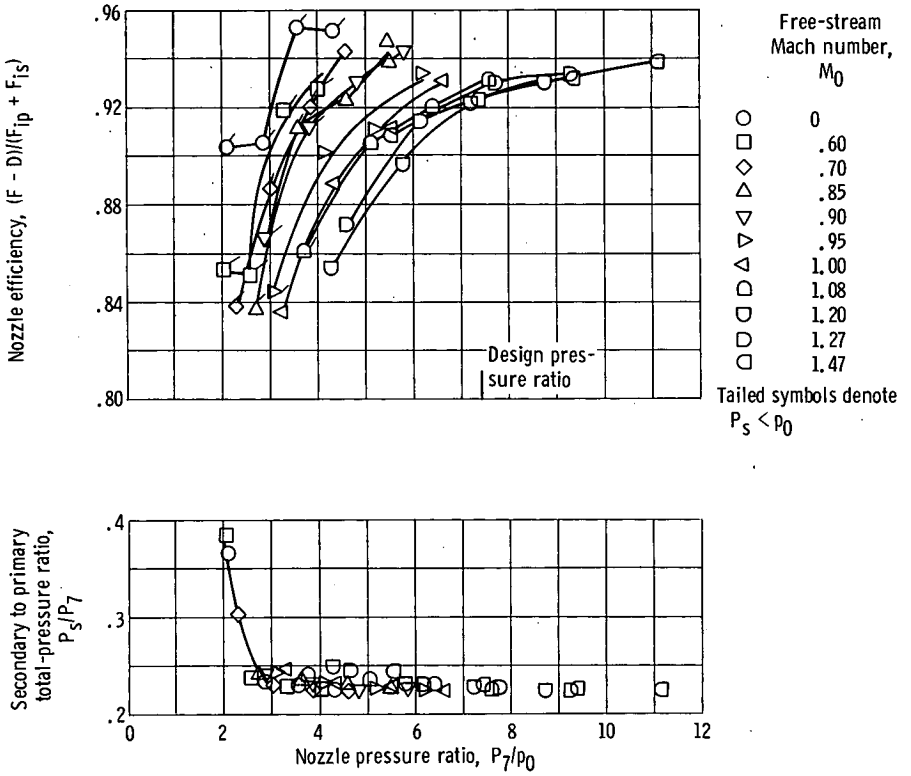

(h) Boattail angle, 10°; radius ratio, 0.5; primary II; nozzle exit to throat area ratio, 1.64.

Figure 14. - Concluded.

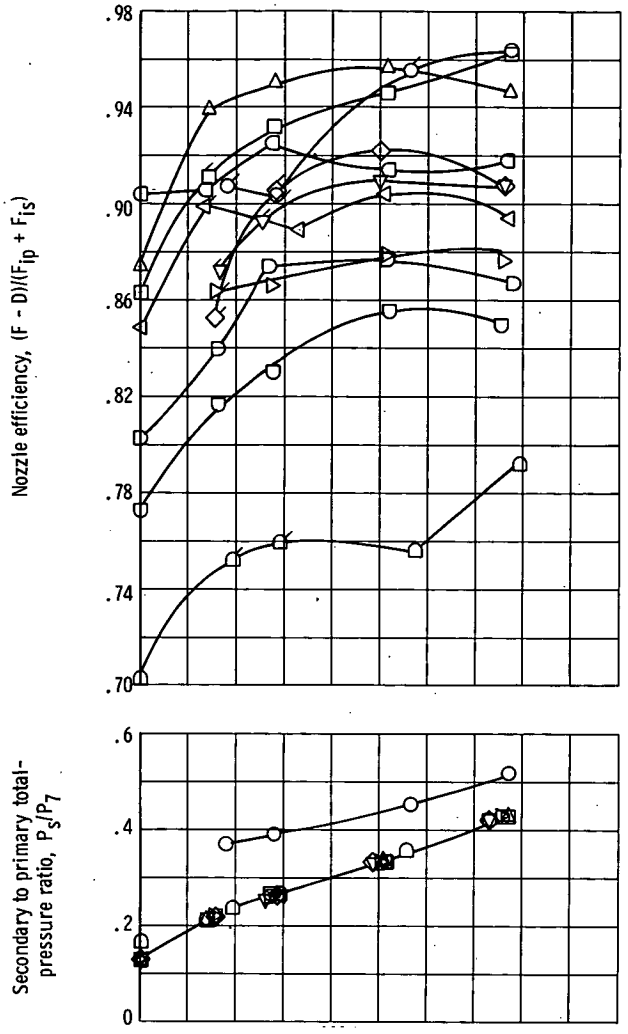

(a) Boattail angle, 15°; radius ratio, 0; primary I; nozzle exit to throat area ratio, 1.70; design pressure ratio, 7.96.

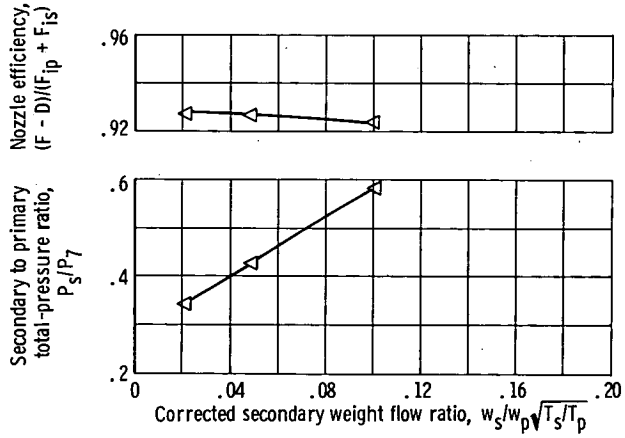

(b) Boattail angle, 15°; radius ratio, 0; primary II; nozzle exit to throat area ratio, 1.22; design pressure ratio, 4.01.

Figure 15. - Effect of corrected secondary weight flow ratio on nozzle performance characteristics.

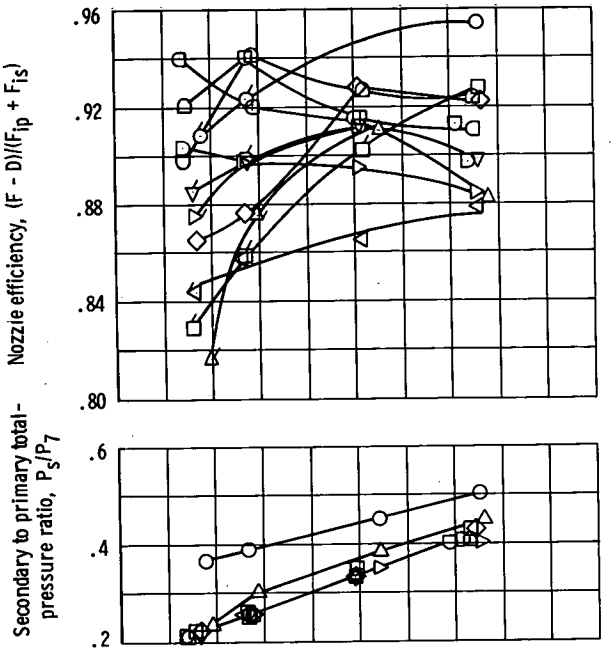

(c) Boattail angle, 15°; radius ratio, 0.5; primary I; nozzle exit to throat area ratio, 1.70; design pressure ratio, 7.96.

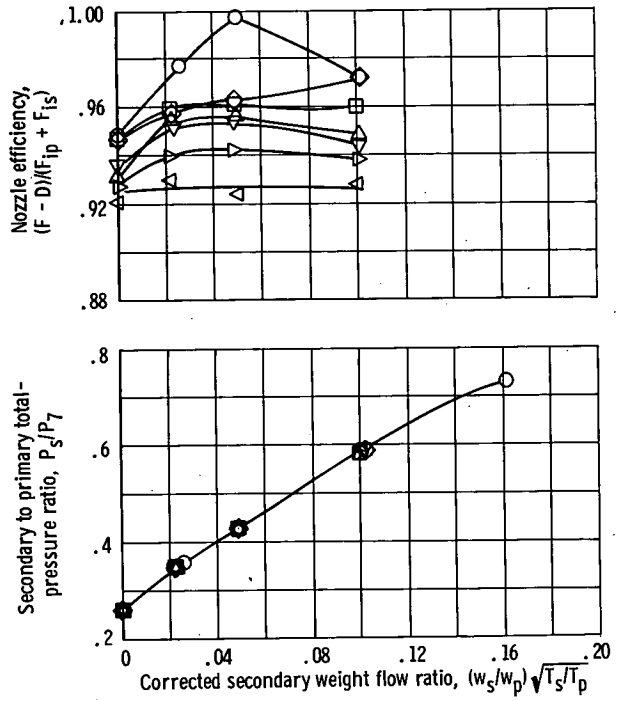

(d) Boattail angle, 15°; radius ratio, 0.5; primary II; nozzle exit to throat area ratio, 1.22; design pressure ratio, 4.01.

Figure 15. - Continued.

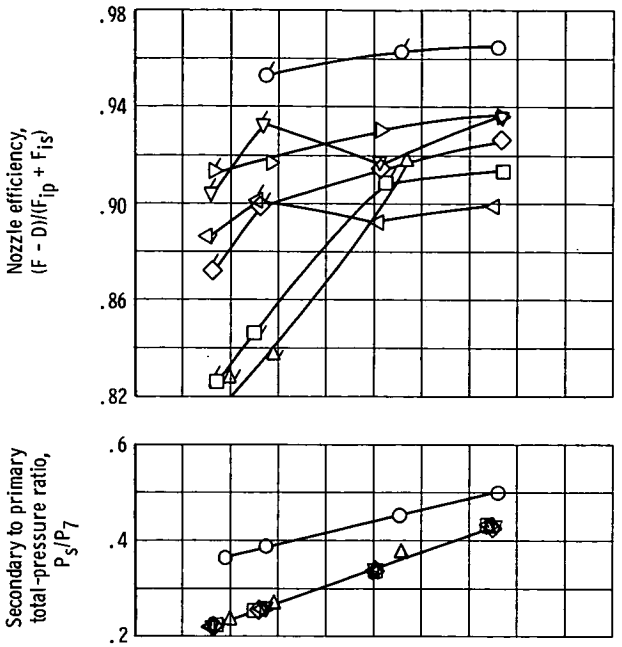

(e) Boattail angle, 15°; radius ratio, 2.5; primary I; nozzle exit to throat area ratio, 1.70; design pressure ratio, 7.96.

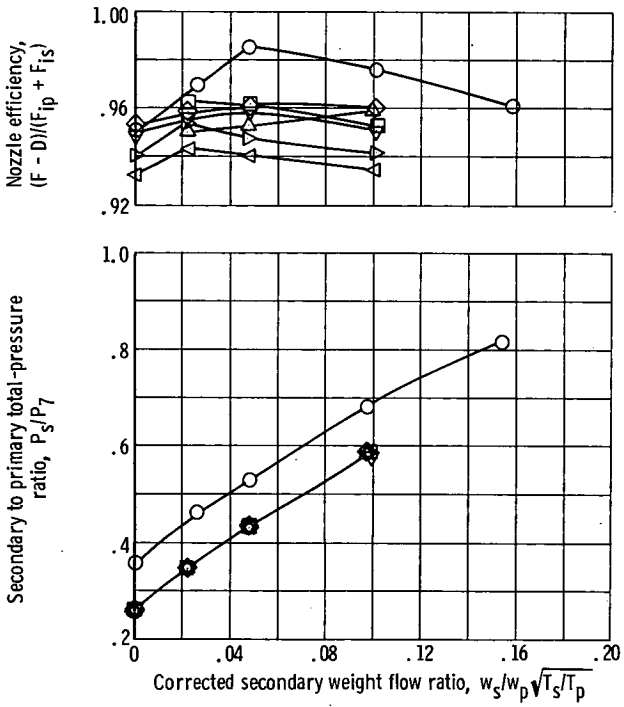

(f) Boattail angle, 15°; radius ratio, 2.5; primary II; nozzle exit to throat area ratio, 1.22; design pressure ratio, 4.01.

Figure 15. - Continued.

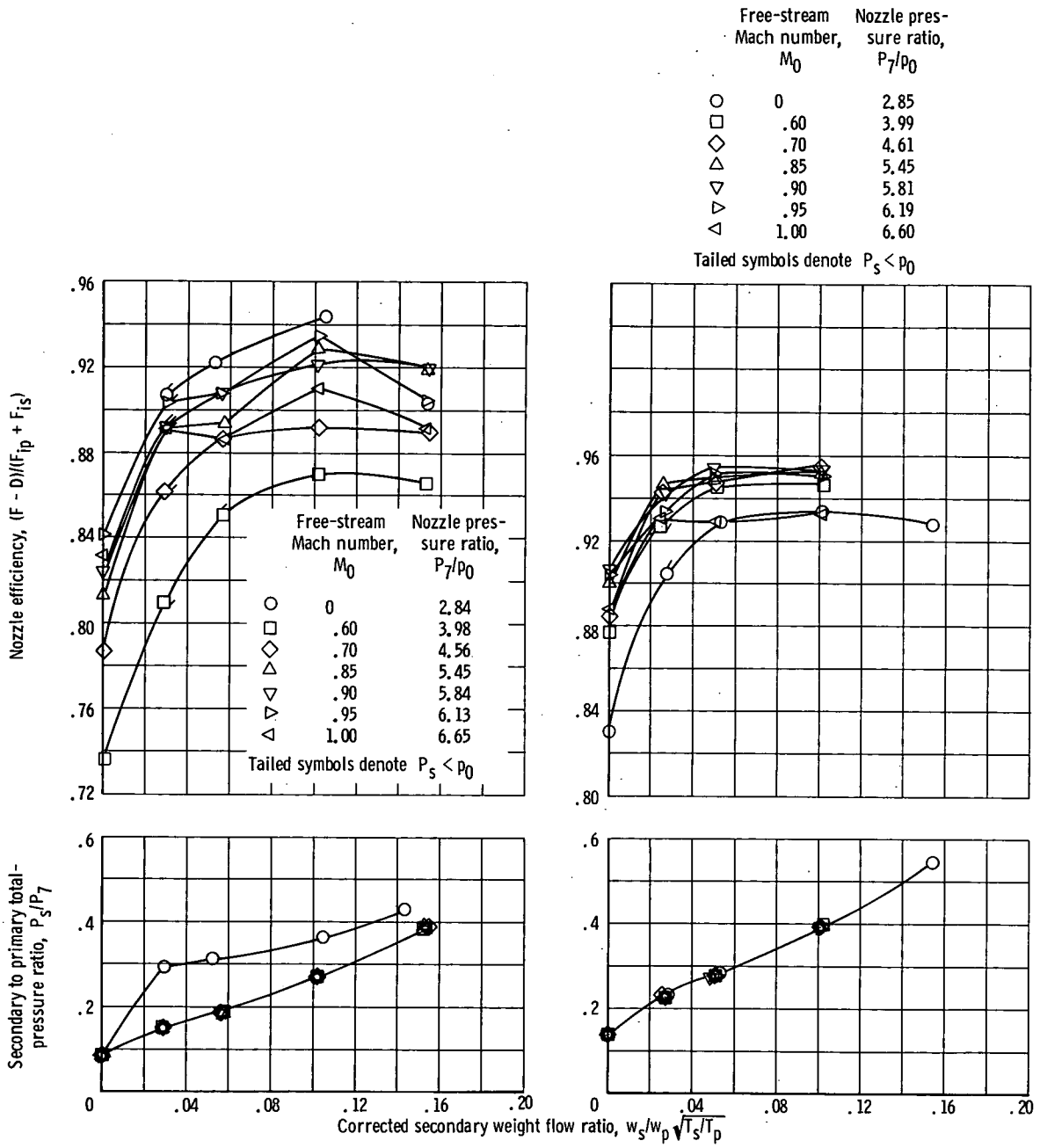

(g) Boattail angle, 10°; radius ratio, 0.5; primary I; nozzle exit to throat area ratio, 2.29; design pressure ratio, 13.50.

(h) Boattail angle, 10°; radius ratio, 0.5; primary II; nozzle exit to throat area ratio, 1.64; design pressure ratio, 7.44.

Figure 15. - Concluded.

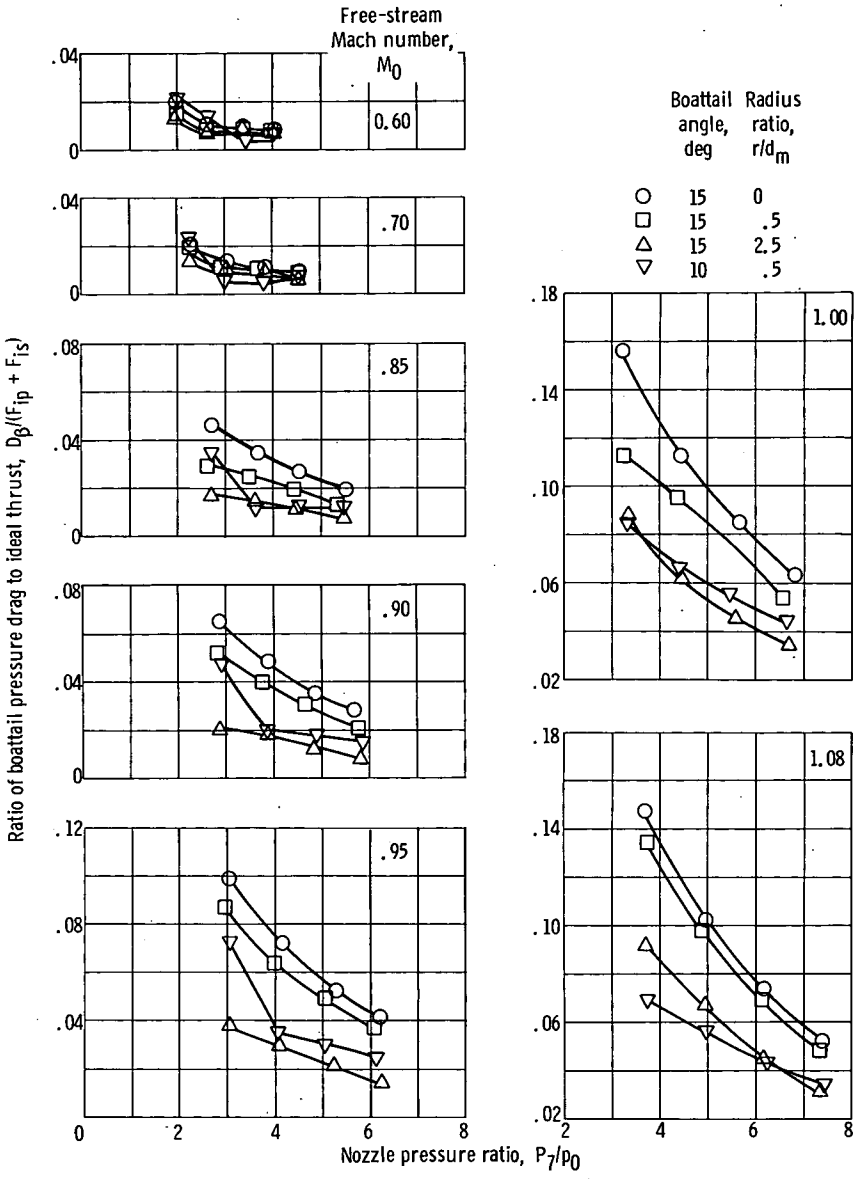

(a) Primary I.

Figure 16. - Comparison of boattail pressure drag to ideal thrust.

E-4077

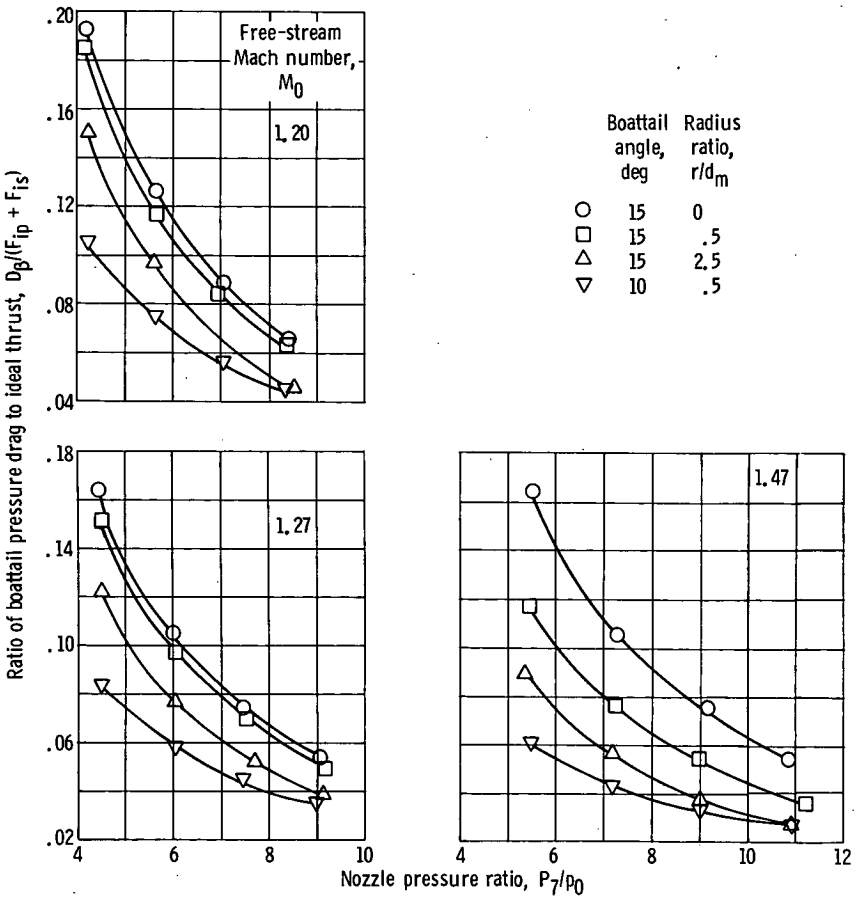

(a) Concluded.

Figure 16. - Continued.

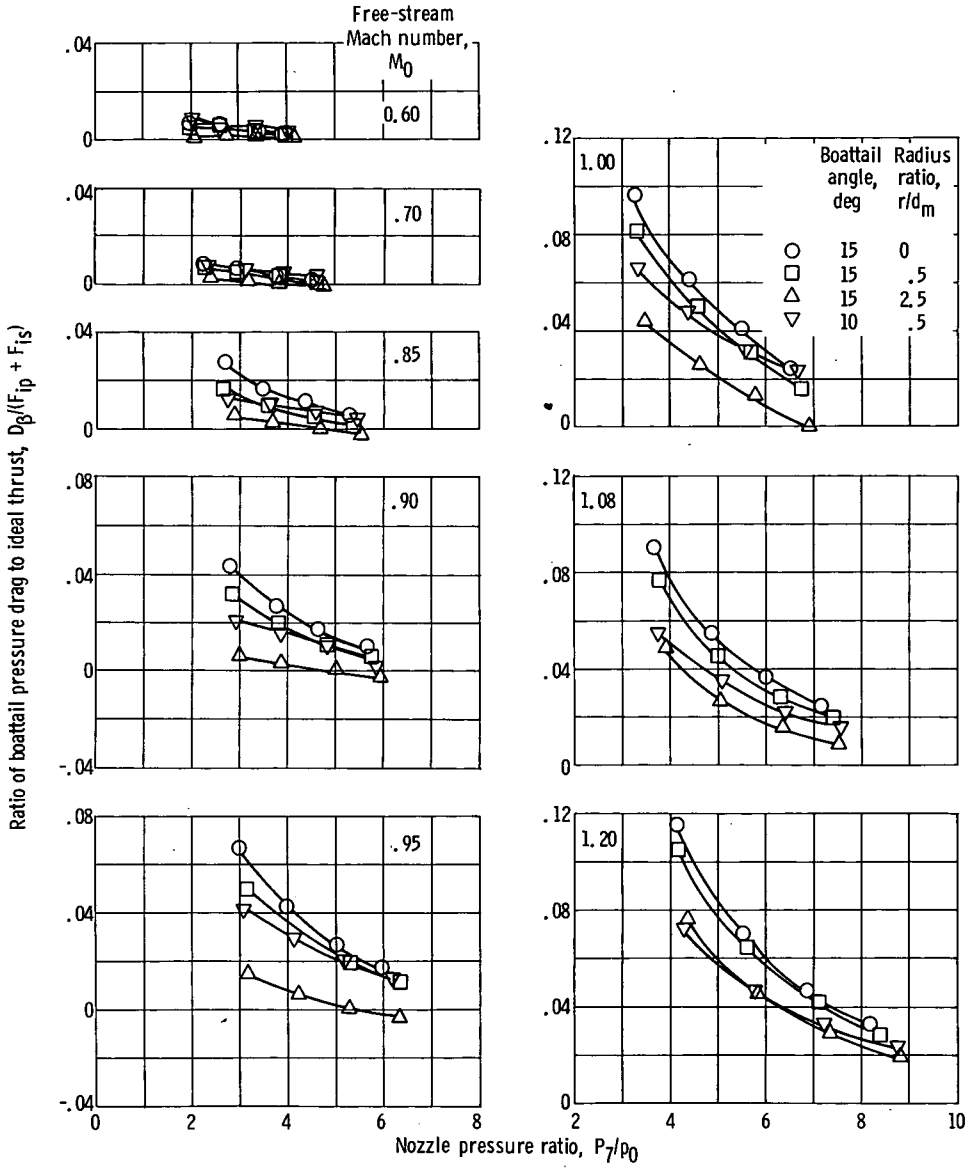

(b) Primary II.

Figure 16. - Continued.

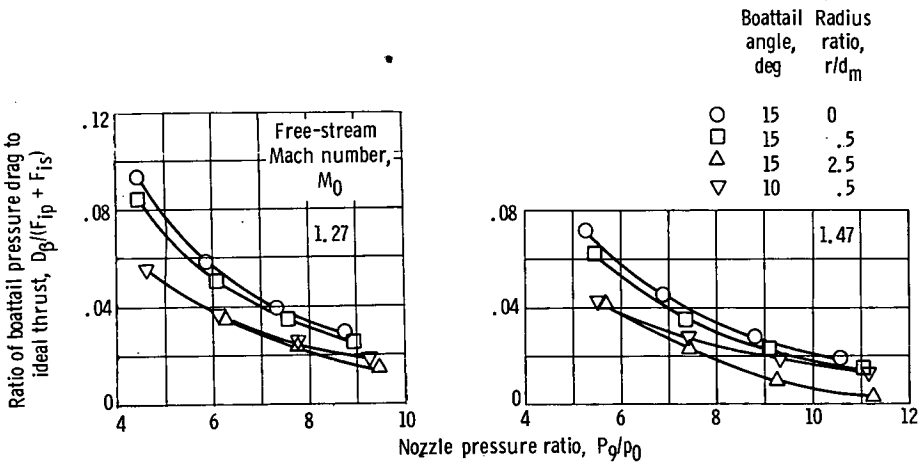

(b) Concluded.

Figure 16. - Concluded.

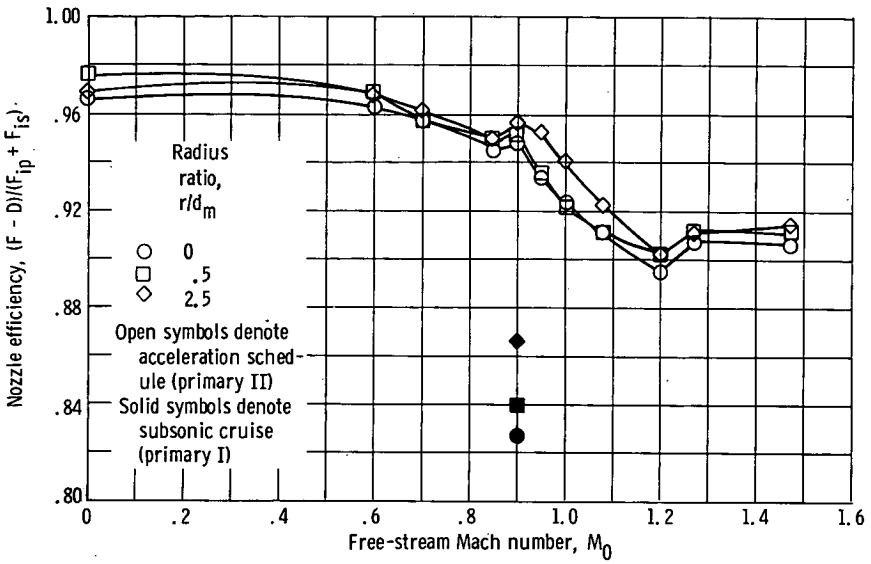

Figure 17. - Effect of radius ratio on nozzle efficiency using assumed pressure ratio schedule. Boattail angle, 15°; corrected secondary weight flow ratio, 0.03.

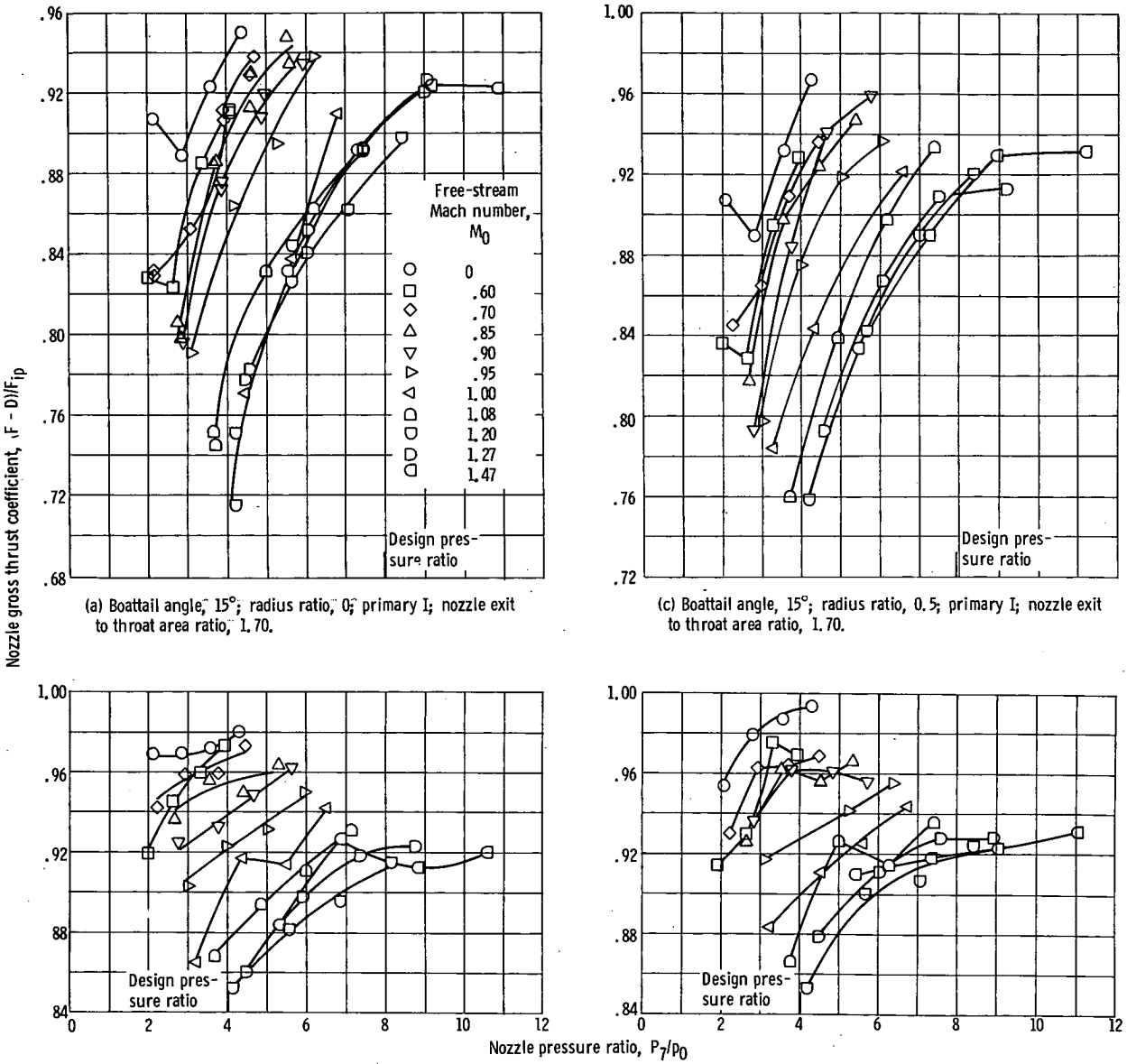

(a) Boattail angle, 15°; radius ratio, 0; primary I; nozzle exit to throat area ratio, 1.70.

(c) Boattail angle, 15°; radius ratio, 0.5; primary I; nozzle exit to throat area ratio, 1.70.

(b) Boattail angle, 15°; radius ratio, 0; primary II; nozzle exit to throat area ratio, 1.22.

(d) Boattail angle, 15°; radius ratio, 0.5; primary II; nozzle exit to throat area ratio, 1.22.

Figure 18. - Effect of nozzle pressure ratio on nozzle gross thrust coefficient. Corrected secondary weight flow ratio, 0.03

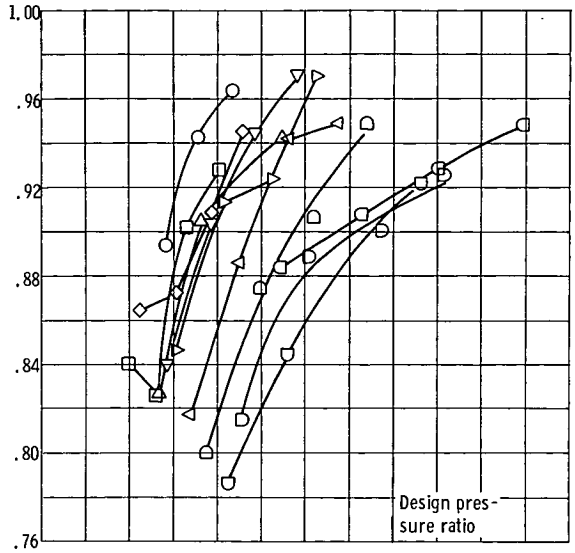

(e) Boattail angle, 15°; radius ratio, 2.5; primary I; nozzle exit to throat area ratio, 1.70.

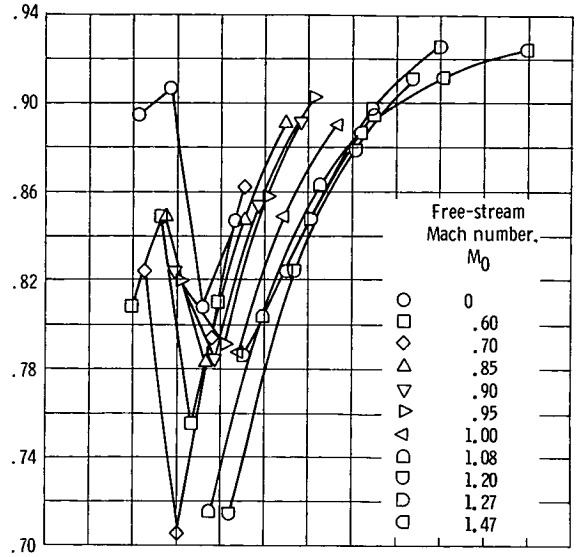

(g) Boattail angle, 10°; radius ratio, 0.5; primary I; nozzle exit to throat area ratio, 2.29; design pressure ratio, 13.5.

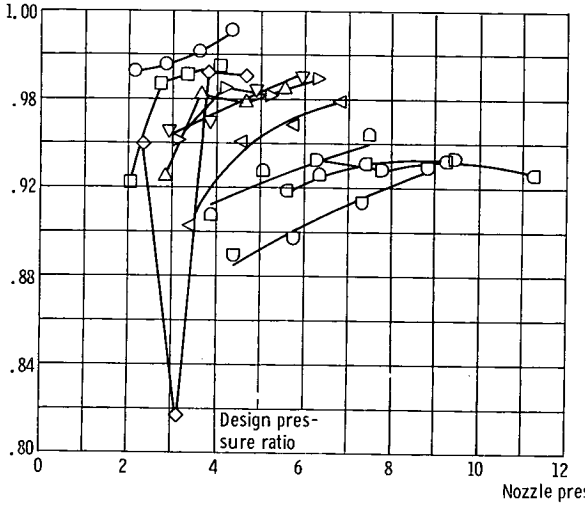

(f) Boattail angle, 15°; radius ratio, 2.5; primary II; nozzle exit to throat area ratio, 1.22.

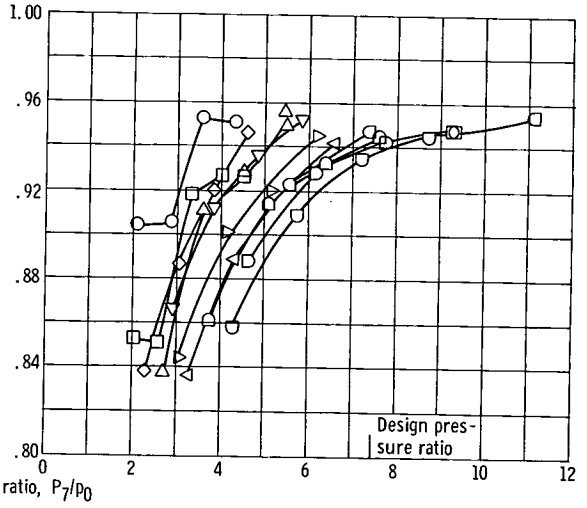

(h) Boattail angle, 10°; radius ratio, 0.5; primary II; nozzle exit to throat area ratio, 1.64.

Nozzle gross thrust coefficient, $(F - D)/F_{ip}$

Nozzle pressure ratio, P_7/p_0

Figure 18. - Concluded.

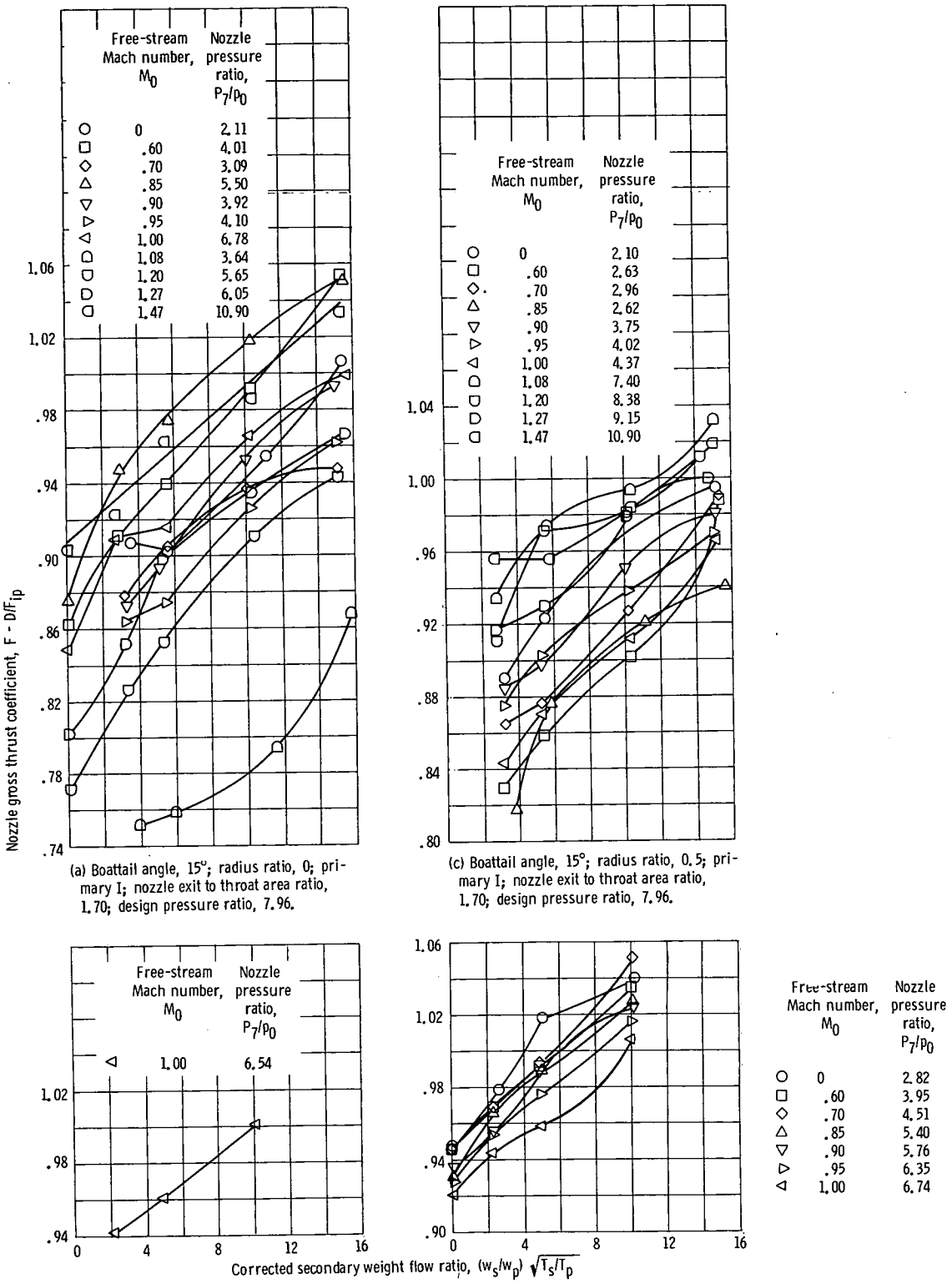

(a) Boattail angle, 15°; radius ratio, 0; primary I; nozzle exit to throat area ratio, 1.70; design pressure ratio, 7.96.

(c) Boattail angle, 15°; radius ratio, 0.5; primary I; nozzle exit to throat area ratio, 1.70; design pressure ratio, 7.96.

(b) Boattail angle, 15°; radius ratio, 0; primary II; nozzle exit to throat area ratio, 1.22; design pressure ratio, 4.01.

(d) Boattail angle, 15°; radius ratio, 0.5; primary II; nozzle exit to throat area ratio, 1.22; design pressure ratio, 4.01.

Figure 19. - Effect of corrected secondary weight flow ratio on nozzle gross thrust coefficient.

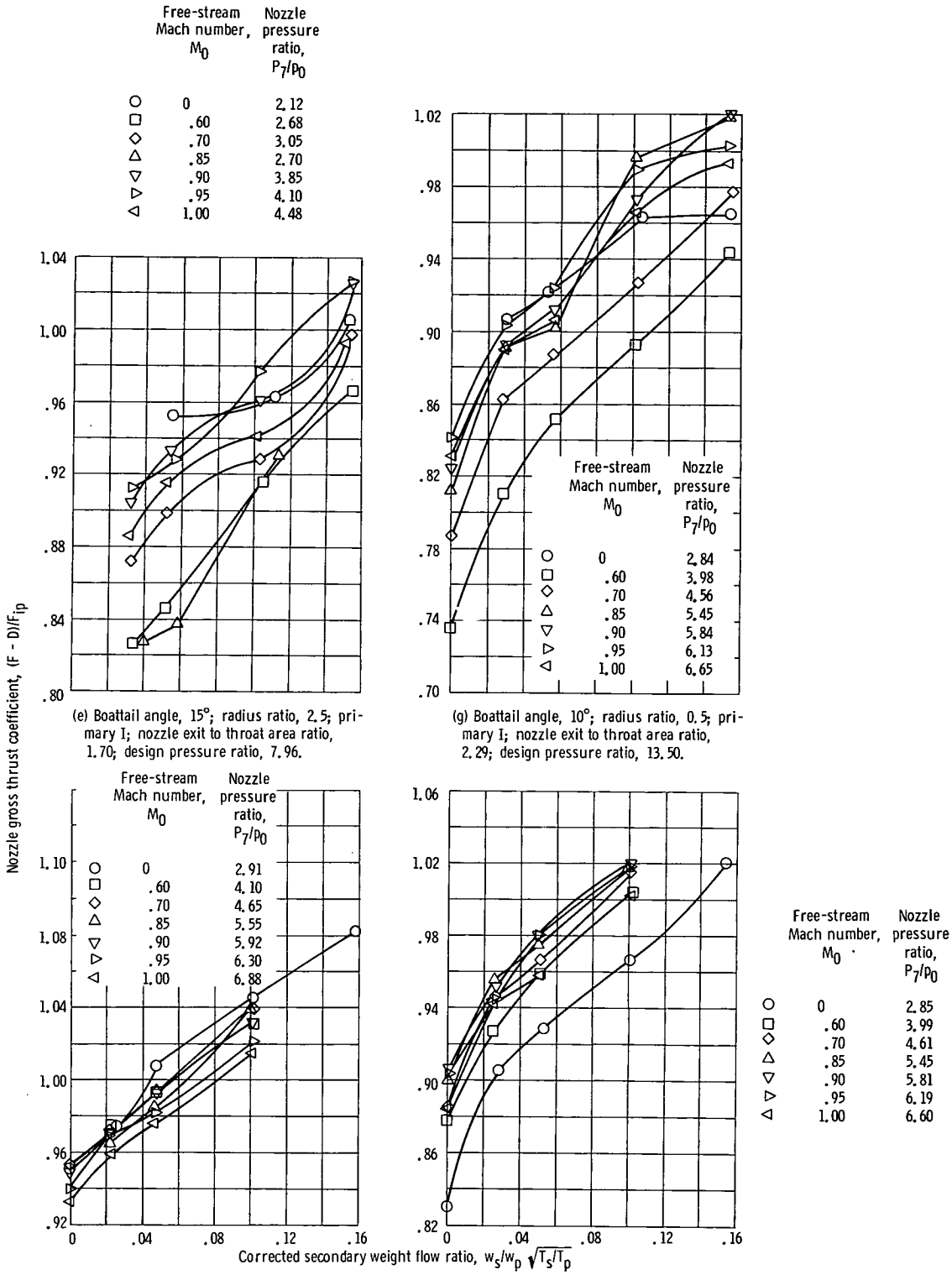

(e) Boattail angle, 15°; radius ratio, 2.5; primary I; nozzle exit to throat area ratio, 1.70; design pressure ratio, 7.96.

(g) Boattail angle, 10°; radius ratio, 0.5; primary I; nozzle exit to throat area ratio, 2.29; design pressure ratio, 13.50.

(f) Boattail angle, 15°; radius ratio, 2.5; primary II; nozzle exit to throat area ratio, 1.22; design pressure ratio, 4.01.

(h) Boattail angle, 10°; radius ratio, 0.5; primary II; nozzle exit to throat area ratio, 1.64; design pressure ratio, 7.44.

Figure 19. - Concluded.

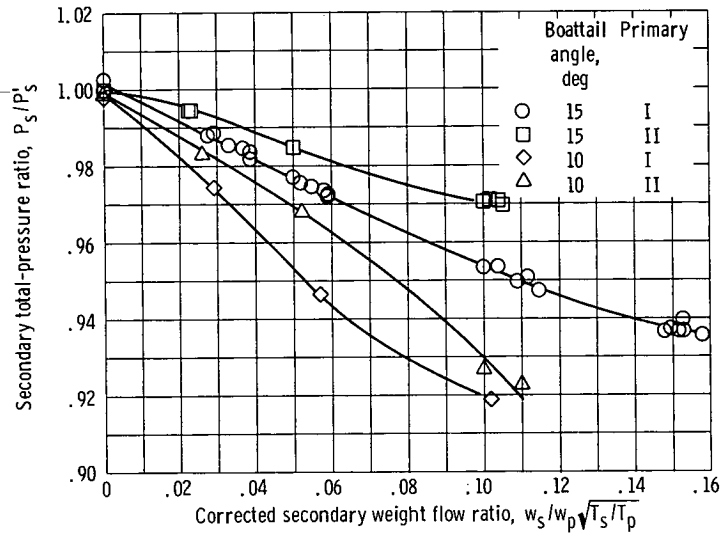

Figure 20. - Total-pressure loss through secondary-flow passage.

NASA-Langley, 1969 —— 28 E-4816

"The aeronautical and space activities of the United States shall be conducted so as to contribute . . . to the expansion of human knowledge of phenomena in the atmosphere and space. The Administration shall provide for the widest practicable and appropriate dissemination of information concerning its activities and the results thereof."

—NATIONAL AERONAUTICS AND SPACE ACT OF 1958

NASA SCIENTIFIC AND TECHNICAL PUBLICATIONS

TECHNICAL REPORTS: Scientific and technical information considered important, complete, and a lasting contribution to existing knowledge.

TECHNICAL NOTES: Information less broad in scope but nevertheless of importance as a contribution to existing knowledge.

TECHNICAL MEMORANDUMS: Information receiving limited distribution because of preliminary data, security classification, or other reasons.

CONTRACTOR REPORTS: Scientific and technical information generated under a NASA contract or grant and considered an important contribution to existing knowledge.

TECHNICAL TRANSLATIONS: Information published in a foreign language considered to merit NASA distribution in English.

SPECIAL PUBLICATIONS: Information derived from or of value to NASA activities. Publications include conference proceedings, monographs, data compilations, handbooks, sourcebooks, and special bibliographies.

TECHNOLOGY UTILIZATION PUBLICATIONS: Information on technology used by NASA that may be of particular interest in commercial and other non-aerospace applications. Publications include Tech Briefs, Technology Utilization Reports and Notes, and Technology Surveys.

Details on the availability of these publications may be obtained from:

SCIENTIFIC AND TECHNICAL INFORMATION DIVISION

NATIONAL AERONAUTICS AND SPACE ADMINISTRATION

Washington, D.C. 20546